UNIVERSITY OF SOUTHAMPTON
FACULTY OF ENGINEERING, SCIENCE AND MATHEMATICS
School of Electronics and Computer Science

Design and Fabrication of a New 3D AC-Electroosmotic Micropump

by

Hamza A ROUABAH

A thesis submitted for the degree of
Doctor of Philosophy

March 2010

UNIVERSITY OF SOUTHAMPTON

ABSTRACT

FACULTY OF ENGINEERING, SCIENCE AND MATHEMATICS
SCHOOL OF ELECTRONICS AND COMPUTER SCIENCE

Doctor of Philosophy

DESIGN AND FABRICATION OF A NEW FLUIDIC MICROPUMP

by Hamza A ROUABAH

Integrated Microsystems, MicroTAS or the Lab-on-a-chip, require integrated fluid handling. Advances in microelectronics fabrication processes have allowed the miniaturization of fluid handling devices such as micropumps. In biomedical technology, pumps for handling extremely small fluid amounts become more and more important where microsystems for biological analysis routinely use solid-state electrokinetic micropumps.

AC Electrokinetic micropumps in particular AC electroosmosis pump can be used to pump fluids using planar electrodes which induce electrical forces on the fluid. However, planar electrodes have limited pumping capability of the micropump.

In this theses a new design for the AC electroosmotic is introduced. The new AC electroosmotic design presents the transition from planar microelectrode arrays to planar with High Aspect Ratio (HAR) pillars in order to increase the surface area of the electrodes. The physical mechanism of AC electrosmosis is the motion of induced Electrical Double Layers on microelectrodes driven into motion by the electric field generated by the electrodes. Since AC electrosmosis is a surface driven effect, increasing the surface area increases the power coupled into the fluid movement. By taking the channel volume and filling it with conductive pillars, the surface area therefore increases, but the volume remains the same, increasing the drive per unit volume. This will have the effect of increasing the pressure generated by the pump.

To explore and realize the proposed pumping principle we attempted to benefit from available expertise of Professor Marc. J. Madou who specializes in Bio-MEMS field and

microfabrication techniques. Prof. Madou and his team at UC Irvine have been able to construct large dimensions of high-aspect-ratio carbon pillars made out of pyrolyzed SU-8 using Carbon-MEMS process. This conversion of polymer to a conductive-polymer technique was adopted and applied to our proposed smaller dimension of 3D-electrodes design. The current planar electrodes designs studied previously were made out of gold and it is desired to make the pillars out of gold also. However due to some microfabrication limitations, and since gold pillars undergo chemical reactions involving dissolution and redeposition, pyrolyzed pillars are suitable for our process. Altough pyrolyzed SU-8 pillars are less conductive than the gold, but they are perfectly polarisable, which is ideal for AC-electroosmosis. In this particular area of interest, we have investigated with the collaboration of Prof. Madou and his team the fabrication of high-aspect-ratio carbon pillars with different aspect ratios and dimensions and introduced them to to AC-electroosmosis pumping. Carbon electrodes were successfully and generate local fluid and drive fluid, where the new 3D-AC-electroosmosis micropump has shown an increase of 5 times to previous planar electrodes design.

Contents

List of Figures

List of Tables

Declaration of Authorship

I, Hamza A ROUABAH, declare that the thesis entitled Design and Fabrication of a New Fluidic Micropump and the work presented in it are my own, I confirm that:

- this work was done wholly or mainly while in candidature for a research degree at this University;
- where any part of this thesis has previously been submitted for a degree or any other qualification at this University or any other institution, this has been clearly stated;
- where I have consulted the published work of others, this is always clearly attributed;
- where I have quoted from the work of others, the source is always given. With the exception of such quotations, this thesis is entirely my own work;
- I have acknowledged all main sources of help;
- where the thesis is based on work done by myself jointly with others, I have made clear exactly what was done by others and what I have contributed myself;
- parts of this work have been published as listed in Section 1.4 of this thesis.

Signed: _____

Date : _____

To my parents...

Chapter 1

Introduction

1.1 Context

The fast evolutions of microelectronics fabrication techniques over the last decade, have lead to the appearance of new multidisciplinary devices called MEMS (Micro-Electro-Mechanical Systems). Based on these techniques, the integration of mechanical elements, sensors, actuators and electronics components in a single device became possible. Moreover, during the last 20 years, MEMS devices were involved in the field of life science to give a birth to a sub MEMS category called Bio-MEMS. The use of Bio-MEMS devices was suitable in biology and biomedical applications for few reasons, mainly: easy to fabricate, they integrate easily with electronics, small quantity of samples and reagents can be manipulated, high precision and samples control, low fabrication costs, reproducibility and simple operation.

The high potential of Bio-MEMS field, has drawn the attention of many research groups over the world, that were able to boost this field forward. Following the trend towards smaller lab on a single device, several laboratory functions such as mixing pumping, sensing, detection, and separation, were successfully integrated on a single chip of only millimeters to a few square centimeters in size. This evolution in Bio-MEMS has been recognized as a new concept -"Micro Total Analysis (μTAS)" or "Lab-on-a-Chip

(LOC)" by the researchers working in the fields of biosciences and bioengineering. The ultimate goal in the development of μTAS systems is to integrate and combine many laboratory functions such as pumps, mixers, sensors, separators, reagent dispensers, and data analysis in a single integrated and automated microchip that is capable to perform and complete analysis from sample to electrical read-out [24, 25].

The ability to transport species and handling fluids in microchannels with ease and precision is central concept to the μTAS devices [53, 49, 45]. Much attention has been focused on micropump research, not only for their use in μTAS systems, but also for a large variety of applications such as: aerospace and aircraft engineering, medical devices, pharmaceutical and cosmetics, paints and inks, food and beverage, environmental, energy and fuel, electronics, clinical and analytical lab [73].

Fluidic micropumps fall into two categories: mechanical micropumps and non-mechanical micropumps. Mechanical micropumps have large dimensions (up to few centimeters) and moving parts that reduce their reliability and increase the packing sizes, which make these types of micropump difficult to be integrated in microchips. Non-mechanical micropumps are characterised not only by smaller sizes and non-moving parts, but also steady fluid flows, accuracy, low power consumption and a long life time. Non-mechanical micropumps involve the use of the electric fields to move the fluid flow including: electrowetting micropumps, electrohydrodynamic micropumps, and electroosmoosis micropumps, with limitations in each case. Electrowetting micropumps suffer from fluid evaporation. Electrohydrodynamic and DC-electroosmosis micropumps require a very high operating voltage of the order of kilovolts [114]. However, AC-electroosmosis micropumps can generate fluid flow pumping using low voltages ($<$5V). In addition to low applied voltages operation characteristic, they are also characterized with ease in fabrication, portability, integration and scalability. With no doubt, these characteristics make AC-electroosmosis micropumps very attractive to μTAS applications [96]. However, this class of micropumps can only generate slow fluid flow, insufficient back-pressure, and have limited life time as the electrodes undergo chemical reactions.

1.2 Motivation & Objective

A wide range of micropumps were studied previously, which varies in fabrication complexity and operation conditions. Mechanical micropumps can generate high fluid flow, but they are very complicated to be made as they require many layers. In addition to an external electric source as they require high operation voltages. Moreover, moving parts in mechanical micropumps are serious concern for long-term reliability. These factors, limit the mechanical micropump to be integrated and scaled in a lab-on-a-chip device. However non-mechanical micropumps, may be scaled and integrated easily in a lab-on-a-chip device, however they can actuate in different liquid conductivities and operational voltages. The voltage required to operate a micropump is an important factor to be considered, mainly for the portability of the device, where batteries would be used. Electrohydrodynamic, and DC-electroosmosis micropumps, require high voltages to operate (from 100V - kV), as consequence, are subjected to Joule effect which may affect bio-particles.

AC-electroosmosis micropumps remain the suitable candidate for lab-on-a-chip applications, as they require low voltages to operate, no Joule effect which may destroy bio-particles, are simply to fabricate, are easy to be scaled and integrated in within a lab-on-a-chip device. However, AC-electroosmosis micropumps can only generate slow fluid flow velocity, and suffer also electrochemical reactions where the electrodes undergo chemical reactions at voltages above 5V.

One possible solution to improve pumping capability of AC-electroomosis micropumps is by implementing 3D-High Aspect Ratio (HAR) pillars on top of previously designed planar asymmetric electrodes. Since AC-electroosmosis is a surface driven effect, increasing the surface area of the electrodes increases the power coupled into the fluid movement. The physical mechanism of AC-electroosmosis is the motion of induced Electrical Double Layers (EDL) on microelectrodes driven into motion by the electric field generated by the electrodes. By taking the channel volume and filling it with conductive pillars, the surface area therefore increases, but the volume remains the same,

increasing the drive per unit volume. Consequently, this will have the effect of increasing the pumping capability.

To explore and fabricate the proposed pumping principle and produce an innovative pumping solution, Carbon-MEMS fabrication process was involved. During this process a high-aspect-ratio structure can be made out of a chemically resistive polymer and then converting it to a conductive electrodes. Taking the advantage of chemical resistance of the polymer makes the electrodes resistive to electrolysis effect upon applying an electric potential.

1.3 Main Contributions

A new 3D AC-electroosomsis micropump design based on previous planar electrodes approach is proposed in this study. The major contributions of this research are presented in this section.

A New design based on 3D high-aspect-ratio electrodes is proposed, where an intense array of 3D-electrodes are implemented inside a microfluidic channel.

The fabrication of High aspect ratio electrodes is being always a problem in microfabrication techniques due to the difficulties of electroplating process for small and thick features, and also the problem associated with the moulds. To avoid these problems and others, we adopted successfully C-MEMS technology which was previously used in making microbatteries, now we introduced it to microfluidic field. The use of C-MEMS allow us to convert polymers to a conductive polymers.

Due the high aspect ratio features requirements, a thick photoresist is required. SU-8 photoresist was the best candidate for making high-aspect-ratio electrodes due to its chemical, mechanical, and optical characteristics. The only problem associated with the SU-8 is the cost, therefore due to the intensive use to SU-8 photoresist in our experiments, we successfully manged to make and calibrate different home-made SU-8 formulations in our cleanroom.

Although SU-8 photoresist has numerous advantages, but making high-aspect-ratio intense array of pillars was not a straightforward process using SU-8. In this research a process of making high aspect ratio pillars of more than 10:1 was developed using standard UV-lithography techniques, where all the problems raised during the fabrication process were successfully solved and explained. 60 μm thick electrodes with an aspect ratio of 12:1, with a distance of less than 15μm between conductive SU-8 pillars was achieved. Moreover, the conductive pillars were connected internally (between each others) and externally (to outside pads) using planar layers of converted SU-8 photoresist. A layer-by-layer techniques was used to combine many layers of SU-8 photoresist, where many problems were raised during the process in particular the alignment problem. All theses problems were also successfully solved. The last stage in the fabrication process was the packaging. Due to the small dimensions of the electrodes, an SU-8 fluidic channel was implemented on top of the electrodes after performing the electrical test on the electrodes to finally make a full device using only SU-8.

Finally, intensive tests were carried out on the fabricated devices, we have shown that a fluid pumping can be produced using converted polymer structures (C-MEMS). The new 3D-electrodes AC-electroosmosis micropump design has shown an increase of 5 times on the previous planar electrodes design.

1.4 Thesis Overview

- Chapter 2: ***Fluidic micropumps***

  In this chapter, an introduction to fluidic micropumps is given, different types of micropump are presented and classified to mechanical and non mechanical. Both categories of micropumps are compared in terms of efficiency and time life. Moreover a comparison between non-mechanical micropumps is also presented.

- Chapter 3: ***Electroosmotic flow: background and theory***

  The basic component in the AC-electroosmosis pumping is the Electrical Double Layer. In this chapter the electrical double layer formation and its structure are

explained. Theoretical background behind the AC-electroosmosis pumping mechanism, and the interaction of the electric field with the charges in the Electrical Double Layer are also highlighted.

- Chapter 4: ***A novel 3D AC-electroosmosis micropump***

  In this chapter an overview on the evolution of the AC-electroosmosis pumping designs is given, followed by introducing the new 3D AC-electroosmosis micropump. The design and proposed dimensions of each component of the new AC-electroosmosis micropump are presented. Fabrication flow and fabrication masks and alignment marks designs are also included in this chapter.

- Chapter 5: ***Materials and Methods***

  In this chapter, the appropriate fabrication materials for the new ACEO design are selected, followed by fundamental microfabrication techniques accordingly to the use of each material.

- Chapter 6: ***Preparation and testing of SU-8 photoresist***

  Since SU-8 photoresist will be used intensively in the fabrication, and also the cost of SU-8 is high, therefore it is preferred to produce home-made SU-8 rather than buying the commercial one. In this chapter the preparation of different SU-8 viscosities is shown. Photolithography tests were carried out on different thicknesses of the home-made SU-8 to demonstrate its functionality.

- Chapter 7: ***Device fabrication using C-MEMS Technology***

  In this chapter, the use of C-MEMS technology is presented in order to make a complete device of the novel AC-electroosmotic micropump. This chapter is divided into three main sections, fabrication of planar electrodes, fabrication and optimisation of 3D electrodes, and finally boosting the aspect ratio of the 3D-electrodes. First the planar electrodes were fabricated and their flatness was inspected as they are considered to be the platform of the device. The optimization process toward the fabrication of 3D electrodes was also conducted in this chapter, including the effect of the lithography parameters on the structures shapes. The optimization of the process of 3D electrodes was limited to an aspect ratio of 5:1, in order

to increase the aspect ratio the fabrication process was investigated deeply, and the limitation problems were solved, where an aspect ratio of more than 12:1 was reached. For combination of planar and high aspect ratio electrodes more problems were raised, however, all these problems were engineered and the fabrication of complete device was accomplished successfully. Finally after the electrical inspection and plasma treatment performed on the carbon electrodes, the full device was encapsulated in microfluidic channel.

- Chapter 8: ***Fluid flow induced by nonuniform AC-electric field***
  Materials and methods were evolved in the tests were defined, including the home made setup used to monitor and measure the fluid flow velocity. For a proof of concept, firstly rough tests were conducted on the planar and 3D structures to show the functionality of C-MEMS technology for generating a steady fluid flow first. Then, in order to characterise the device, both carbon electrodes resistance and the electrical double layer impedance were measured in order to model the device. For deep characterization of the device behaviour, different voltages, frequencies, were applied on different devices geometries (planar and 3D with different dimensions) for different conductivities.

- Chapter 9: ***Conclusion and outlook***
  In this chapter concluding remarks on the fabrication processes and the functionality of the AC-electroosmotic pump are presented. Future work and research thrusts are discussed at the end of the chapter.

Chapter 2

Fluidic micropumps

The concept of microfluidic pumps involves handling and manipulation of liquid or gas inside a microchannel and causes hydraulic flow and pressure. The enhancement of microfabrication techniques has a strong influence for the appearances of a wide range of micopumps. According to Laser et, al. [73] micropumps generally fall into one of two classes. The first category is the displacement micropumps, these micropumps exert pressure forces directly on the working fluid by one or more moving boundaries, and also are known as mechanical micropumps. The second category, is dynamic micropumps, which exert forces directly on the liquid without any moving part, and also know as non-mechanical micropumps.

2.1 Mechanical micropumps

Mechanical micropumps, involve mechanical actuators which translate electric energy to mechanical work. The actuators can be external or integrated. Commonly used external actuators are: piezoelectric actuators; electromagnetic with solenoid plunger

actuators; disk type; cantilever type actuators; pneumatic actuators; and shape memory actuators. These actuators are characterized by large sizes which generate a large force and displacement. As a consequence, the size of the overall mechanical micropumps is restricted to the size of the actuators. Also, because, these type of micropumps consist of moving parts which are serious concern for long-term reliability.

The most common used integrated actuators are: electrostatic actuators, electromagnetic actuators and thermopneumatic actuators. Although the electrostatic actuators have a fast response and good reliability, the electrostatic actuators generate a small force and stroke. Electromagnetic actuators require external magnetic field, therefore restricting the size of the pump. In addition, they produce large electric currents in the fluid and cause thermal perturbations and high electric energy consumption. Thermopneumatic actuators produce a high pressure and therefore a large stroke. However, a significant electrical energy is needed to provided the thermal energy. Other major drawbacks are raised, for the fact of complex structures of mechanical micropumps. Therefore, many complex fabrication steps are required as many layers material are involved in the fabrication [88]. This is inconvenient as it increases the cost of the device, and extends the fabrication time.

In general, the basic components in mechanical micropump are a pump chamber (bounded on one side by the pump diaphragm), an actuator-mechanism or driver and two passive check valves: one at the inlet (or suction side) and one at the outlet (or discharge side). As a consequence, many layers are required to fabricate this type of micropumps. Usually micropumps are made from as few as two and as many as seven layers of material [88].

Figure 2.1 shows a basic design and operation of a displacement (mechanical) micropump. During operation, the driver apply force on the pump diaphragm to increase or decrease the pump chamber volume. Fluid is driven into the pump chamber during the chamber expansion or suction stroke and forced out of the pump chamber during the contraction/discharge stroke. The check valves at the inlet and outlet are oriented to favor flow into and out of the pump chamber, respectively, rectifying the flow over

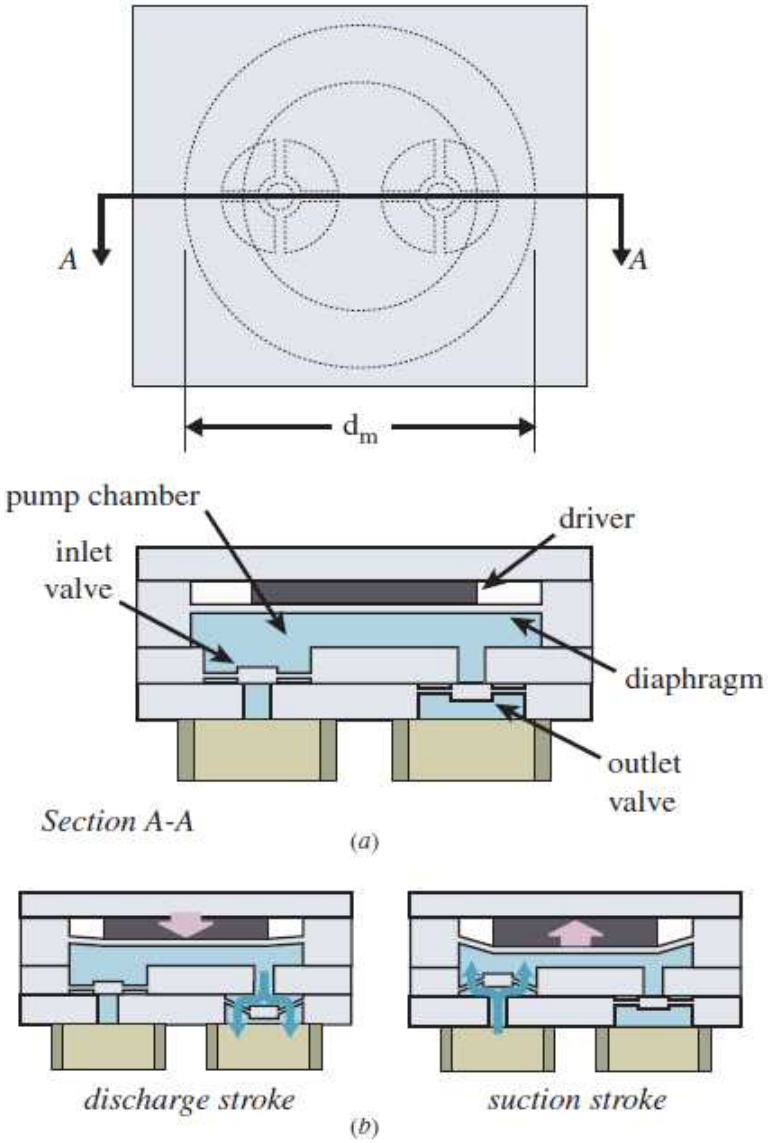

FIGURE 2.1: Structure and operation of a typical reciprocating displacement micropump. (a) Top view and section. (b) Discharge and suction strokes. During the discharge stroke, the driver acts to reduce the pump chamber volume, expelling working fluid through the outlet valve. During the suction stroke, the pump chamber is expanded, drawing working fluid in through the inlet valve [73].

a two-stroke pump cycle [73]. This micropump which was fabricated by Van Lintel et. al [120], comprises a full 2 inch silicon wafer sandwiched between two glass plates with same dimensions, which makes the package size of 4 cm^3 relatively large. The pump chamber is a 12.5mm diameter, 130μm deep cavity etched in the silicon wafer using A 0.19 mm thick glass plate seals the pump chamber side of the device; a thicker piece of

glass seals the other side. The portion of the thin glass plate above the pump chamber is the pump diaphragm; a piezoelectric disk actuator is attached to this glass diaphragm. Usually the required operation voltage for these micropumps is above 100V [73].

2.2 Non-mechanical micropumps

In contrary to mechanical micropumps, non-mechanical micropumps are characterised with simple microstructure, where may induce the fluid flow without using any moving parts of the device. They have been used to reduce waste streams, increase precision and accuracy, and disposability in a continuous fluid flow. Their fundamental working principles rely critically on the electrical proprieties of the fluid (permittivity and conductivity) [129].
The function of non-mechanical pumps is vitally based on the electric field for producing pumping forces. The electrical field can be generated from an AC or DC generators which makes a difference in the functionality of the micropumps themselves. Two categories of micropumps will then be defined in terms of electrical field; the *static* electrical field micropump and the *dynamic* electrical field ones. In terms of fluid characteristics two kinds of pumps can be defined: pumps that use non-conductive fluids such oil and ethanol and which are known as *electrohydrodynamic* micropumps, and *t*he electrokinetic pumps which deal with conductive fluids.

2.2.1 Electrowetting Micropump

Under an applied electric potential, droplet in direct contact with metallic electrodes may result in electrolysis effect. In early 1990, Berge [9] separated metallic electrodes with a thin dielectric layer from fluidic droplet to prevent any electrolysis or corrosion may occur.

The electrowetting technique was originally defined as the change in solid-electrolyte contact angle due to the applied potential difference between the solid and the electrolyte. The idea behind the electrowetting micropumps is to drive liquid droplets instead of fluid

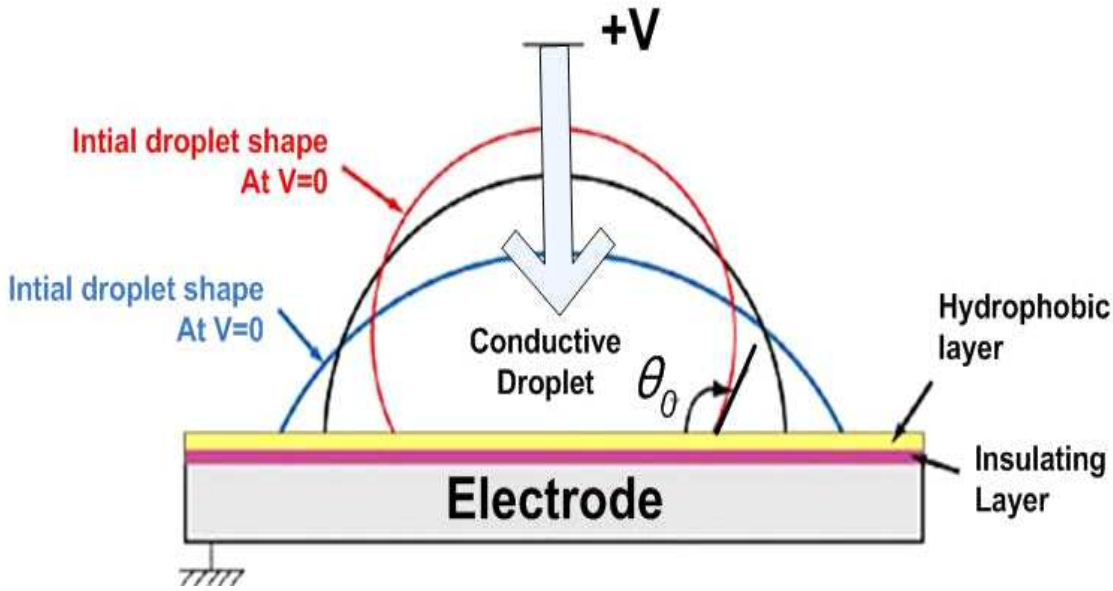

FIGURE 2.2: Principle and phenomena of electrowetting on dielectric(EWOD)

bulks using a set of arrays. Electrowetting arrays allow large numbers of droplets to be independently manipulated under direct electrical control without the use of membranes, valves or even fixed channels. This approach illuminates many problems such as leakage and hence bubbles, bounding of the channel deficiencies. Digital fluid circuits are made possible by the ability to manipulate fluid droplet from the range of picolitre to the range of microlitre [82, 104]. Although electrowetting are effective for transporting finite quantities of fluid in a generally unidirectional manner, However, they suffer from a serious disadvantage which is the volatile nature of liquids.

2.2.2 Electrohydrodynamic micropump

In electrohydrodynamic (EHD) micropumps the electrical field is used to transport dielectric fluids. Pumping effect in EHD micropumps rely critically on the electrical properties of the fluid. Typical electrical conductivity of the fluid must remain between 10^{-14} and 10^{-9} S/cm [88]. EHD micropumps require also either a free space charge within the fluid or a gradient in the permittivity. Therefore, depending on the dominant

process used, the way of the space charge is introduced and the kind of the driven voltage, different pumps can be produced [103]. Despite, there is a large number of EHD micropumps, the three main types are injection EHD, conduction EHD, and induction EHD micropumps. The critical disadvantage of these micropumps, is their operational voltage which lies in the range of kilovolts.

2.2.2.1 Electrohydrodynamic Injection pump

Much effort was put on injection pumping mechanism, it was firstly studied experimentally and theoretically by Stuetzer, et. al. [113, 112] and Pickard et. al. [94, 95]. Then fabricated and characterised by Richter et al. [102] and Darabi et al. [34]. The injection pump, also known as ion-drag pump, uses the interaction of an electric field with electric charges injected into a dielectric fluid (highly insulating liquids in the order of $10^{-}9Sm^{-1}$). This micropump consists mainly of two electrodes, the first one called emitter and the other one collector. Upon the application of high electric field The emitter supplies ions that are driven by electric field toward the collector placed far away from the emitter. While the ions move, they drag the working fluid by friction. According to Darabi et al. [34] ion-drag micropump has shown a good performance in pumping liquid nitrogen, this is due to its very stable molecular structure. However the use of other working fluids at the presence of high applied voltages (> 100V) can change the liquid electrical properties, and damage the electrodes. These effects can reduce this micropump life time.

2.2.2.2 Electrohydrodynamic induction micropumps

In this micropump family, charge is induced in an inhomogeneous liquid by the electric field, as a consequence the generated electric force is transmitted to the electrolyte. The electrolyte inhomogeneity can be achieved by imposing a gradient of temperature. Liquid conductivity depends on temperature since the ionic mobilities are inversely proportional to viscosity (that depends on temperature) the dissociation rate of neutral molecules also depends on temperature. The common induction pump consists of a set of planar

electrodes array, that can be subjected to a traveling wave potential together with a vertical gradient of temperature as it can be seen in Figure 2.3 [58].

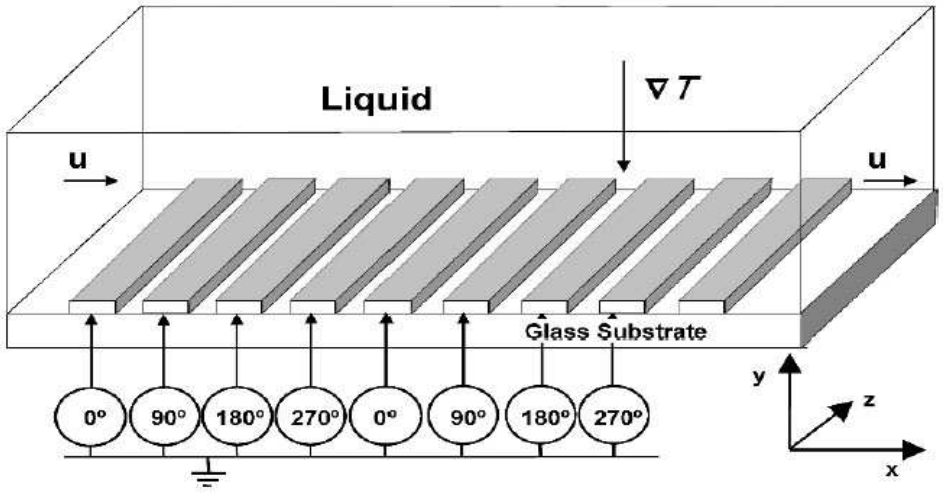

FIGURE 2.3: A schematic of traveling wave induction micropump under the influence of traveling wave potential and vertical gradient of temperature [58]

The temperature gradient may be obtained either by the Joule heating generated from the applied electric field or by an externally applied temperature gradient [40, 41, 87]. But, recently, an induction pump was made by using an external gradient of temperature[38]. With the presence of longitudinal temperature gradient, and under the influence of a single phase signal, a unidirectional fluid motion can be generated with this type of micropumps [52, 48]. However, for a proper functionality of the micropump, the electrolyte has to be conductive. A wide range of conductivities can be used for this micropump which varies from 10^{-9} to 1 Sm^{-1} [58]. However, at high electrolyte conductivities, if a high electric field is applied, the temperature may excessively increase. This is considered as a disadvantage since high temperature affects bio-particles such as cells, DNA, viruses, and bacteria in μTAS applications [46, 39]. In addition, if the electric field is high enough, the fluid flow becomes instable, and formation of gas bubbles takes place in the microchannel, especially at low frequencies [41].

2.2.3 Electroosmosis micropump

Electroosmosis refers to the bulk movement of an electrolyte past a stationary solid surface, as a result of an externally applied electric field. At the interface between solid surface and electrolytes, a thin layer of charges and ions are formed, this layer is known as electrical double layer as a results of the electrochemical differences in potentials of both phases [61]. At this stage, the solid surface becomes charged and counterions attracted from the electrolyte screened this surface charge. At equilibrium, the electrostatic attraction between the charged surface and the counterions is balanced by thermal agitation. This results to an electrically neutral electrolyte and a charged electrical layer at the interface solid/electrolyte [58].

The application of an electric field along the solid surface produces a Coulomb force on the electrical double layer, as a consequence a fluid motion can be generated. Usually the thickness of the Debye layer is very small (1-100 nm in water), therefore the electric force is considered as a superficial force [58]. With regards to the applied electric field two kinds of electroosmosis micropumps can be distinguished: DC-electroosmosis and AC-electroosmosis.

2.2.3.1 DC-electroosmosis micropump

Usually electroosmosis micropumps are glass-made, in the case of silica based ceramics, when immersed in electrolyte with pH greater than 4, a part of silanol groups (SiOH) at the surface deprotonate, and results in a net negatively charged surface [73]. As a consequence, the ions in the liquid redistribute and result in electrically neutral liquid bulk while a positive diffuse charge layer appears close to the surface [58], this can be seen clearly in Figure 2.4. By applying a high DC signal between the electrodes, an electric field is generated along the surface and causes the ions of the diffuse layer to move towards the electrode of opposite sign, however the negatively charged SiO^- groups remain immobile as they are bounded to the solid surface by covalent bonds. While the mobile ions migrate, they drag the fluid with them and result in a bulk flow.

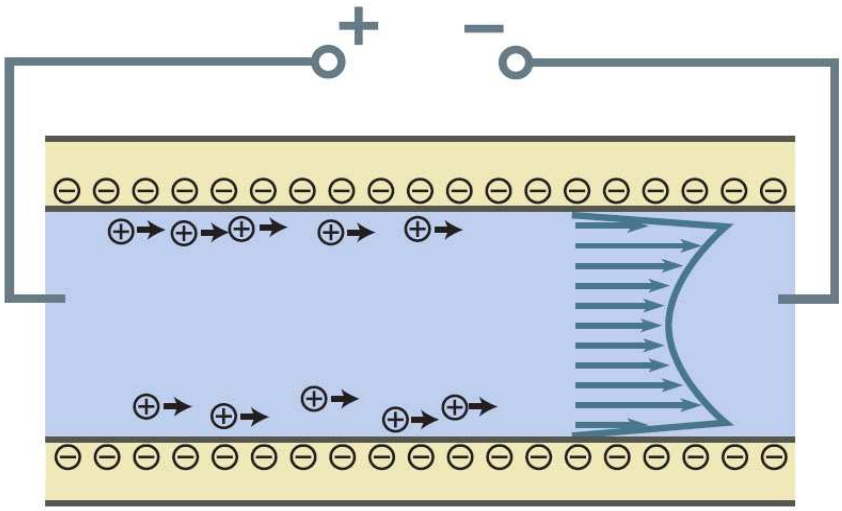

FIGURE 2.4: A schematic shows an externally applied electric field causes motion of counter ions that shield a negative wall charge [73].

According to Laser et al. [73] the key factors that affect the performance of electroosmosis pumps are: the magnitude of the applied electric field and applied electric potential, the cross-sectional dimensions of the microchannel in which flow is generated, the surface charge density of the solid surface that is in contact with the electrolyte, and ions density and pH of the electrolyte.

The operation voltage in the DC-electroosmosis micropumps is very high usually in the kilovolt range, this is considered as a drawback, as it requires relatively large external source which limits its portability and integrity in a chip. Also the application of high electric potential to metallic electrodes, results to electrolysis problem and gas bubbles generation. Redox reactions at the electrodes will vary the pH value, which is considered a problem as DC-electroosmosis flow depends on it.

2.2.3.2 AC-electroosmosis micropump

An AC-electroosmotic micropump involves the use of the Coulomb force on the induced-charge in the double layer [84, 99, 1]. The fluid movement occurs in the presence of parallel electrical field, and it is due to the influence of the electrical field on the electrical double layer [84]. The normal component of the electric field charges the double layer at

the electrode/electrolyte interface, while the tangential electric field component produces a force on the induced charge in the diffuse layer that results in fluid motion [50, 47, 51].

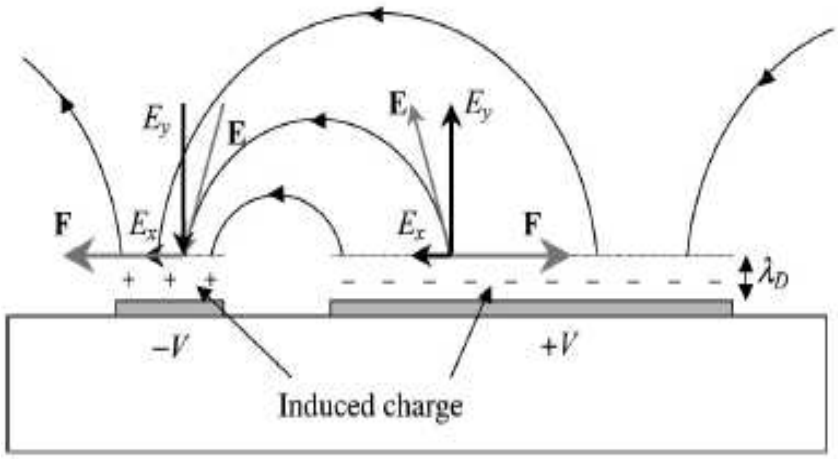

FIGURE 2.5: Schematic diagram of the physical mechanism of AC-electroosmosis in an asymmetric electrode array [96].

Unidirectional fluid flow can be generated either by employing arrays of asymmetric pairs of planar electrodes subjected to a single AC signal [50] or arrays of symmetric electrodes subjected to traveling-wave signals [22]. The Ac-electroosmosis micropump performance is dictated by substrate material and geometry as well as the fluid properties. However, fluid conductivity has to be kept low, as the fluid flow velocity reduces as the conductivity increases (usually in the range of $10^{-4} - 0.1 Sm^{-1}$) [58].

Although AC-electroosmosis micropumps show very good performance in terms of power consumption, a considerable small sizes in comparison to a wide range of micropumps. but they suffer from some drawbacks. The applied voltage has to be kept low in order to avoid electrochemical reactions since the electrodes are in direct contact with the electrolyte. After a long run of the micropump, the Faradaic reactions can degrade the electrodes state[58], while covering them with a dielectric photoresist may affect the capacitance of the AC-electroosmosis mechanism [70].

Chapter 3

Electroosmotic flow: background and theory

Usually solid surfaces have an electric charge. When an electrolyte comes in contact with a solid surface in a fluidic microchannel, an electric double layer of counter ions will form at the solid surface. When a tangential electric field is applied across the channel, the ions in the double layer move towards the electrode of opposite polarity. The movement of ions in the electrical double layer drag the fluid and generate the so called electroosmosis fluid flow in the microchannel.

This chapter presents the theory behind the electroosmosis effect, along with a description of the electrical double layer model and the electrodes polarisation. Also presented is an explanation of AC-electroosmosis and the fluid mechanic forces acting on the fluid.

3.1 Fluid mechanics

The main governing equations in fluid dynamics are the continuity and the Navier-Stokes equations. These equations are restricted to the assumption that the fluid is a continuum [84]. This is because the molecular spacing λ_{mol} is very small compared to the length scales considered. The molecular spacing λ_{mol} is given by [17]:

$$\lambda_{mol} = \sqrt[3]{\frac{M}{\rho N_A}} \tag{3.1}$$

Where: M: is the molar mass (g.mol^{-1}), ρ: is the mass density (kg.m^{-3}), and N_A: is Avogadros number (6.022 x $10^{-23} mol^{-1}$)

3.1.1 Mass conservation

The conservation of mass equation states that at all times the mass entering the control volume is equal to the mass leaving the control volume, and is given by [17]:

$$\frac{\partial \rho}{\partial t} + \nabla \cdot (\rho u) = 0 \tag{3.2}$$

where, u (m.s^{-1}) is the velocity vector.
If the mass density ρ is constant then the fluid is incompressible, hence the continuity equation becomes [47]:

$$\nabla \cdot u = 0 \tag{3.3}$$

3.1.2 Momentum conservation

This equation is derived from Newton's law for fluids. The equation establishes that the rate of change of the momentum of a fluid particle is equal to the sum of the forces acting on it. The acting forces on the fluid particles are: the body forces, the pressure and viscous forces. This dynamical statement of the balance of forces acting at any

given region of the fluid is called Navier-Stokes equation, and is given as:

$$\underbrace{\rho\frac{\partial u}{\partial t}}_{Acceleration} + \underbrace{\rho u \cdot \nabla u}_{inertial} = \underbrace{-\nabla P}_{Pressure} + \underbrace{\eta\nabla^2 u}_{Viscous forces} + \rho \underbrace{f}_{Body forces} \tag{3.4}$$

ρ: is the mass density, u: is the velocity, P: is the pressure, η: is the viscosity coefficient, f: is the body force. This form of the Navier-Stokes equation is generally valid for incompressible Newtonian fluids.

3.1.3 Reynolds number

Navier-Stokes equation contains nonlinear inertia terms or (convective terms), a measure for the ratio between inertial and viscous forces is the Reynolds number and is defined as:

$$Re = \frac{\rho u}{\mu / L} \tag{3.5}$$

where L and u are the characteristic length and velocity, respectively, and μ is Kinematic viscosity ($m^2.s^{-1}$).

Reymolds number characterizes the behaviour of the fluid flow in the microchannel. If the Reynold number is high the fluid flow is defined as turbulent, however, if Reynold number is low the fluid flow is considered laminar. In microfluidics the flow is generally laminar due to the viscose forces which dominant in microscale domain, and also to the small velocities u resulting to a small Reynolds number.

3.2 Electrical double layer and surfaces

Most of microfluidic devices are made from silica based ceramics (such as glass or silicon) and metals. The surfaces of these solid materials carry a net charge that may be acquired through a variety of mechanisms, mainly disassociation of the chemical groups on the surface and by ion adsorption. This net charge on the solid surfaces creates an electrostatic potential ϕ_o local to the interface [84]. When the solid surface comes in contact with the electrolyte, the electrostatic potential ϕ_o attracts the opposite charged

ions (counter-ions), and repels ions with the same charge (co-ions) in the fluid, and as a results a thin layer of ions is created. This layer of ion which is formed between the solid surface and electrolyte interface is referred to as the *Electrical Double layer*.

There are several types of effect that lead to charge separation at interfaces and the resulting formation of electrical double layer [32].

- Charge accumulation due to ion adsorption.
- Charge generation by chemical ionization.
- Charge generation at electrode metal surfaces.

3.2.1 Electrical double layer

The electrical double layer is a central concept in the understanding of the electrokinetics mechanism. According to the classical theoretical model of electrical double layer (Gouy-Chapman-Stern model), it consists of two different layers: Diffuse layer and Stern Layer. The diffuse layer is being a layer of ions that is adjacent to the solution region, the ions in this region are not static, they undergo thermal motion. Following the diffuse layer, Stern layer or bound region (also called compact layer), which is is referred to the region between the solid surface and the diffuse layer, this region is of the order of one to two solvated ions thick. The Stern layer itself can be subdivided into two regions. The inner Helmholtz Plane (iHP), which consists of the ions which are not hydrated and have adsorbed to the solid surface. Where the second region is called the outer Helmholtz Plane (oHP), that consists of bond hydrated ions, this electrical double layer model is well known as Gouy-Chapman-Stern model (see Figure 3.1). The electrical double layer acts as an electrical capacitor. If the surface potential is increased, the surface charge density increases also. The double layer capacitance given by the series combination of the Stern layer capacitance C_s and the Diffuse layer capacitance C_d [133, 127]:

$$\frac{1}{C_{DL}} = \frac{1}{C_s} + \frac{1}{C_d} \tag{3.6}$$

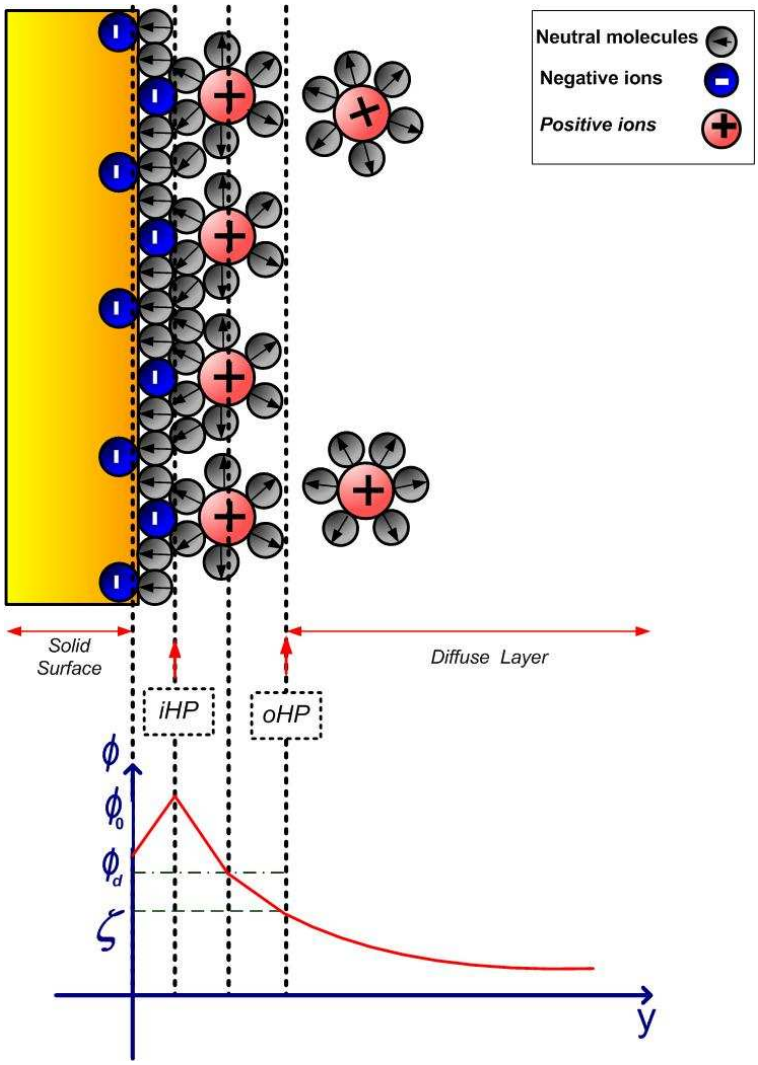

FIGURE 3.1: Schematic model of the electrical double layer, showing the distribution of ions in different layers, including adsorbed negative ions, bounded by inner Helmholtz plane iHP and hydrated charges bounded by the outer Helmholtz plane oHP on a negatively charged surface [84, 133]

.

The schematic diagram that is depicted by Figure 3.1 shows the internal structure of the electrical double layer, and the variation of the potential ϕ across it. The potential decays exponentially through the diffuse layer [84]. The thickness of the electrical double layer may be estimated by considering a balance of electrical potential energy and thermal energy (diffusion) and is well known as Debye length. The Debye length is found by balancing repulsive diffusive forces with attractive electrical forces as follows [84]:

$$\lambda_D = \frac{1}{\kappa} = \sqrt{\frac{\epsilon k_B T}{2z^2 q^2 n_0}} \tag{3.7}$$

where: ϵ is the material permittivity (C.(V.m)$^{-1}$), z is the ion valence number, n_0 is the bulk ion concentration in $mol \cdot m^{-3}$, k_B is Boltzman constant (1.381 x 10^{-23} J.K^{-1}), T is the absolute temperature (K), q is the elementary charge (C). The thickness of λ_D is of the order of few nanometers (e.g. 1-100nm in water)

Figure 3.1 shows also Zeta potential which is the effective potential for the diffuse layer and the value of the solid surface potential at the shear plane above stern layer. Zeta potential is defined as the potential difference across the Debye layer from the shear surface between the charged surface and the electrolyte to the far field.

3.2.2 Electrode polarisation and Electrical Double layer impedance

The electrodes inside a microfluidic channel that come in contact with liquid, will end up with formation of electrical double layer at the interface electrode-electrolyte. The accumulated charges of the electrical double layer behaves as a capacitor with nonuniform charge density, where the potential across the electrical double layer decays exponentially from the maximum at the electrode to nearly zero in the bulk (see Figure 3.1). By applying an external potential to the electrodes the charge distribution changes and the capacitor charges, this phenomenon is referred to as *Electrode Polarisation* [99, 84, 33]. The electrodes polarisation prevents the electrical potential influence on the bulk electrolyte, where the applied potential is dropped across the capacitor and the potential in the bulk electrolyte is only a fraction of the applied one [84].

The electrical double layer impedance can be represented by an equivalent electrical circuit composed of a resistor R_{DL} and capacitor C_{DL} in series as it can be seen in Figure 3.2, although this is a simplified circuit model since the electrochemical reactions at the electrode surface can be ignored. The electrical double layer formation mechanism is inherently related to the solid surface characteristics (such as roughness, uniformity, porosity,...), which results in the variation of Debye length of the electrical double layer.

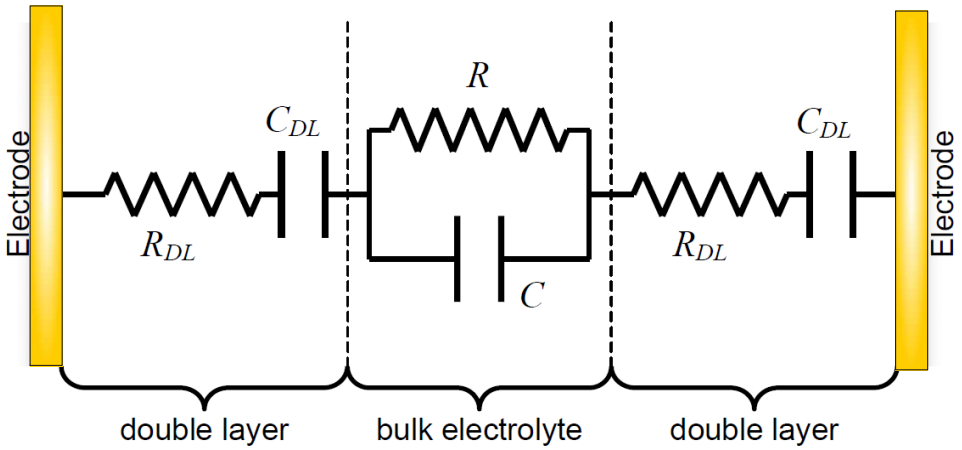

FIGURE 3.2: Circuit diagram illustrates the electrical model of the double layer and a bulk electrolyte. The double layer can be represented by Capacitor C_{DL} in series with a resistor R_{DL} at each surface of the electrodes. The electrolyte can be considered to consist of capacitor and C parallel to resistor R, which is in series with the double layer impedance [84].

If the surface of the electrodes is porous or nonuniform, the electrical double layer polarisation impedance is given by [84]:

$$Z_{DL} = \frac{A}{(i\omega)^{\beta}} = \frac{A}{\omega^{\beta}}[Cos(\frac{\pi}{2}\beta) - iSin(\frac{\pi}{2}\beta)] \tag{3.8}$$

A and β are constants. For perfect capacitor $\beta = 1$ and for perfect resistor $\beta = 0$. β is typically found to be between 0.7 and 0.9 on solid electrodes.

The impedance Z_{DL} is also know as the Constant Phase Angle Element (CPE), the origin and use of CPE has been extensively discussed in the literature [137, 19, 71, 28, 36]

3.3 Electroosmosis

In a microfluidic channel, due to the contact of fluid to the solid surfaces, an electrically charged thin double layer is formed near to the solid surfaces. Application of a tangential electric field along the channel causes all electric charges to be attracted towards the electrode of opposite sign. The charges in the diffuse layer of the electrical double layer experience a force. As a result of this force, these double layer ions move. Since the

viscous effect of liquid is dominant in microscale, the migration of the ions causes a fluid movement inside of the channel by way of momentum transfer. As a result, a bulk flow is produced in the microchannel. This fluid flow phenomenon generated by electric field is called the electroosmosis phenomena.

In electroosmosis flow, Reynold number is relatively small to the viscous term, also the pressure and the velocity remain constant in x direction, therefore the equation 3.4 can be simplified to:

$$\eta \frac{\partial^2 u}{\partial y^2} = -\rho E_t \tag{3.9}$$

where, u is the fluid flow velocity at x direction.
Combining equation 3.9 with the Gauss's law results to:

$$\eta \frac{\partial^2 u}{\partial y^2} = \epsilon \frac{\partial^2 \phi}{\partial y^2} E_t \tag{3.10}$$

where ϵ is the permittivity of the medium.

By taking the following boundary conditions in consideration:
$\phi = \zeta$ at $u = 0$
$\frac{\partial \phi}{\partial y} = 0$ as $y \to \infty$

Integrating equation 3.10 twice, gives:

$$u = \frac{\epsilon E_t \zeta}{\eta} \tag{3.11}$$

The application of an electrical potential difference across the system, leads the mobile ions to drag fluid, the velocity field of the fluid is as function of an external electric field. The equation 3.11 which describes this effect is well known as Helmholtz-Smoluchowski slip velocity, which is proportional to the tangential electric field, and the zeta potential.

3.3.1 AC-Electroosmosis

AC-electroosmosis flow generation was first observed by Ramos et al. [99] during the AC-electrokinetic manipulation of particles in suspension on microelectrode structures, where a strong frequency-dependent fluid flow was observed. It was first thought that the source of the flow was the heating of the electrolyte that was generated by the electric field. Since fluid heating creates gradient in permittivity and conductivity of the fluid, which in turn may give rise to electrical volume forces well know as electrothermal. However, the fluid flow that can be generated by electrothermal mechanism is relatively slow, and can not explain the observed frequency-dependent fluid motion[96, 98]. This mechanism was similar in behavior to DC-electroosmosis [55], therefore it was termed AC-electroosmosis due to the application of AC signal [99]. AC-electroosmosis is also a surface driving effect, it employs the electrical double layer that is formed on top of the electrodes surface to generate fluid flow. The fluid flow motion is generated under the action of the non-uniform electric field on the diffuse layer.

In order to explain AC-electroosmosis pumping mechanism, a pair of parallel symmetrical planar electrodes is used. Upon the application of an AC signal to the electrodes, an electric field is generated. Both components of the electric field (normal and tangential) contribute in the flow generation. The normal component induces the charges on top of the electrodes, while the tangential component produces a force on the induced charge in the electrical double layer in the opposite electrode makes use of Coulomb forces (as it can be seen in Figure 3.3(a)). As the ions and charged molecules in the opposite electrode move, they drag the fluid making use of the strong viscous forces in microscale. The motion of the electrical double layer results in rotating vortices (roles) on top of the electrodes. The rotation of roles and the trajectory of the fluid can be monitored by the motion of tracer particles as it can be seen in Figure 3.3(b) [96]. The particles move down from the bulk into the inter-electrodes gap and out onto the electrodes surface. In addition to the AC-electroosmosis flow dependency to the frequency, it was also observed to vary with the position to the electrodes [96]. Figure 3.4 shows that the motion of the tracer particle on top of planar electrodes is maximum close to the inner electrodes edges and decreases as the distance from the electrodes edges increases.

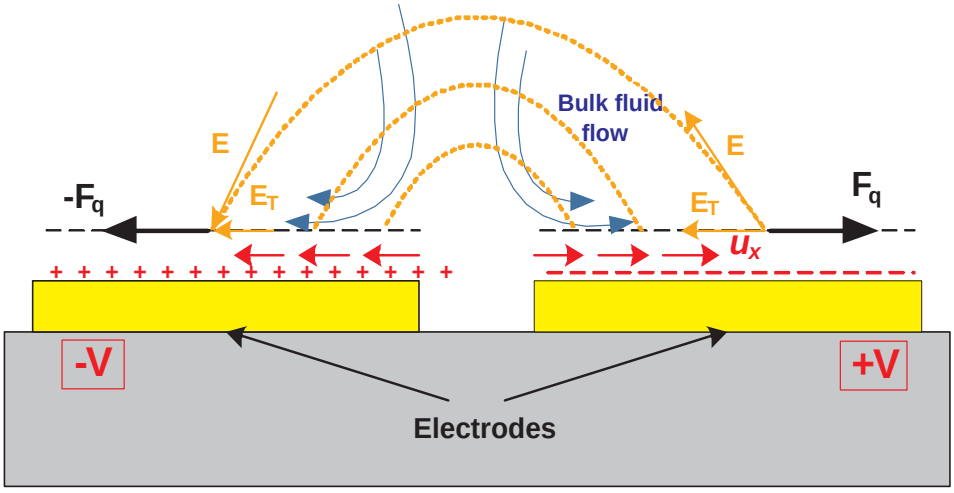

(a) Schismatic of the electric field and fluid flow directions

(b) Flow motion on top of the electrodes

FIGURE 3.3: Fluid flow on top of planar symmetric electrodes. On the left schematics of electric field distribution and fluidic motion. On the right, fluidic roles on top of planar electrodes showing the generation of fluid flow in microchannel [96]

It can also be seen in Figure 3.4 that the magnitude of the fluid varies as a function of the frequency, but the direction of the fluid flow on top of the electrodes remains always constant if the applied signal switches to the opposite sign (as it is alternating current).

According to Green et al. [96] the magnitude of the fluid flow velocity on top of the electrodes depends on the applied frequency and voltages. It can be seen clearly in Figure 3.5 that the applied voltage is proportional to the AC-electroosmosis velocity

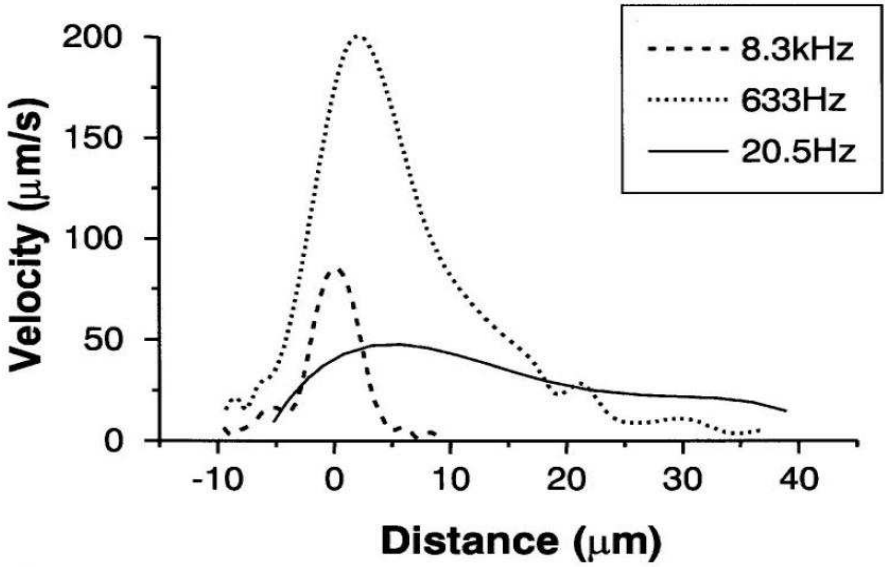

FIGURE 3.4: Graphs show the movement of particles on the top of the electrodes at different frequencies. The movement is maximum close to the electrode edge, and decreases as the distance from the electrode edge increases. As the frequency varies the fluid fluid flow velocity changes showing the velocity dependency to the frequency [50]

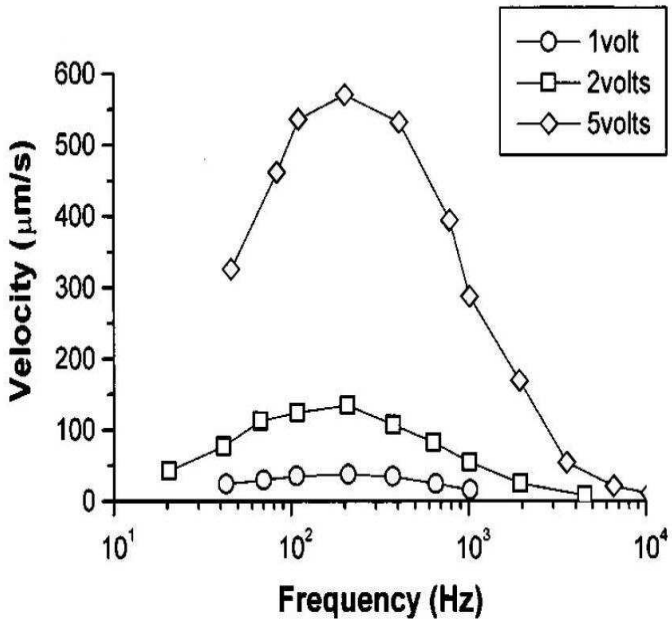

FIGURE 3.5: Graphs show the movement of latex particles on the top of planar symmetrical electrodes at different frequencies and voltages. [50]

where the fluid flow increases as a function of the voltage. The velocity also increases at intermediate frequencies and decreases at low and high frequencies.

3.3.2 AC-Electroosmosis flow velocity

Based on the equation 3.11, in the linear approximation, the zeta potential is proportional to the surface charge density in the diffuse double layer σ_q therefore equation 3.11 becomes:

$$u = \frac{\epsilon E_t \sigma_q}{\kappa \eta} \tag{3.12}$$

where κ is the reciprocal Debaye length.

The equation 3.12 can be only applied to estimate the fluid flow velocity for a given value of the tangential field and surface charge density. In classical electroosmosis the driving field is constant throughout the medium and tangential to the surface. However in the case of a nonuniform electric field, the "x" component of the field E_t lies tangentially to the electrode surface, as illustrated in Figure 3.3(a). The charge in the diffuse double layer can be represented as a time dependent excess charge constant, $\Delta\sigma_q(t)$ which changes with the variation of the electric field.

By neglecting the compact layer in the linear approximation the excess charge can be estimated to be:

$$\Delta\sigma_q = \epsilon\kappa\phi_{DL} \tag{3.13}$$

where ϕ_{DL} is the induced potential across the double layer.

An AC-electroosmosis system consists of electrodes, electrolyte in association with electrical double layer, can be modeled by an RC circuit. Assuming that the electrodes are ideally polarisable and no chemical reactions occur on the surface of the electrodes. A simplified equivalent electrical model of the whole system can be presented by multiple parallel capacitor-resistor-capacitor (C-R-C) combinations. Figure 3.6) shows the capacitors distribution over a pair of electrodes connected to resistive tubes. Each capacitor

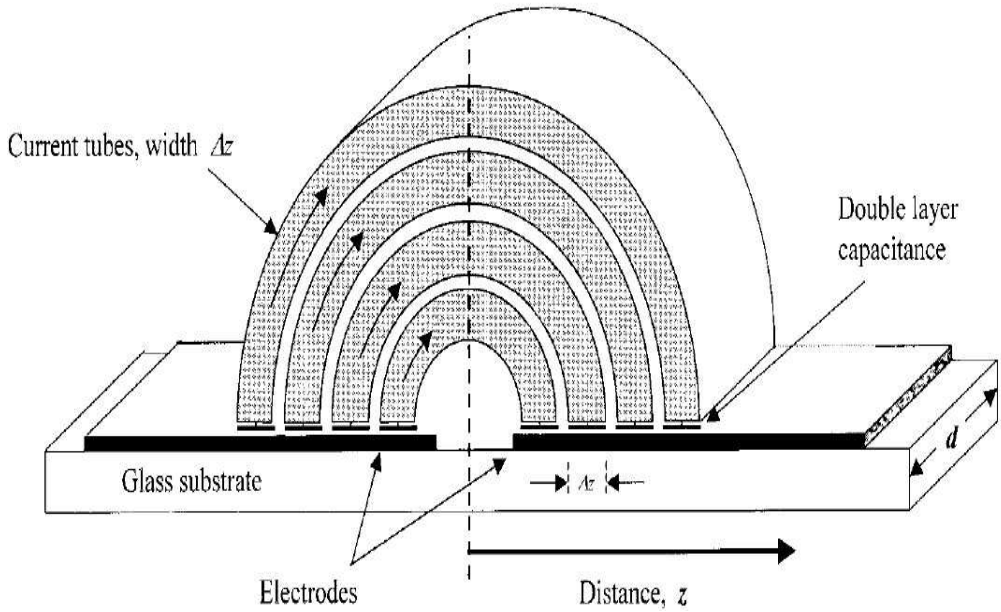

FIGURE 3.6: Schematic shows a simple electrical model illustrating the concept of current flux tubes connected to electrical double layer capacitors [99].

has a constant value given by:

$$\Delta C = \epsilon \kappa d \Delta z \tag{3.14}$$

where d is the electrode length.

The electrolyte impedance is purely resistive at low frequencies, and the resistance of each tube is given by:

$$R(z) = \frac{\pi z}{\sigma d \Delta z} \tag{3.15}$$

Each incremental capacitor charges over a resistor, however their charging time is different since each incremental flux tube is different in length. The potentials dropped across the electrical double layer and the electrolyte

Subsequently, the potentials dropped across the electrical double layer and the electrolyte as a function of distance z can then be obtained [84, 98]:

$$\Delta\phi_{DL} = \frac{V_0}{2 + i\omega\pi z(\epsilon/\sigma)\kappa} \tag{3.16}$$

where V_0 is the amplitude of the applied AC potential, ω is the frequency, σ is the conductivity of the medium, ϵ is the permitivity, κ^{-1} is the Debye length of the electrical double layer.

The charge density for this model can be evaluated as $\Delta\sigma_q(z) = \epsilon\kappa\phi_{DL}$ where the tangential field is:

$$E_t = -\frac{\partial\phi_{DL}}{\partial z} \tag{3.17}$$

From equation 3.12, the time averaged electroosmotic velocity is then:

$$\langle u\rangle = \frac{1}{2}Re\left\{\frac{\Delta\sigma_q E_t^*}{\eta\kappa}\right\} = \frac{1}{8}\frac{\epsilon V_o^2\Omega^2}{\eta z(1+\Omega^2)^2} \tag{3.18}$$

where

$$\Omega = \omega\frac{\epsilon}{\sigma}\frac{\pi}{2}z\kappa \tag{3.19}$$

The equation 3.18 explains the variation in velocity as a function of frequency and distance. It gives a bell-shaped profile for the frequency dependence of the AC-eletroosmosis velocity flow, which goes to minimum values at low and high frequency limits where a maximum velocity can be achieved at $\Omega = 1$ [99]. Figure 3.7 shows the experimental velocities for fluid at 5 V_{pp} [50].

The AC-electroosmosis flow velocity profile can be explained by the behavior of the electrical double layer. Based on the equivalent RC circuit model, three different cases can be distinguished:

- Low frequencies: at each cycle the double layer has sufficient time to entirely form on top of the electrode, as a consequence the applied signal is totally dropped at

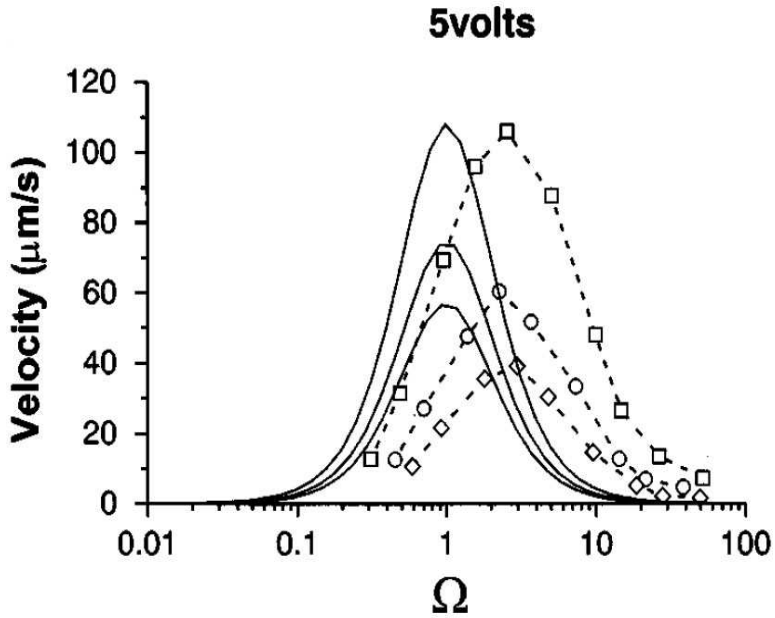

FIGURE 3.7: Graphs show the velocity profile of the fluid flow velocity on top of planar electrodes as a variation of Ω at deffirent position to the electrode edge. The applied voltage is 5 V_{pp}, a maximum velocity can be achieved at $\Omega = 1$, the dashed lines represent the experimental data and the theoretical results are plotted as solid lines [50]

the electrical double layer. therefore no electroosmosis flow can be seen at low frequencies.

- High frequencies: the double layer has no time to form on top of the electrodes, therefore the applied signal is equal to the signal in the electrolyte. Subsequently no fluid flow can be generated at high frequencies.

- At intermediate frequencies: there is a transition between these two limits, the potential across the electrolyte decreases as the applied voltage decreases [84, 50]. The presence of the electrical double layer at this stage leads to generate an AC-electroosmosis flow.

3.4 AC-Electroosmosis micropumps

3.4.1 AC-Electroosmosis micropump using symmetric electrodes

AC-electroosmosis micropump using symmetrical pair of electrodes was first studied experimentally and theoretically by Green and Ramos et. al. [47, 50, 51] using 2mm long and 100μm wide parallel electrodes separated by 25μm gap. However with this type of pumping can only generate a local fluid flow on top of the electrodes (as seen in section 3.3.1). Pairs of planar electrodes were fabricated on a glass substrate using photolithography fabrication process combined 10 nm titanium, 100 nm gold, and 20 nm titanium layers. The maximum fluid flow velocity reported was about 500$\mu m/s$ measured at 10μm from the inner edge of the electrode. This velocity was measured at 5V, for an applied frequency below 500Hz and electrolyte conductivity was 2.1 x 10^{-3}S/m.

Symmetrical pair of electrodes structure may generate fast fluid flow, but it can only generate a local fluid flow on top of the electrodes. The resulted net fluid flow on top of these electrodes in one direction is zero. This results from the rotation of each roll in opposite direction of the role on top the opposite electrode, therefore each roll cancel the the effect of the roll in opposite electrodes (see Figure 3.3) [50].

One possible solution to generate a net fluid flow of electrolyte induced by symmetrical microelectrodes is to use AC-electroosmosis traveling-wave mechanism (see Figure 3.8). This mechanism is similar to electrohydrodynamic traveling-wave, which was discussed previously. The only difference is that the traveling-wave electroosmosis pumping is generated because of the influence of the electrical forces on the induced charge in the diffuse double layer, while EHD pumping occurs because of electrical forces on induced charges that appear in the electrolyte due to gradients of conductivity and permittivity [131]. The AC-electroosmosis traveling wave micropump was adopted by many research groups, where it was first introduced by Ramos et al. [100] and characterised by Garcia-Sanchez et al. [42, 43, 44] where the maximum fluid flow velocity achieved for an applied signal of 7V$_{pp}$ was 200$\mu m/s$ at 1 kHz [44]. However the traveling-wave micropumps suffer

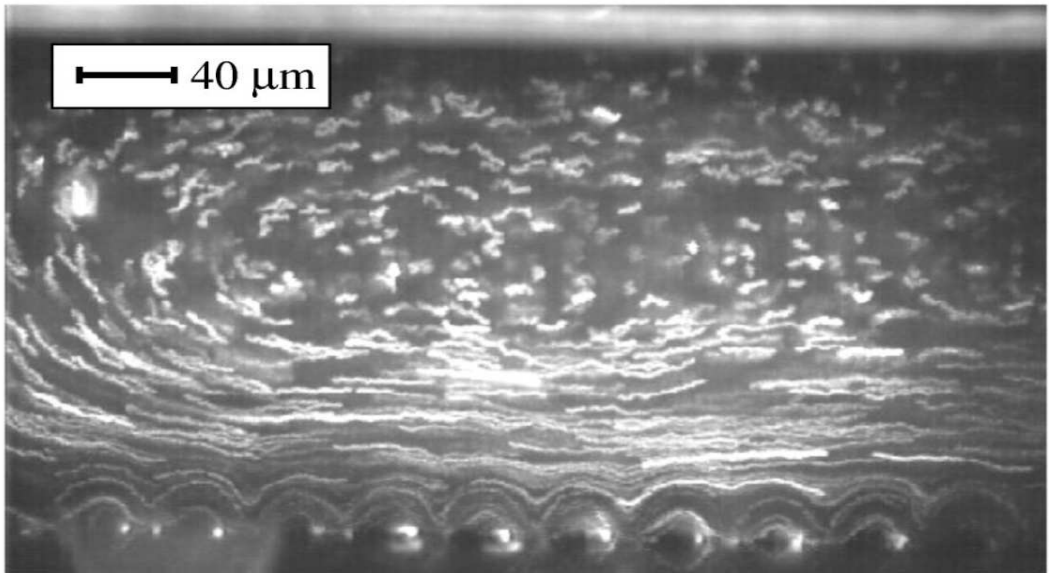

FIGURE 3.8: Experimental observation of fluid motion using 20 symmetrical planar electrodes. The electrodes were 2mm wide separated by 2mm gaps, and the applied voltage on consecutive electrodes was phase shifted by 90^o [100].

from wiring complexity, as each electrode requires a single electrical connection to the external source, which make these kind of pumps difficult to be scaled and integrated in a microchip.

3.4.2 AC-Electroosmosis micropump using asymmetric electrodes

One possible solution to generate a net AC-electroosmosis fluid flow over a set of micro-electrodes and to overcome the electrical wiring complexity, is to modify the geometry of the symmetric electrodes. Many designs were suggested and studied theoretically [96, 1, 2, 8, 109, 90] and experimentally [18, 111, 5] which are based on braking the symmetry of the electrodes.

First was Ajdari who proposed two models [1]; either by coating the electrode surface by a dielectric and changing their capacitance (Figure 3.9(a)), or by varying the surface hight of electrodes with half the spatial period of the array (Figure 3.9(b)), and hence, each side of a single electrode drives stronger AC-electroosmotic flow compared to the other side and therefore a net pumping can be generated over a long range array. Alternative approach was implemented by Brown et al. [18], and explained by Ramos et al.

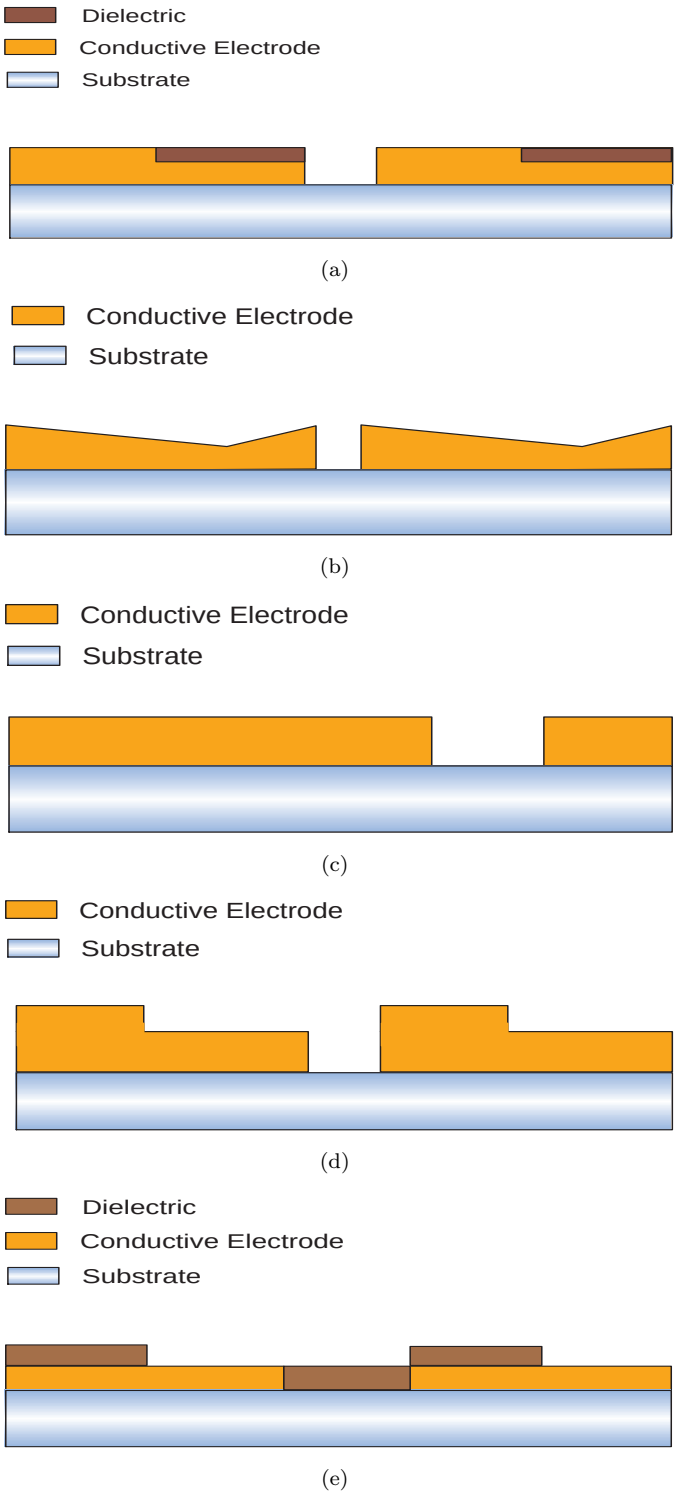

FIGURE 3.9: Schematic diagram of different AC-electroosmosis micropumps using asymmetric microelectrodes configurations. (a)- Planar electrodes covered by dielectric, (b)- Variation in surface height, (c)- Large and small electrodes configuration, (d)- Stepped electrodes configuration, (e)-Asymmetric capacitance modulation.

[96], where the asymmetry between the electrodes the symmetry between the electrodes involved the use of different widths and gaps of planar microelectrodes (Figure 3.9(c)), this electrodes structure was able to generate a steady fluid flow velocity on top of a set of repetitive pair of asymmetric electrodes. Bazant et al. [8, 109], brake the symmetry of the electrodes using a special geometry (3D) of stepped electrodes instead of using planar configuration Figure 3.9(d). The idea behind this design is to create a so called fluid conveyor belt with electrodes each having steps of two different heights: On each electrode, the region of desired forward flow is raised up, while the region of reverse flow is blocked physically below by the high electrodes wall, as a consequence the pumping efficiency was increased. Similar to stepped electrodes design proposed by Bazant, instead of making the steps in metal, Kuo et al. [70] have used dielectric instead, this configuration allowed to vary the capacitance of the electrical double layer and therefore the optimal frequency of maximum velocity was shifted to high frequencies. The only advantage of this design is that the pumping at high frequencies reduces the electrolysis and minimize bubbles generation.

3.4.3 Comparison between different AC-Electroosmosis micropumps

	Author	Year	Type of configuration	Measurements were taken:	Maximum fluid Velocity (micron/s)	Type of the flow generated		
						Local flow (rolls)	forward	reverse
A	Ramos *et al.* [99]	1999	Planar symmetrical electrodes	at the electrodes surface	200	√		
B	Green *et al.* [50]	2000	Planar symmetrical electrodes	at the electrodes surface	600	√		
C	Brown *et al.* [18]	2001	Planar Asymmetric electrodes	50 micron above the electrodes	75		√	
D	Mpholo *et al.* [86]	2003	Planar Asymmetric electrodes	at the electrodes surface	450		√	
E	Debesset *et al.* [35]	2004	Planar Asymmetric electrodes	above the electrodes	50		√	
F	Studer *et al.* [111]	2004	Planar Asymmetric electrodes	Outside the electrodes array	500			√
G	Gracia.*et al.* [44]	2006	Planar symmetrical traveling wave	140 micron above the electrodes	200		√	
H	Urbanski *et al.* [117]	2006	Stepped electrodes	away from the electrodes	420		√	
I	Tanguy *et al.* [115]	2008	Planar Asymmetric circular electrodes	Above the electrodes	70	√		
J	Moore *et al.* [83]	2008	Traveling-wave with Square spiral electrodes	Above the electrodes	333		√	
K	Kuo *et al.* [70]	2009	Asymmetric capacitance modulation	Above the electrodes	290		√	
L	Yang *et al.* [132]	2009	Planar symmetrical traveling wave	30 micron above the electrodes	100			√

TABLE 3.1: Comparison between different AC-electroosomsis micropumps configuration for last decade in chronological order. For the fluid flow velocities are given, were measured either on top of the electrodes or far away from the electrodes region. The fluid flow might be a local fluid generation or direct motion includes forward and reverse motions

Table 3.1 illustrates the maximum fluid flow velocity measured experimentally for the state of the art AC-electroosmosis micropumps fabricated since last decade. These micropumps are classified chronologically according to:

- Type of configuration: is addressed to the configuration of the electrodes which are presented previously in section 3.4.2. Mostly used structures are symmetric planar electrodes micropumps ("A, B"), asymmetric planar electrodes micropumps ("C, D, E, F, I"), traveling wave ("G, J, L"), stepped electrodes ("H"), and Asymmetric capacitance modulation ("K").

- The point where the measurements were taking. It can be on the electrodes surface, above the electrodes or far away from the electrodes. This can make a huge difference in the fluid flow velocity measurement. Mainly because the fluid flow velocity varies with the height of the channel, as it can be seen in micropumps "A, B, D" the fluid flow velocity measured at the surface of the electrodes is high. Taking the measurements above the electrodes like in the case "C, G, L", the velocity decreases, because AC-electroosmosis is a surface driven effect, the velocity is high at the electrodes surface and reduces as the distance from the electrodes increases. Moreover, the tracking beads near to the electrodes can be affected by the electric field upon the measurements, therefore for reliable measurements the fluid flow velocity has to be measured away from the influence of the electric field such as in the cases "F" and "H".

- Types of the flow generated can be fall in two categories a local, and net fluid flow. The local flow is where the fluid moves just in local area usually it rolls around the electrodes and does not move away from them. The net fluid flow is where the fluid moves away from the electrodes area, with a capability to move forward or reverse.

Based on Table 3.1, the fastest fluid flow velocity reported ($600\mu m/s$) was generated by planar symmetric electrodes made by Green et al. [50] (case "B"), however this micropump can only generate a local fluid flow. Studer et al. [111] configuration ("F")

has shown also a high net fluid flow velocity about $500\mu m/s$ using asymmetric planar electrodes. Mpholo et al. [86] using also asymmetric planar electrodes configuration ("D") $450\mu m/s$ flow velocity was achieved. Urbanski et al. [117] has also demonstrated that the use of asymmetric stepped electrodes can generate a net fluid flow velocity as fast as $420\mu m/s$. Traveling wave micropumps, despite they can produce a steady fluid flow velocity across a long fluidic channel but the highest velocity reported was just $333\mu m/s$ ("J"), which is lower in comparison to asymmetric planar electrodes and stepped electrodes configuration.

These comparisons remain approximative as these micropumps have different electrodes and gaps dimensions, different channel widths and height. Also they operate under different applied potentials and frequencies, and they use different medium conductivities. However all the electrodes in the micropumps were made out of metals, and metals undergo chemical reactions in the presence of the electric field. This is considered as a vital problem since the electrodes are the active part in the AC-electroosmosis micropumps as they dissolve in the electrolyte and limit the life time of the micropump. Studer's micropump although it generates the fastest net fluid flow velocity, it can only operate for 30 minutes before the electrodes dissolve in the electrolyte due to electrolysis.

Also most in these micropumps slip velocity on the channel walls is zero, the only existing slip velocity is present only on the bottom of the channel. As a consequence, the flow moves on the bottom and as the height of the channel increases the flow decreases which weaken the pumping back-pressure. According to Ramos et al. [58] in many situations, the flow rate Q that a pump is able to generate against a back pressure Δp under constant operating conditions, can be approximated by the following linear relation:

$$Q = Q_{max}(1 - \frac{\Delta p}{\Delta p_{max}}) \tag{3.20}$$

Where the maximum flow rate (Δp_{max}) can be obtained when the pump works without an external load, that is, when the pressure difference between the inlet and outlet of the pump is zero. For a rectangular cross section channel (height h and width w,

w>>h), and axial dimension L [58]:

$$Q_{max} = \frac{C_s}{C_s + C_d} \frac{\epsilon n V_o^2}{4\eta} wh \tag{3.21}$$

where: C_s: is stern layer capacitance, C_d: is compact layer capacitance, ϵ: is the medium permittivity, n is the number of waves in case of traveling-waves pump, V_o: is the applied potential, η: is the fluid viscosity, w and h: are the width and the height of the channel respectively.

The maximum flow rate (ΔQ_{max}): The maximum pressure is defined as the pressure difference required to stop the flow that the pump generates and is giving by [58].

$$\Delta p_{max} = \frac{C_s}{C_s + C_d} \frac{3\epsilon n V_o^2 L}{h^2} \tag{3.22}$$

where: C_s: is stern layer capacitance, C_d: is compact layer capacitance, ϵ: is the medium permittivity, n is a number of waves in case of traveling-waves pump, V_o: is the applied potential, L: is the axial dimension, and h: is the height of the channel.

Chapter 4

A novel 3D AC-electroosmosis micropump

A set of parallel symmetrical electrodes can only generate a local AC-electroosmosis fluid flow around the electrodes (as seen in section 3.3.1). Expanding the set of symmetrical parallel electrodes to a long array, can also generate a local fluid flow on top of each pair of electrodes. The resulted net fluid flow on top of these electrodes in one direction is zero, unless either the phase shift signal is applied to each electrode or the symmetry between the electrodes is broken. Many designs were suggested by different research groups and discussed in chapter 3. The AC-electroosmosis micropump with asymmetric planar electrodes [18, 97, 111] was amongst the successful AC-electroosmosis micropumps since it was able to generate fast fluid flow velocities, also it can move the fluid in forward and reverse directions inside the microchannel, and more interestingly that only a single layer of deposited metal is required to make the electrodes. These criteria make the asymmetric planar electrodes based micropump more attractive to be adopted for lab-on-a-chip applications. In this chapter asymmetric planar electrodes based micropump is studied in detail. The evolution from 2D to 3D asymmetric electrodes based

AC-electroosmosis micropump is also presented along with the suggested fabrication design.

4.1 2D AC-electroosmosis micropump using asymmetric planar electrodes

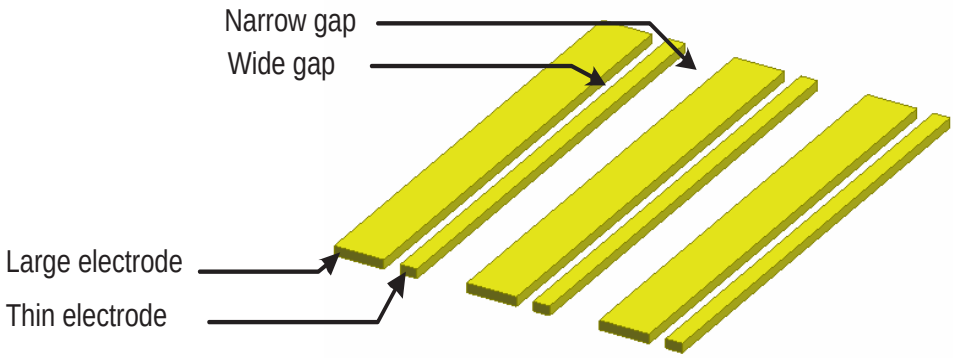

FIGURE 4.1: 2D-Asymmetrical planar electrodes, consist of a large end narrow electrodes separated by large and narrow gapes in periodical manner.

An electrolyte on an asymmetric planar microelectrodes array (Figure 4.1) powered by an AC signal in the order of hundreds to kHz range and at low voltages (less than 10 V_{pp}), can generate a unidirectional fluid flow. The unidirectional fluid flow resulting from spatially asymmetric applied potentials [96]. The physical mechanism responsible for the flow is AC-electroosmosis effect, where a nonzero time-averaged electroosmotic slip velocity at the surface of the electrodes can be produced. This is due to the influence of the nonuniform electric field that is generated between the asymmetric planar electrodes on the electrical double layer. The mechanism responsible for driving the flow is shown in Figure 4.2.

If an AC potential difference is applied to each pair of asymmetric electrodes generating a nonuniform electric field. At a given time t, the electric field distribution and fluid flow streamlines are represented by Figure 4.2.

The component of the field normal to the electrode induces a charge in the diffuse double layer; where the tangential component of the field produces a force on the induced

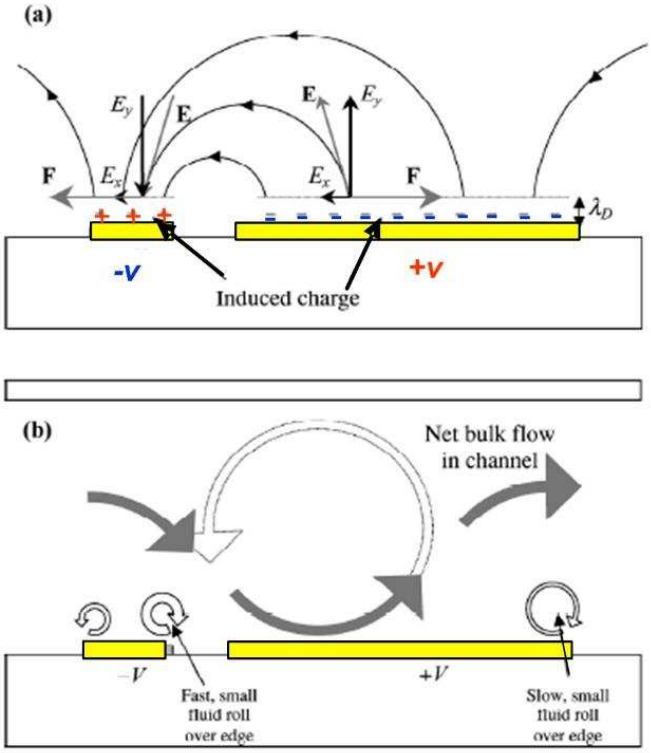

FIGURE 4.2: Schematic diagram of the physical mechanism of AC-electroosmosis in an asymmetric electrode array inside a microfluidic channel. (a): A diagram showing the charge induced in response to applied potentials on the electrodes, the resulting electric field in the electrolyte, and the force on the induced charge. (b): A diagram of the resulting bulk flow, with small rolls over the edges of the electrodes and a large roll over the inner edge of the larger electrode that rolls over the others to produce a unidirectional flow. [96].

charge [96]. The force has a nonzero time average because if the polarity of the field reverses, the sign of the charge changes also. This electrical force (Columb) generates the electroosmotic slip velocity.

Figure 4.2b, shows a schematic diagram of the fluid flow that occurs on top of the electrodes in the experiment [18, 96], the periodic arrangement of planar asymmetric electrodes produces a nonsymmetric local flow on top of each pair of electrodes, which eventually generates a global flow in the direction of broken symmetry along the channel. A rolling motion of the fluid is also generated at every electrode edge Figure 4.2b. According to Ramos et al. [96], that the formation and charging of the double layer is more uniform along the small electrode than along the large electrode, since it is distributed over a smaller surface. This results in two rolls over the small electrode, which

are similar in size, moving in opposite direction, and, therefore, do not contribute to the overall fluid flow [96]. Whereas, the rolls over the big electrode are more asymmetric, with the higher velocity occurring at the edge closest to the small electrode, where the electric field is stronger.

This roll would be limited by the height of the fluidic channel and follow the path shown by the gray arrow if the fluidic channel is closed at the left and right sides. However, since the channel is open and the other rolls do not extend upwards to any great height, the fluid instead moves outwards from the inner edge of the large electrode, then up and over the outer edge and the small electrode, and then down toward the next large electrode as shown schematically. This results in a directional flow along the electrode array [96].

4.2 Evolution from 2D electrodes to 3D

AC-electroosmosis is a surface driven effect resulting from the interaction between the electrical double layer induced by an electrical potential to electrodes and the electric field generated by the same potential. In order to to improve the pumping inside the fluidic channel, the internal resistance of the pump should be increased as well as increasing the surface area of the electrodes. This can be done for example by increasing the the length of the array. However, the resistance linearly depends on the length and therefore large increases in array length, with associated problems of transmitting the signal into long arrays.

Alternatively, significant improvement in resistance can be achieved by reducing the channel cross-section since the hydrodynamic resistance of a pipe proportional to the radius to power 4. Multiple channel in parallel therefore, have a significantly higher resistance that a single channel of the same cross-section; an effect well known in DC electroosmosis, where parallel channels and frits are used [73].

The proposed new design is based on the existing asymmetric electrode array but incorporating High Aspect Ratio pillar electrodes vertically dividing the channel and

extending the asymmetric structure upwards . More driving surface is produced for the same volume and the internal resistance is increased leading to greater pumping flow velocities and pressure. Based on these criteria, the new proposed design is based on using high-aspect-ratio (HAR) asymmetric pillar electrodes on top of planar electrodes inside a microfluidic channel as it can be seen in Figure 4.3.

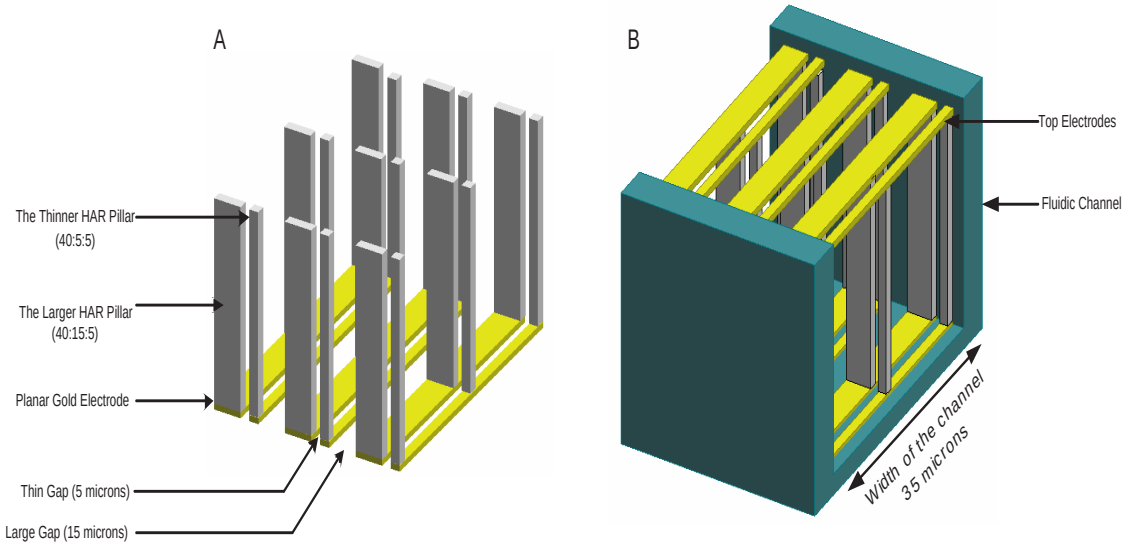

FIGURE 4.3: The new electrodes configuration shows an increase of the electrodes surface area from planar (yellow bottom electrodes) to 3D electrodes (high-aspect-ratio gray electrodes), but the channel volume remains the same . A. The new electrodes configuration of the electrodes without the channel. B. The new electrodes configuration with the upper electrodes inside the channel.

Increasing the surface area of the electrodes increases the power coupled into the fluid movement. By taking the channel volume and filling it with conductive pillars (see Figure 4.3), the surface area therefore increases, but the volume remains the same, increasing the drive per unit volume. Thus, the internal resistance of the pump can rise, reducing the maximum flow rate. However, it is expected that the increase in driving surface area will offset this to a degree. In order to prove and validate the functionality of the novel design of the 3D AC-electroosmosis configuration, a full device has to be fabricated first and then characterised.

4.3 Layout of 3D AC-electroosmosis micropump

The 3D AC-electroosmosis micropump mainly consists of the electrodes and a fluidic channel. Both electrodes and channel are designed to be fabricated on the top of 2x2cm^2 substrate in order to handle it and test it comfortably.

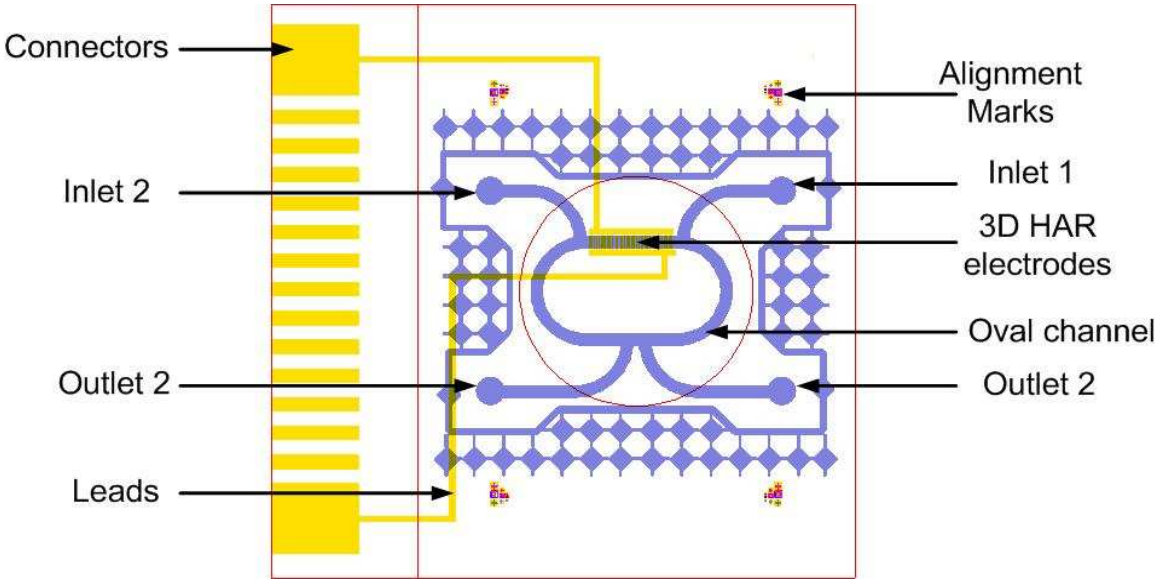

FIGURE 4.4: Schematic of the new AC-electroosmosis micropump. It consists mainly of: a microfluidic channel which is connected to the external via two inlets and two outlets, an array of planar and 3D high-aspect-ratio (HAR) asymmetric electrodes which are also connected to the external through large connectors, and 4 alignment-marks on each corner of the device to allow an accurate alignment during the lithography process.

The Fluidic channel has an oval shape (loop), as is shown in Figure 4.4. The advantage of using oval shape is to allow the visualization of the fluid flow for a longer distance under the microscope in comparison to linear channel. The long radius of the channel is $3mm$ and the shorter one is $1mm$. The width of the channel is $500\mu m$, where its thickness is $50\mu m$. Two inlets and two outlets, which are connected to the main channel. These in/outlets, are the fluid inputs and outputs, that allow to inject liquids and beads inside and outside the device. Also in order to remove of the wast outside the device.

In addition to this components, a top cover slip glass (The top lid) will be bonded on top of the channel in order to prevent any evaporation or fluidic leakage.

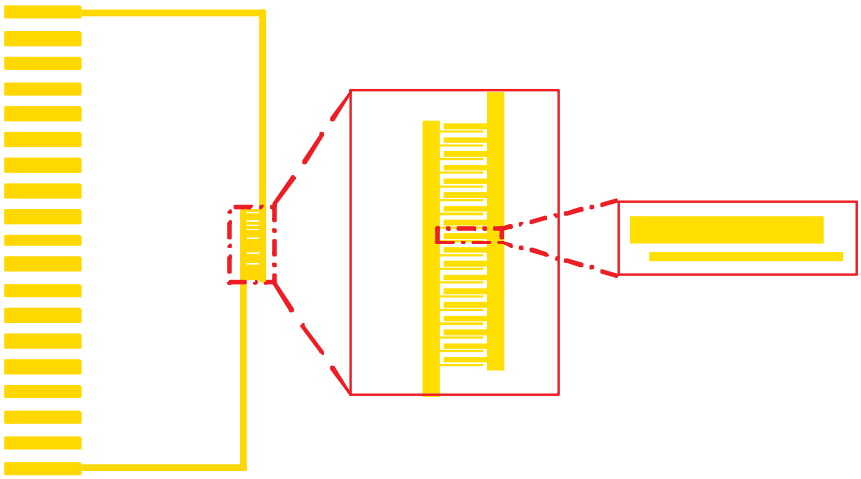

FIGURE 4.5: An electrodes array which consists of repetitive pairs of planar asymmetric electrodes (large and small electrodes). The entire array is connected to an external source via large pads

The electrodes are the active part of the micropump, and are designed to be implemented only on one side of the oval channel (see Figure 4.4). Therefore the fluid flow velocity will be measured on the opposite side of the channel to avoid the influence of the electric field on the tracing particles. The electrodes inside the channel are wired to relatively large external pads to allow the connection to the outside electric source.

Thin electrode	Thin gap	Large electrode	Large gap
$10\mu m$	$10\mu m$	$30\mu m$	$30\mu m$
$10\mu m$	$10\mu m$	$50\mu m$	$50\mu m$
$20\mu m$	$20\mu m$	$60\mu m$	$60\mu m$
$20\mu m$	$20\mu m$	$100\mu m$	$100\mu m$

TABLE 4.1: Different sizes of planar electrodes that are proposed for fabrication. 3 and 5 times asymmetry coefficients are used for $10\mu m$ and $20\mu m$ electrodes widths and gaps

Since our target is to make the smallest and fastest fluidic micropump possible, and since the active core of the AC-electroosmosis micropump is the electrodes, therefore, the minimum dimensions of the small electrodes/gaps were scaled down to 10 μm as it can be seen in Table 4.1. This limitation was due to lithography capability since a high-aspect ratio gaps below $10\mu m$ are not easy to achieve. To have an idea on the asymmetry effect of the ratio between the large electrodes/gaps and the small electrodes/gaps on the AC-electroosmosis pumping, the large electrodes/gaps were designed to be 3 and 5

times larger than the small electrodes. Also in terms of the area of the electrodes effect on AC-electroosmosis, the electrodes width was doubled on both cases (in the 3 and 5 times configurations). Table 4.1 shows the 4 proposed aforementioned electrodes/gaps configurations, which will be designed on a single 5 inch mask to make 12 devices in total (3 devices from each configuration (see Figure 4.8)).

For the 3D electrodes by using planar electrodes as the fundamental platform and taking the channel volume and filling it with conductive pillars, the new configuration of asymmetric electrodes which combines planar and high aspect ratio pillars is shown in Figure 4.3.

4.4 Fabrication flow

In order to make the new ACEO micropump, microelectronics fabrication processes can be used for the fabrication and miniaturization of the new micropump. The fabrication process flow is presented by Figure 4.6 and Figure 4.7.

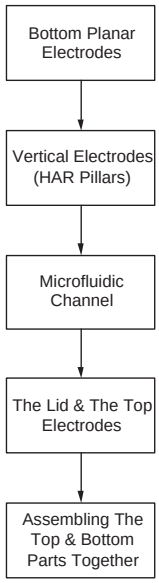

FIGURE 4.6: Fabrication process priorities chart. The planar electrodes have to be patterned first, followed by the high-aspect-ratio (HAR) electrodes to be fabricated on top of the planar ones, than the microfluidic channel to be patterned around the electrodes active area, and finally the top lid has to be assembled with the rest of the device

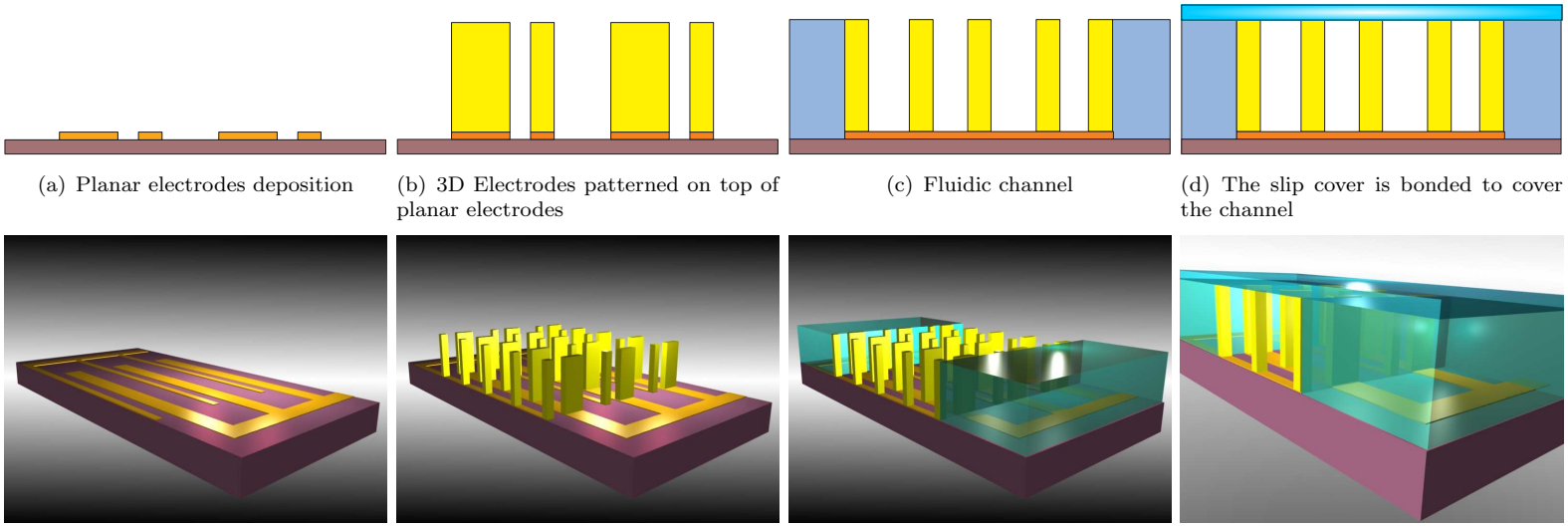

(a) Planar electrodes deposition

(b) 3D Electrodes patterned on top of planar electrodes

(c) Fluidic channel

(d) The slip cover is bonded to cover the channel

(e) 3D representation of planar electrodes

(f) 3D representation of the 3D HAR electrodes

(g) 3D representation of the fluidic channel after patterning

(h) 3D representation of Channel lid after bonding

FIGURE 4.7: A schematic shows the the evaluation from planar electrodes to the new 3D electrodes configuration.The 3D view representation is shown on the top part, and the cross section view is shown in the bottom . Figures (a,e) consist of asymmetric planar electrodes patterned on top of silicon wafer. (b,f) 3D high-aspect-ratio (HAR) electrodes are built on the top of the planar electrodes, (c,g) The electrodes are encapsulating with fluidic channel, (d,h) the device is sealed with a transparent lid

4.5 Masks designs and alignment marks

Since 4in wafers are used in the fabrication, the dimensions of the mask have to be 5in x 5in in order to cover all the wafer's surface. Masks were designed using L-edit CAD tool from Tanner. High quality chromium masks were used in order to eliminate any UV penetration to non desirable area. The resolution of the mask was chosen to be 0.25 μm, since the smallest features are $10\mu m$, and also to reduce the edge roughness. In order to make use of the space of the mask, 12 devices with 2x2 cm^2 per mask were designed. Since, the device is composed of 5 layers including the silicon wafer and the top cover slip layer, 3 masks were designed, therefore, the alignment marks, have been incorporated in each single design.

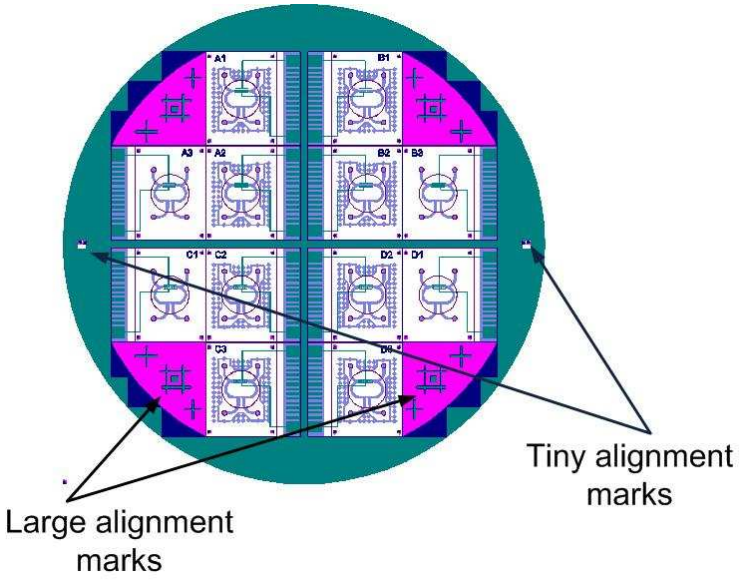

FIGURE 4.8: Complete set of designs and masks of 4in wafer which contains 12 devices, each device measure 2x2 cm^2. It shows the main locations of the large and small alignment marks on the wafer.

- *Alignment marks:* The alignment marks, are images selectively placed within and outside the array of devices for testing and aligning different layers of the device on top of each other during the fabrication. The alignment marks locations are shown by Figure 4.8.

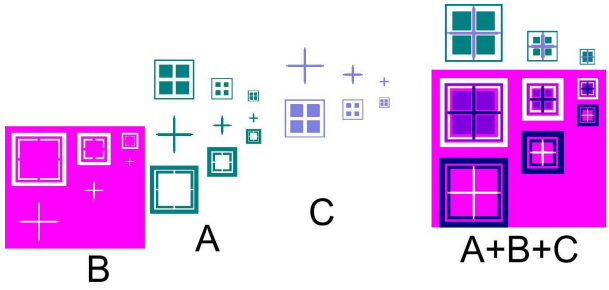

FIGURE 4.9: Alignment marks for three layers, the minimum dimensions of the alignment marks correspond to the minimum dimension in the device ($10\mu m$).

- *Types and locations of the alignment marks:* The alignment marks set for the 3 layers, is shown by Figure 4.9. Usually the cross shape is suited to draw the alignment marks as it helps to align in horizontal and vertical directions. Two types of alignment marks was drawn; large alignment marks in the 4 corners of the mask to help for visual and rough alignment, and small alignment marks along the X axis in the middle of the wafer. The use of the alignment marks on the X axis rather than Y axis, is due to some limitations with the use of MA6 Karl Suss mask aligner. For good precision, the smallest features and gaps of the alignment marks were designed to have the same size of the smallest features in the design which is $10\mu m$.

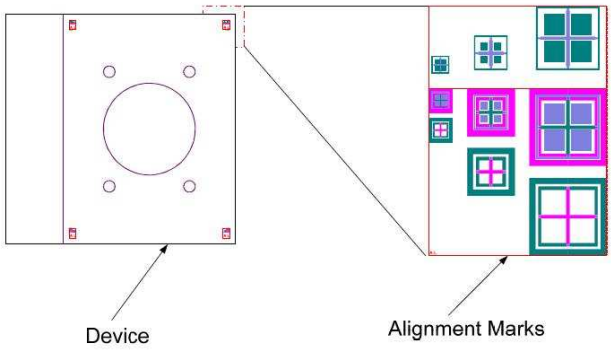

FIGURE 4.10: Shows the locations of the small alignment marks in each devices. 3 different alignments marks were designed for each layer.

As it can be seen in Figure 4.9 the alignment marks for the layer A are aligned

with the alignment marks from the layers B and C. Also the alignment marks from the layer B can be aligned with alignment marks from layer C and vice versa.

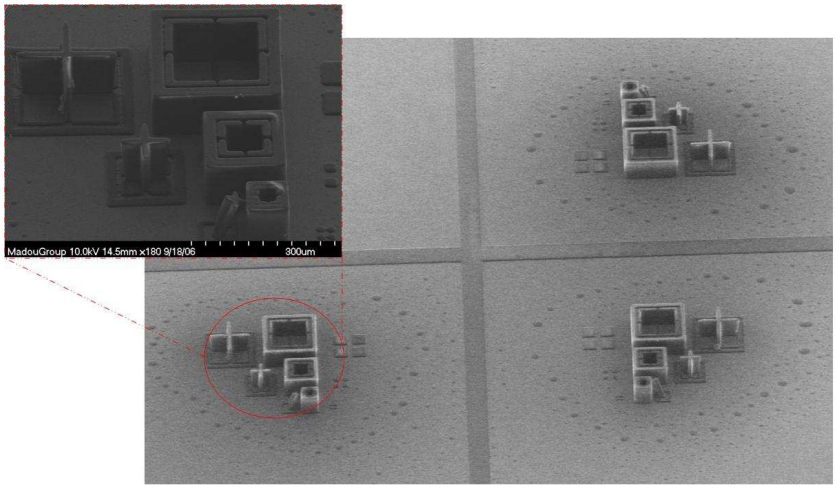

FIGURE 4.11: SEM pictures of SU-8 alignment marks for planar electrodes and HAR electrodes layers

Since each wafer contains 4 different designs, therefore, it is necessary to put also alignment marks in each separate device, thus will help to align each device separately after dicing. The alignment marks were put in the four corners of the device (see Figure 4.10) in order to simplify the alignment process during the fabrication. Fabricated high aspect ratio alignment marks of layers A and B are shown by Figure 4.11.

Chapter 5

Materials and Methods

Silicon-based fabrication techniques are widely used in microfluidic applications. However, many problems rise during the fabrication such as etching a channel on silicon wafer, which is both time consuming and expensive process. Or sealing the grooves with glass or Pyrex lids, using anodic bonding, which requires a strong electric field and high temperature. These critical conditions may deteriorate small features and thin metal layers, which may affect the electrodes and the electrical leads [105]. To provide reliable microfluidic structures, polymers, such as photoresists, PMMA, PDMS, can be employed. Moreover as almost MEMS devices require electrical connections, and probably 3-D electrodes, metals and conductive polymers can be employed. In this chapter, the appropriate materials for the fabrication of the new AC-electroosmosis micropump are chosen, followed by fundamental microfabrication techniques accordingly to the use of each material.

5.1 Selection of microfabrication materials

The new ACEO micropump consists of the following parts:

- A substrate and the lid where glass or silicon wafers can be used.
- Planar and 3D electrodes can be made from or conductive polymers, metals, and Silicon.
- A channel that can be made out of a thick polymer.

In this section materials that are required for the fabrication of the ACEO micropump are selected and covered.

5.1.1 Substrate

Usually in microfluidic applications, transparent glass is suitable as it allows to visualize, track particles and fluids motion. However, polymers such as SU-8 suffers from a weak adhesion to the glass. Moreover, in high temperatures processes like the pyrolysis process, where a temperature of more than 900^oC is required, in this case glass can not be used due to its low melting temperature which is around 500^oC. Quartz, can be used instead in this process, but it is expensive material and can be broken easily. Silicone dioxide wafers are suitable for this application, due to its high melting temperature, low price relatively to the quartz and silicone nitride, and also due to its availability in the market. The presence of the thin dioxide layer is important as it plays an important role to isolate the electrodes from the silicon substrate since silicon is conductive.

5.1.2 Polymers

Many polymers can be used in microfluidic applications, such as PMMA, PDMS, and SU-8. Despite SU-8 photoresist suffers from few disadvantages, mainly [31]:

- Weak adhesion to some substrates like glass and gold,

- Stress for large surfaces,
- Resist stripping after use as an intermediate material.

However, certain attributes make SU-8 suitable for building successful microfluidic structures using conventional microlithographic processes which are cited as following:

- A simplicity in fabrication, and flexibility in shaping,
- It is relatively inexpensive technology for high aspect ratio structure formation compared to other techniques, such as LIGA or dry etching techniques,
- Easy to spin a thick layer in one coating step,
- It enables the formation of deep trenches and extremely rigid structures by standard UV photolithographical means,
- It has an excellent sensitivity to UV,
- It has a very low absorption coefficient in UV range,
- It has a good optical properties,
- It has high resolution structures and nearly vertical sidewall surface,
- It characterizes with a good thermal and mechanical stability,
- Owing to its bio-compatibility and chemical resistance, as it is a compatible material for analysis by mass spectrometry,
- It may be easily treated to change its electrical and dielectrical properties.

Owing to these numerous utilities and advantages that characterize this amplified photoresist, therefore the implementations of the HAR electrodes would be possible using SU-8. Two possible fabrication processes can be adopted to make HAR electrodes. In the first approach, a conductive SU-8 can be used as permanent material for the electrodes. In the second method, SU-8 can be used as an intermediate mould for making gold electrodes, and will be removed afterwards.

Since SU-8 will be extensively used in the fabrication of the device , therefore fundamental techniques of preparing SU-8 and the use of this amplified photoresist are introduced also in this chapter.

5.1.3 SU-8 Photoresist

SU-8 is a negative near-UV amplified photoresist, an octafunctional epoxy resin based, that has been originally developed and patented by IBM [107, 77, 56, 80]. Due to its low optical absorption in UV range. This photoresist can form very thick film, the range of available thicknesses, extending from few nanometers to approximately 2 millimeters in a single spinning coat.

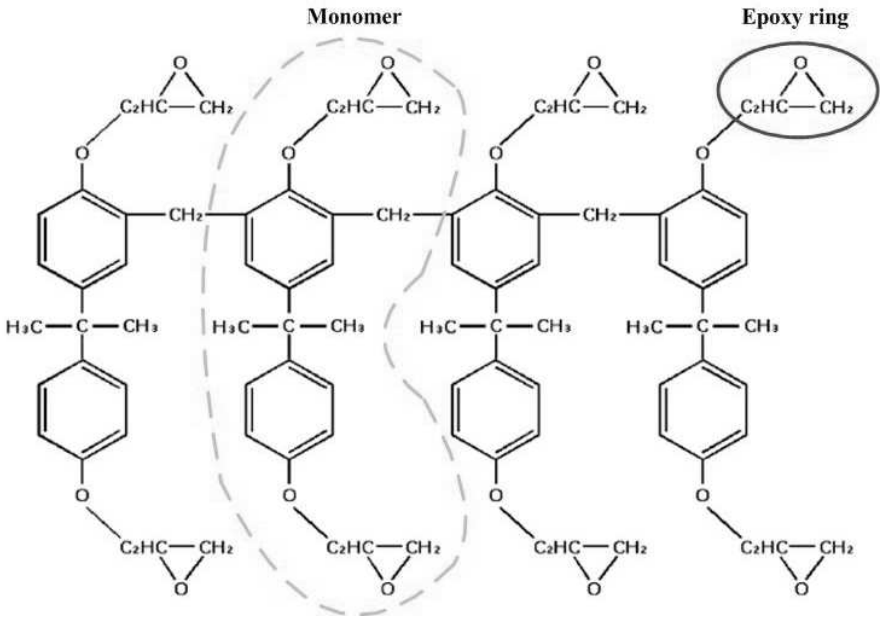

FIGURE 5.1: Molecular structure of SU-8 polymer, it consists of 8 epoxy groups. In SU-8 molecules the epoxy groups refer to the bridge linking between an oxygen atom and two carbon atoms. [67]

.

The main component of the resist is the octafunctional EPON SU-8 epoxy resin (glycidyl-ether-bisphenol-A novolac) from Shell Chemical. Figure 5.1 shows the molecular structure of SU-8 [72, 121] which has eight (08) epoxy groups. The bridge consisting

of the oxygen atom bonded to two carbon atoms forms the the epoxy ring. The SU-8 resist contains a few percent of photoacid generator that will produce a strong acid when a photochemical transformation takes place during the absorption of a photon. This photoacid acts as a catalyst in the subsequent crosslinking reaction that takes place during post exposure bake (PEB), the crosslinking occurs only in regions that contain acid catalyst.

The new series of SU-8 which are SU-8 2000 and SU-8 3000, they have minor changes in their chemical formulation. The SU-8 2000 series have an improved adhesion on most materials, due to the change of solvent to cyclopentanone rather than gamma butyrolactone (GBL). This solvent has a higher vapor pressure solvent which means that the nominal cure times are much reduced also. In addition they are compatible with conventional edge bead removal processes directly after spin coating. However the SU-8 3000 is an improved formulation of the SU-8 2000 where adhesion is also improved and the stress is reduced with this photoresist. The enhancement of the adhesion between both formulates of SU-8 2000 and SU-8 3000 with different substrates is presented in the Table 5.1:

Substrate	SU-8 2000 [MPa]	SU-8 3000 [MPa]
Si	53	71
SiN	43	73
GaAs	66	78
Ni	45	48
Au	29	47
Cu	38	80
Glass	Poor	23
Glass w/HDMS Prime	Poor	44
Quartz	61	80

TABLE 5.1: Comparison between the adhesion of SU-8 2000 and SU-8 3000 on different substrates [80]

5.1.3.1 Polymerization mechanism of SU-8

There are eight reactive epoxy functionalities allow a high degree of cross-linking after photoactivation, since it generates an acid during UV light irradiation with peaks of

absorption at 310 and 230 nm [121].

Epoxy resins could be cationically polymerised by utilizing a photoinitiator which generates strong acid upon exposure to ultraviolet light (365 to 436 nm) and the acid facilitates polymeric cross-linking during post-exposure bake.

This salt disintegrates upon UV exposure and generates an acid which initiates cross-linking of the polymer when heated. The non-cross-linked SU-8 can dissolve in Propylene Glycol Methyl Ether Acetate (PGMEA).

5.1.4 Conductive SU-8 photoresist

Many attempts have been used to change the conductivity of insulating polymers matrix. The basic idea behind these techniques was by adding some nano-particles to the polymer to form conductive paths. Different kinds of inorganic particles like carbon [106, 23] or metallic such as copper, iron, silver,and gold which have been used [81], in different shapes (microbeads, flakes, fibers, and wires), and in different sizes also (ranging from 1nm to 10nm). Many types of these conductive polymers were involved in MEMS fabrication. However, patterning these polymers, is difficult task, and requires many steps since the dry etch process is involved. To overcome these problems, a new idea was proposed by a group from EPFL, Switzerland. Their idea was making SU-8 silver composites polymer and exploring the optical characteristics of SU-8, since it is an amplified resist [65]. The SU-8 photoresist is filled with silver nano-particles, where the composition is homogeneously mixed. The selection of silver nano-particles as conductive filler, because their low absorption at the irradiation wavelength relatively to gold, aluminum and copper [64]. This electrically conducive polymer composite is known as silver nano-particles conductive SU-8 [63]. However, the silver nano-particles conductive SU-8 photoresist suffers from some problems also. Since the dimensions of silver particles are in the nanometer scale, therefore by adding the silver powder to the SU-8 photoresist, this changes the viscosity. Consequently, this photoresist cannot be spread on a wafer by spin-coating, alternatively a scrapper can be used instead of the spinner [63]. This makes it difficult to control the thicknesses of different layers of the proposed

design. Moreover, for thick films, silver nano-particles act like a mask, preventing the UV light to crosslink the deep parts of the photoresist (usually in the interface of SU-8/substrate) despite light scattering [64]. The resolution of this material varies from $5\mu m$ to $30\mu m$, which is unsuitable for fabrication of 10 and $20\mu m$ structure, therefore, for this reason and the previous cited reasons, the conductive SU-8 will not be chosen as the perfect material to fulfill the fabrication proposed.

5.1.5 Pyrolyzed SU-8 (Carbon-MEMS)

Carbon have a wide range of different crystalline structures and morphologies, which have enabled different physical, chemical, mechanical, thermal and electrical applications. Recently carboneous materials were used in microfabrication techniques to give a rise to a new technology called Carbon MEMS (C-MEMS). C-MEMS has received a lot of attention due to its involvement in many applications such as microelectrodes in electrochemical sensors and microbatteries. Many other methods are being used in the fabrication of Carbon structures such as the use of carbon ink. However, most of these fabrication techniques require expensive processes such as reactive ion etch (RIE) and focus ion beam (FIB) which are basically time consuming and also they have a low features resolution and poor repeatability. The new promising C-MEMS fabrication technique for high aspect ratio (HAR) structures and high densities patterns has been developed by Prof. Madou's group at the University of California Irvine, USA [126]. This new technique is based on the pyrolysis process in an inert environment of the photopatterned resist at different temperatures and different ambient atmospheres. Both photoresists (positive and negative) can be used in this type of process [125].

The physical and chemical properties of fully cross-linked SU-8 make it very efficient as an intermediate material but make it also attractive as a functional material for C-MEMS applications. Adopting pyrolysis process, the SU-8 can be used as functional material, this means that the pillars (HAR electrodes) can be made first from SU-8, and then converting them to conductive SU-8 while changing their electrical characteristics.

Pyrolyzed SU-8 might provide an interesting material for the electrodes and might be also a good solution to miniaturize 3D-conductive structures for the following reasons:

- High aspect ratio carbon posts (> 20:1) can be achieved by pyrolyzing SU-8 negative photoresist in a simple one step process.
- C-MEMS can be used for both the current collector and the electrodes applications.
- Photoresist derived carbon electrodes show excellent electrochemical kinetics.
- The pillars made by gold undergo chemical reactions involving dissolution and redeposition. In contrast, the pyrolyzed electrodes will be less conductive than the gold ones (see Table 5.2), but they are perfectly polarisable, which is ideal for AC-electroosmosis.

Therefore, SU-8 photoresist seems to be a good candidate for the fabrication of HAR electrodes that are designed for the 3D ACEO micropump.

5.1.6 Metals

Metals in general characterize with good electrical and thermal conductivity. In microfabrication mainly metals are employed for making connectors, and 3D electrodes structures. In ACEO micropumps the electrodes have to be in contact with electrolytes and liquids, therefore, the oxidized metals such as copper, aluminum will be avoided. Noble metals which have higher conductivity and less oxidization behavior like platinum and gold can are used in microfluidic devices, since they are relatively chemically resistive. In addition, few metals like chromium and titanium are used as seed layer on most fabrication posses which involve metals in order to increase the adhesion between the substrates and other metals or polymers. Table 5.2 shows the electrical resistivity and the melting point of the commonly used metals in microfabrication along with Carbon and Silicon [128].

Material	Electrical resistivity $[10^{-8}\Omega m]$	Melting Point $[^oC]$
Gold (Au)	2.2	1064.18
Copper (Cu)	1.7	1084.62
Nickel (Ni)	7	1455
Titanium (Ti)	40	3287
Carbon (C)	3500	3500
Silicon (Si)	100 000	1687

TABLE 5.2: Electrical resistivities and melting point temperatures of frequently used materials in microfabrication

5.1.7 Silicon

Planar and 3D electrodes can be also made from Silicon since it is conductive material. However due to the implementation of multiple layers of electrodes (3D-electrodes on top of planar electrodes) and due to the small dimensions (10 and 20 μm) and high aspect ratio (at least 5) for both 3D-electrodes and gaps, therefore bonding and reactive ion etching (RIE) processes will be used, which require more complicated fabrication protocols, heavy equipments and more processing time. As a consequence the silicon will not be used in this work.

5.2 Microfabrication techniques

Since polymers and metals are involved in the fabrication of the micropump, photolithography, metals depositions and etching processes are explained in the following section.

5.2.1 Substrate preparation

In order to ensure a good adhesion and good uniformity of the photoresist the substrate has to be cleaned before use. There are two types of cleaning RCA1 and RCA2.

RCA1: This type of cleaning is used to remove organic contaminations by adding one part of NH_3 and five parts of DI water. This combination needs to be boiled with addition of H_2O_2. At this time the wafer needs to be immersed for ten minutes.

RCA2: This type of cleaning is applied to remove metal ions by adding one part of

HCl to six parts of DI water after heating and boiling them. Afterward, the wafer needs to be immersed also for ten minutes. After these RCA cleaning processes, an oxide layer remains on the wafer; this layer is stripped off by dipping the wafer in 1% of HCl solution for a short time and then rinsed in water.

***D*ehydration bake:** This step is necessary specially after the wafer has been rinsed or immersed previously in water or either if the humidity is high. The water should be removed from the wafer by dehydration in order to provide a good adhesion of the resist. In most processes, the wafers are baked for 150^oC for about 1 hour.

5.2.2 Photolithography

Photolithography is the pattern transfer from a photomask to the bulk or thin film by selective exposure, employing a light source and light-sensitive material. The fabrication of the new ACEO micropump will rely on soft lithography employing UV light. A good lithography involves substrate preparation (cleaning, dehydration, priming), a sensitive resist, a good mask aligner with good optical system (uniform exposure), baking conditions (leveled hot plate, uniform temperature), and good developer condition. In this section the photolithography steps which will be used to pattern SU-8 layers are explained.

5.2.2.1 Spinning process

In order to coat the wafer with SU-8 photoresist, two stages will be applied. First spinning the wafer slowly to allow the resist to dispense on the wafer, usually the first spinning speed should be around 100 and 500 rpm. It depends on the resist viscosity. Then the wafer is spun at selective speed by ramping it gradually. The spin speed and acceleration determines the final thickness of SU-8 film. The thickness of the resist is defined by the spinning speed which is related to the viscosity, the concentration of the resist, and the weight of the molecules. The empirical expression of the thickness T is given by [78]:

$$T = \frac{KC^{\beta}\eta^{\gamma}}{\omega^{\alpha}} \tag{5.1}$$

K: Overall calibration constant, C: polymer concentration in g/ml solution and η: intrinsic viscosity. α,β, and γ: are constants

The recommended spinning speeds for different viscosities of SU-8 are shown by the graphs in Figure 5.2.

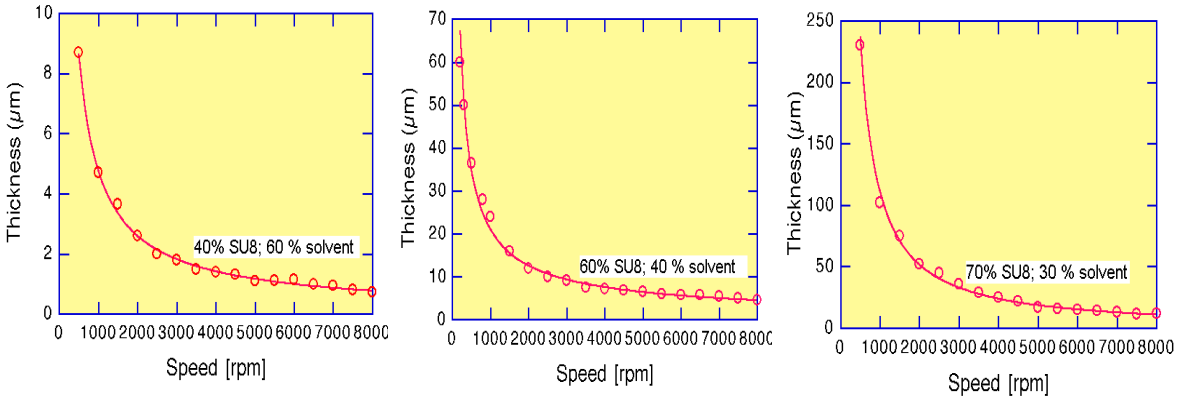

FIGURE 5.2: Spin speed for different SU-8 viscousities (containing 40%, 60%, and 70% of SU-8 reisine), the high viscouse composition gives a thicker film profile [56].

5.2.2.2 Soft bake

Spinning the resist on the wafer does not give the final required thickness of the coated layer, since it still contains about 15% of the solvent which may be a good factor for generating the stress . Softbaking the wafer on leveled hot plates from 1 to 10 min at $65^{o}C$ then at $90^{o}C$. The two steps baking are required in order to avoide the stress, to increase the adhesion and to remove the remain solvant. The hotplate is recommended as it helps to remove almost the solvent from the film, whereas the oven prevents the solvent to completelty evaporate resulting in a non-uniform film. The baking duration it strongly depends on the thickness and viscosity of SU-8 film, the recommended softbake time and temperatures for different SU-8 viscosities are presented in Table 5.3 [80]

Formulation	Thickness [μm]	Pre-bake [min] (at 65^0C)	Softbake [min] (at 95^0C)
SU-8 2	1.5	1	3
SU-8 5	7	2	5
SU-8 10	15	2	5
SU-8 25	25	3	7
SU-8 50	100	10	30
SU-8 100	250	30	90

TABLE 5.3: Pre-bake and softbake times recommended for different SU-8 formulations for different thicknesses

5.2.2.3 Exposure

The photoresist is usually composed of polymer, sensitizers and a casting solvent. The polymer changes structure when it is exposed to the radiation, the sensitizers control the photochemical reactions and the solvent is responsible for the spin application and the creation of thin layer on the wafer surface [78]. The incident light intensity (W/cm^2) multiplied by the exposure time (second) gives the incident energy (J/cm^2) or the dose D. The UV radiation induces a chemical reaction in the exposed areas of the resist which leads to break and polymerase the resist, the polymerization mechanism of SU-8 will be explained in section 5.1.3.1. The recommended exposure doses for different thicknesses of SU-8 are presented in Figure 5.3.

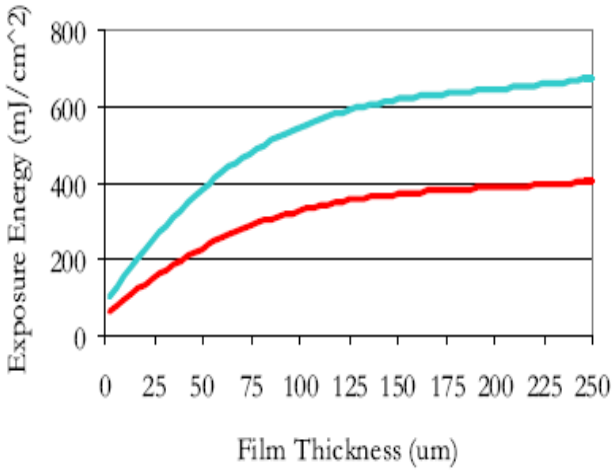

FIGURE 5.3: Recommended UV exposure dose for different thicknesses. The red (bottom) and blue (top) lines shows the minimum and the maximum exposure doses that can be applied [80].

5.2.2.4 Post exposure bake

The post exposure bake (PEB) is performed also on leveled hotplate on two stages, at 65^oC then ramping slowly to 95^oC. This baking is considered as the backbone step of the polymerization the SU-8 structure. During the PEB stage, the photoacid which was generated during the UV exposure step leads the SU-8 structure to crosslink. Also the remained solvent will be evaporated. The recommended baking time for different thicknesses of SU-8 are presented on the Table 5.4.

Formulation	Thickness [μm]	Pre-PEB time [min](65^oC)	PEB time [min] (95^oC)
SU-8 2	1.5	1	1
SU-8 5	7	1	1
SU-8 10	15	1	2
SU-8 25	25	1	3
SU-8 50	100	1	10
SU-8 100	250	1	20

TABLE 5.4: Post exposure bake time for different SU-8 thicknesses.

5.2.2.5 Development of the photoresist

Formulation	Thickness [μm]	Development [mn]
SU-8 2	1.5	1
SU-8 5	7	1
SU-8 10	15	3
SU-8 25	25	4
SU-8 50	100	10
SU-8 100	250	20

TABLE 5.5: Recommended development time for different SU-8 viscosities

The standard way to develop SU-8 photoresist, is to immerse the wafer in the developer followed by agitation at room temperature. For high-aspect-ratio structures, rinsing is recommended to remove the residues that may stuck between the structures. Other techniques such as spray development may also be used. The development time depends on the layer thickness, and baking time. The last step in the development is to rinse the substrate with Isopropanol which helps to remove any residue left. Air or nitrogen blow dry, can be also used to dry the structure from the solvents. The recommended developing time for different thicknesses of SU-8 is presented on Table 5.5.

5.2.2.6 Hard Bake

This optional baking step is run at high temperature (around 150^oC), for applications where the resist is to be left as part of the final device, both hot plates and oven can be used. This step is performed to further crosslink the material, to more solidify the structure and to increase the adhesion of the SU-8 layer on the substrate. Baking times depend on shape and thickness of the structure. In electroplating process this step is not recommended.

5.2.3 Pyrolization of SU-8 (C-MEMS)

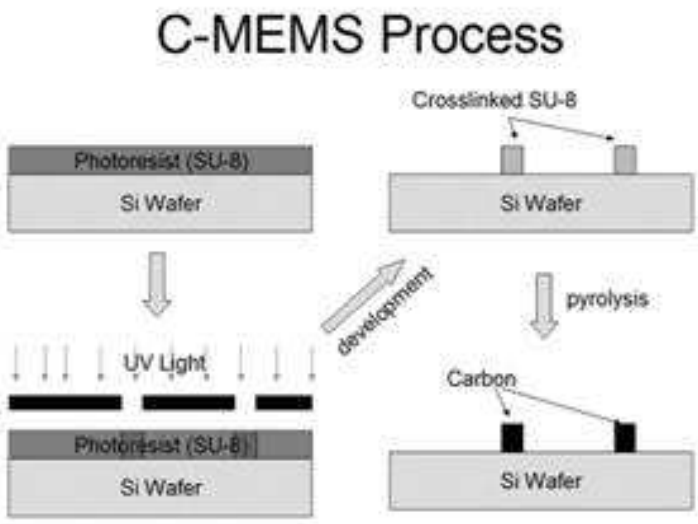

FIGURE 5.4: C-MEMS process flow. In the first step photlithography process is used to produce a polymer structure. In the second step, the photopatterned resists, heat treated (pyrolyzed) at high temperatures in different ambient gases to produce a conductive carbon structure [126].

This process involves baking polymers in particular SU-8 as we are using HAR structures, in an environment free of oxygen at 900^oC. The presence of the oxygen in the oven leads to burn the polymer structures, therefore %95 N_2 and %5 H_2 will replace the oxygen inside the oven, H_2 will absorb the O_2 gas released by the remained solvent inside the photoresist to form H_2O which subsequentley will evaporate. At this

temperature, the electrical characteristic of the polymer change from a dielectric to a conductive carbon. The process flow for pyolized step is shown in Figure 5.5.

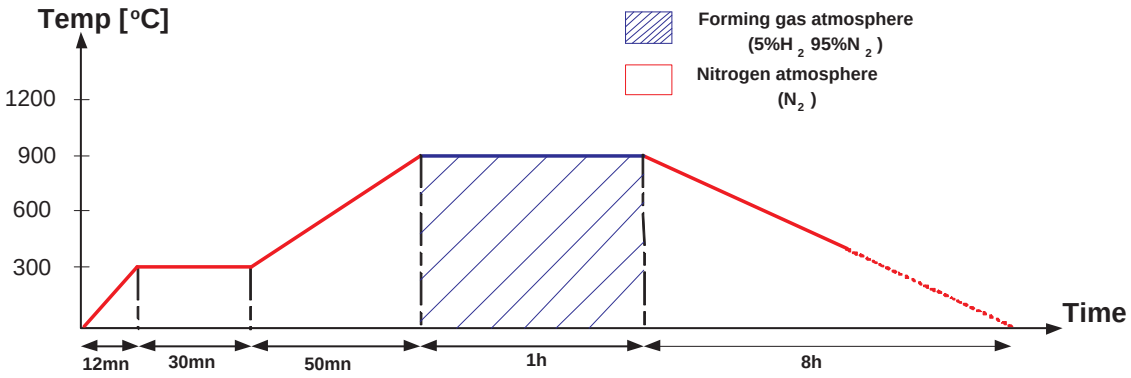

FIGURE 5.5: C-MEMS schematic process flow, indicating the temperatures and gases variation in each phase. At 900^oC 95% N_2, 5% H_2 gas is applied for 1 hour heat treatment in order to perform the pyrolization [92].

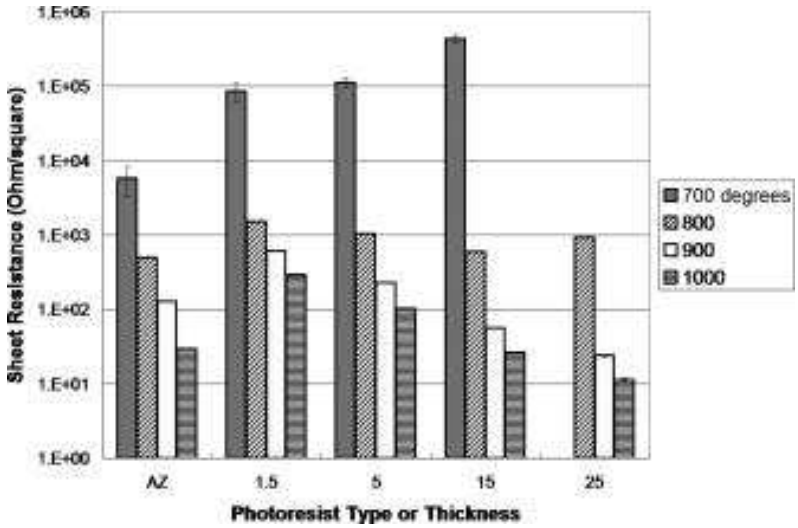

FIGURE 5.6: The resistivity of carbon films obtained from AZ P4620 photoresist and various-thickness SU-8 films after 1 h of heat-treatment at different temperatures [92].

Pyrolyzation temperature plays and important role in converting polymers to carbon, according to the experiments carried out by Park et al. [92], there is a large change in resistivity at the temperatures between 600^oC and 900^oC as it can be seen in Figure 5.6, the thicker layers of SU-8-derived carbon are more resistive at lower carbonization temperatures (700-800^oC), but they tend to be slightly more conductive than thinner layers

at higher temperatures ($900-1000^oC$). The resistivities of both photoresists, regardless of the thickness or resist tone, are almost identical after heat-treatment at 1000^oC (5.330 ∓ 0.574 x $10^{-5} \Omega m$).

5.2.4 Metal deposition

This process involves in the deposition of few nanometers of high purity conductive layers. Many technologies are being used to deposit thin films, mainly physical vapor deposition (PVD), which involves evaporation of desired metal using electron beam and condensation on the substrate to form a thin metal layer. Also chemical vapor deposition (CVD)which involves substrate heating to about 500^oC for metal deposition. However the use of these technologies remains limited to thin films (less than 1 μm) applications. For the fabrication of the 3D ACEO micropump, 40 μm electrodes thick are targeted, therefore the suitable technology for this application would be the chemical deposition.

5.2.5 Chemical deposition (Electroplating)

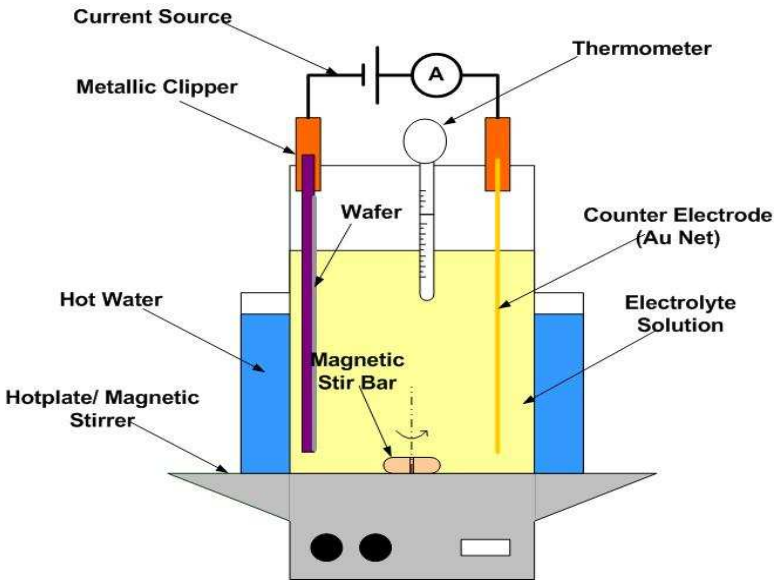

FIGURE 5.7: A schematic of a standard electroplating setup.

The electroplating or electrodeposition process is well suited to make thick films and structures of metals such as copper, nickel and gold through polymer mould. The films

can be made in any thickness from few microns to tens of microns. The deposition is controlled by the current density generated from an external source, by the medium temperature and the pH of the solution (see Figure 5.7). In oder to keep the electrolyte temperature constant, a second container full of water can be used in order to warm up all the the electrolyte, and to keep the temperature constant over all the container not only the bottom part. In addition to that, the magnetic stirrer hot plate is used to mix the electrolyte inside the container to get a uniform temperature of the solution. Electroplating process requires electrical contact to the substrate when immersed in the bath, therefore, the surface of the substrate must have an electrically conducting layer before starts the electrodeposition. For this reason the substrate has to be first evaporated by a conductive seed layer before use. Usually chromium and titanium are used as seed layers since they have good adhesion to most substrates.

Chapter 6

Preparation and testing of SU-8 photoresist

In order to fabricate the 3D-ACEO micropump different thicknesses of SU-8 structures are required, therefore different SU-8 viscosities and will be involved. This chapter shows the techniques followed to prepare home made SU-8. Photolithography tests will be carried out on the home made SU-8 in order to demonstrate its functionality.

6.1 Preparation of SU-8 photoresist

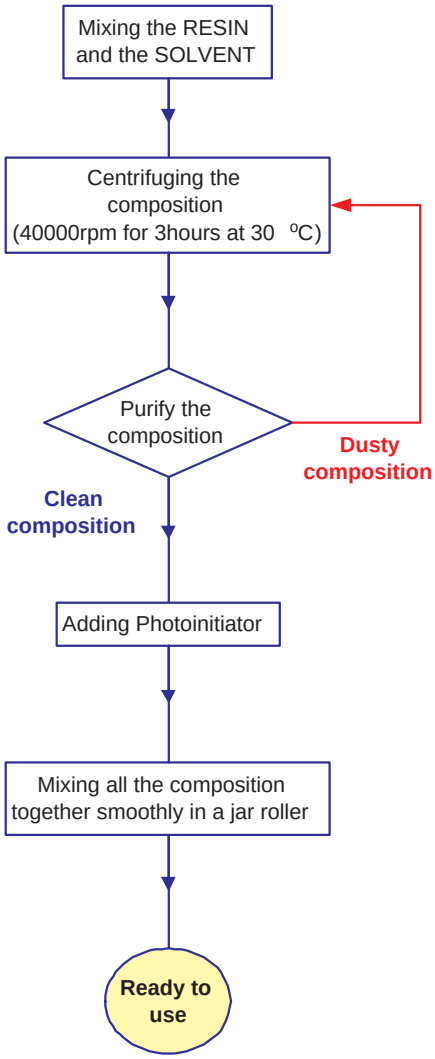

FIGURE 6.1: Flow chart shows the steps followed to prepare home-made SU-8 photoresist

SU-8 is chemically amplified near-UV negative photoresist. The SU-8 photoresist can be produced using commercially available materials. The main component of the photoresist is the octafunctional EPON SU-8 epoxy resin (glycidyl-ether-bisphenol-A novolac) from Shell Chemical. A photoinitiator is added to optimize the contrast of the photoresist upon UV exposure [116, 14, 20]. The photoinitiator is composed from mixed triarylsulfonium and hexafluoroantimonate salts in propylene carbonate solvent. Finally all the composition is dissolved in the organic solvent gamma-butyrolacton (GBL).

The amount of solvent determines the viscosity and thus, the range of available thicknesses, extending from few nanometers to approximately 2 millimeters. Along with GBL, cyclopentanone is also can be added to the solvent in order to make the SU-8 2000 formulation

Four(4) formulations of SU-8 were prepared: SU-8 5, SU-8 10, SU-8 25, and SU-8 50. In order to produce these photoresists (see Figure 6.1), first the solvent and the epoxy resin were mixed together. In order to get clean resist without any dust or lage particles, a filtration step was performed. At first instance a syringe with $0.2\mu m$ filter was used, however due to the high viscosity of the liquid, the filtration did not work. As an alternative the mixture was then centrifuged at 30^oC for 3 hours with a speed of 40000 rpm. Centrifuging step was used to separate the large particles of the resin and dust from the resist. However, this process may be replaced by a set of high pressure pump and ceramic filter with $0.2\mu m$. After the first centrifuge step is processed, the mixture is poured in a new container by separating the clean part of the mixture from the dusted. The centrifuge process was repeated again in the same conditions (30^oC for 3 hours with a speed of 40000 rpm), until a clear resist was reached. The last step, was by adding photosensitizer to the resist using $0.2\mu m$ filter, with the absence of UV light (this process was performed in the yellow room). Finally, the composition was mixed slowly in a jar roller at room temperature for a few hours. Rolling time, and the composition epoxy resin, solvent and photosensitizer quantities for different SU-8 formulations are shown in Table 6.1. Increasing the quantity of the resin makes the composition more viscous, and hence, requires more time to mix all the components together.

Resin	GBL	Photosensitizer	Rolling Time
35-75 %	22-60 %GBL	1-5 %	1-15 days

TABLE 6.1: Quantities of different ingredients and rolling time which were used to make and control the viscosity of home-made SU-8.

6.2 SU-8 photoresist tests

Many attempts of standard photolithography tests were applied on the home-made SU-8 to check its reliability and repeatability. In these tests, $40\mu m$ thick layers of SU-8 50 were spun to create a various range of patterns with different sizes and shapes on glass slides. The applied photolithography process is mentioned in chapter 5 using Karl Suss MA6 mask aligner. All the tests on home-made SU-8 were run in the ORC class 1000 cleanroom at the University of Southampton, UK.

6.2.1 Air bubbles

During the tests many problems have been raised, the first problem occurred upon pouring the resist on the substrate or just after spin coating process, where undesirable clusters of air bubbles appeared in the thick films of SU-8 as it is shown in Figure 6.2.

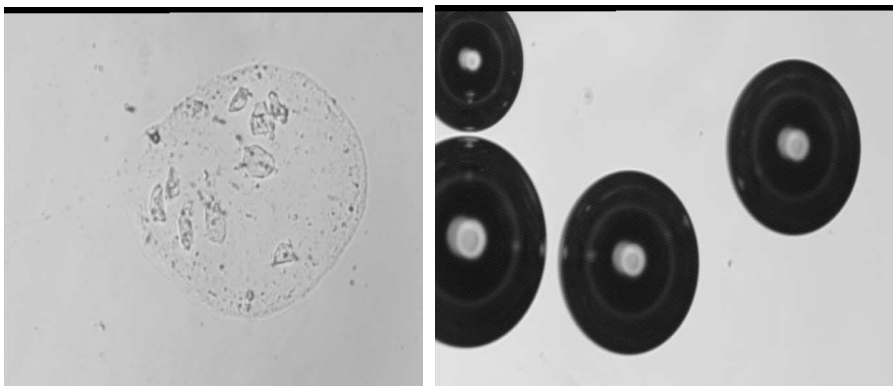

(a) Bits of dust are surrounded by air bubble (b) Air bubbles

FIGURE 6.2: Formation of the air bubbles on a glass slide. The bubbles can form due to the presence of external impurities like dust in the SU-8 photoresist. Also can be formed due to aggressive agitation of the SU-8 photoresist before spinning step.

The creation of bubbles on the substrate may be a result of the existing bubbles in the SU-8 bottle before dispense it, which will deposit onto the substrate. Bubbles cannot float out from thick photoresist in particular small bubbles, since thick SU-8 formulations have high viscosity which ranges between 1050 cSt and 51500 cSt for SU-8

10 and SU-8 100 respectively. In order to work out this problem SU-8 bottle kept in upward position and heated up in an oven at 60^oC for approximately 30min, this helped to decrease the viscosity of the resists and release the bubbles.

External impurities like dust can contaminate the photoresist, as consequence they generate bubbles in the SU-8 film after spin coating step. In this case the air bubbles surround these micro particles as it is shown in Figure 6.2(a). To remove these kind of bubbles the photoresist has to be filtered.

The use of a syringe or pipette to dispense a thick layer of SU-8 onto the substrate can also generate bubbles on the SU-8 film. To reduce this problem, it is recommended to pour SU-8 from the original bottle or from a small bottle with large orifice directly to the substrate, which will give more control to pour the right amount of SU-8 and minimize the creation of bubbles.

The technique of pouring SU-8 itself from the bottle can generate bubbles also. The appropriate technique is to get the SU-8 bottle as close as possible to the substrate and pouring SU-8 slowly.

Using above techniques may reduce the air bubbles to a large extent, but sometimes few bubbles may appear after pouring the photoresist. However, keeping the photoresist to relax on the substrate before spin coating it for 1 to 2 hours will give the air bubbles time to rise out of the solution.

A sharp needle can be also used to open the air bubbles before spinning, if the opening of air bubbles occurs after the spin coating step, a relaxation time will be recommended to allow the SU-8 to planarize and re-flow into the gaps generated by the bubbles.

6.2.2 Adhesion problem

After removing successfully the air bubbles from a 40 μm SU-8 film, the remained steps from the lithography process were performed. The temperatures of oven for applied softbake were 65^oC for 20 min and at 90^oC for 45min, the exposure dose was for 450 mJ, post exposure bake temperatures were 65^oC for 5min and at 95^oC for 20 min, then

the substrate was developed. However an adhesion problem and lifting off the SU-8 structures occurred during the development step as it is clearly shown in Figure 6.3.

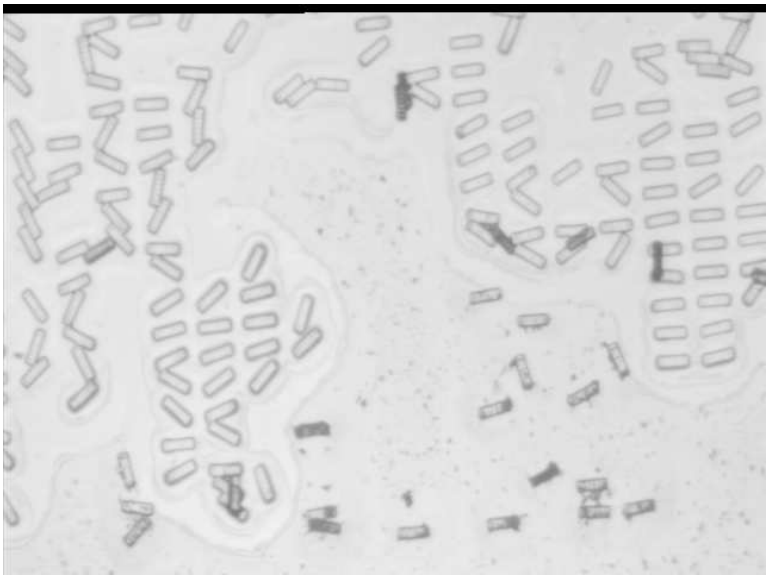

FIGURE 6.3: Poor adhesion can be seen during developing process of photopatterned SU-8 structures on glass

Adhesion of the SU-8 is usually good, but it strongly depends on the properties of substrate interfaces. In these experiments SU-8 suffers from a weak adhesion and unwanted debondings from the glass.

To improve the adhesion, a pretreatment of the substrate is recommended before the spin coating step, and also reducing the inter-facial stress during the process it has to be taken in consideration.

To ensure a good adhesion, and a good film uniformity on the substrate, therefore it is necessary that the substrate has to be cleaned. Many wet and dry methods are used in cleaning wafers from contamination, the most prevalent cleaning procedures are the aforementioned RCA1 and RCA2. Plasma cleaning can also promote the adhesion.

Adhesion promoter: In order to increase the adhesion of the SU-8 on glass or silicon wafers, an adhesion promoter can be used prior to spin coat the photoresist. Priming improves adhesion by producing an interfacial bonding layer between the resist and the substrate surface.

Baking using a conventional oven leads to the formation of a skin by solidifying the top part of the SU-8 film. This skin can restrict the evaporation of the solvent, resulting in incomplete drying of the film and leaving the bottom part unstacked to the substrate, which results to lift off the crosslinked part during the developing process. In order to work out this problem, a hot plate was used as a replacement to the oven. Using a hotplate bakes the bottom region first, which helps in the evaporation of the solvent.

Insufficient exposure dose results the deepest part of the SU-8 layer (closest to the SU-8/substrate interface) to a non-crosslinked region, which leads to dissolve the underneath part and lift off the top crosslinked region upon development.

Spray development process is recommend for both thin and thick film applications. Optimized spray development process is fast, clean, compatible with high aspect ratio structures and reduces the risk of resist adhesion failure.

6.2.3 Stress and Cracks

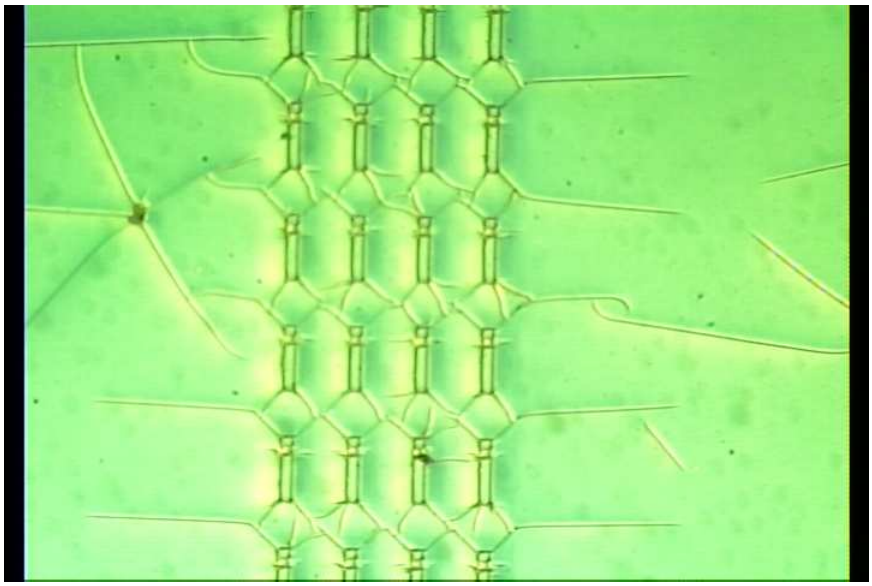

FIGURE 6.4: Cracks and stress of a photopatterned $40\mu m$ thick SU-8 film with small and large holes. SU-8 film is cracked intensively around the holes due their sharp angles and high stress.

During the fabrication the cracks have been appeared on the SU-8 film during the development step (see Figure 6.4). The formation of cracks may affect the performance

of the final structure, leading to leakage in microfluidic channel, or disconnections in the electrical connectors, and also leading distortions, and delaminations. The stress can be also induced on the SU-8 film and creates cracks. Two types of stress can be generated: intrinsic and extrinsic stresses [110, 30]. Intrinsic stress is the stress generated from the movement of the monomer in the crosslinking process, in which there is no much control on it. The extrinsic stress is the thermal stress that generates during PEB which it can be minimized.

It was thought first that the formation of the cracks was due to the long developing time, however it was proved by Miao et al. and Bystrova et al. [12], [21] that the cracks are formed due to the thermal mismatch between SU-8 film and the substrate material. The creation of a large internal tensile stress in the SU-8, which accumulates and builds up during processing in particular post exposure process, and are initiated during the development.

Also the shapes of the patterns assist the generation of cracks, for instance the shapes with rounded corners are less subjected to cracks to those with sharp corner.

Swelling and deformation may also appear after the softbake process. These effects are not only due to the internal forces, but also including normal, shear and friction forces at the interface.

In order to minimize the cracking effect, a relaxation time of 5 to 30 min is recommended between each processing step In order to minimize the internal stress.

The exposure dose has a significant effect on the creation of cracks on SU-8 film. The cracks can be reduced by increasing the exposure dose, however the SU-8 film has to be optimally softbaked. If the SU-8 film is underexposed it will be more susceptible to stress and cracking.

Also optimizing the exposure dose the stresses can be controlled, however, there is a trade-off point between the exposure dose and the resolution which can be decreased if the exposure dose increased, and hence a balancing point between optimal resolution and exposure dose is also required.

During the developing process, using the ultrasonic bath sonicator is strictly avoidable, because it aggressively generates cracks and destroy the SU-8 features.

6.3 Optimised lithography tests

To ensure the good functionality and to check the reliability and repeatability of the home-made SU-8, four different structures with different shapes and sizes were fabricated. Many optimizations in terms of baking time and temperatures, exposure dose and developing techniques were taking in consideration during photolithography tests. In these tests the thickness chosen of SU-8 was approximately $40\mu m$. The sizes of the features are on the range of 150-500 μm. Figure 6.5(a), shows that 500 μm wide channel

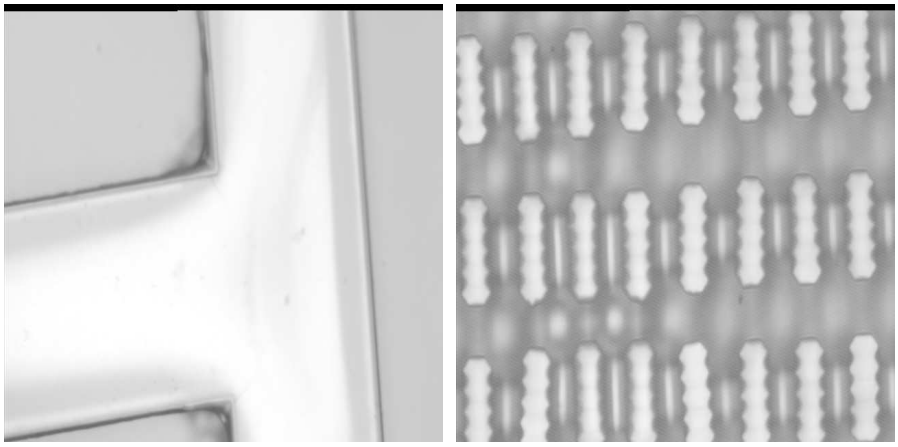

(a) (b)

FIGURE 6.5: 40 μm thick photopatterned home-made SU-8 structures. Figure 6.5(a) shows 500 μm wide "T" shaped microfluidic channel with high resolution and vertical wall profile. Figure 6.5(b) illustrates the good adhesion of 200 μm long bars on glass substrate

is well defined on the edges and good resolution has been achieved. Figure 6.5(b) proves that the SU-8 bars have a good adhesion to the glass substrate which were previously suffer from sticking to it. Figure 6.6(b) shows, a large SU-8 film with square holes. These test shows that there is no stress or cracks around the squares angles. No bubbles traces can be seen on the SU-8 layer. The wall profile of a 150 μm deep hole is measured

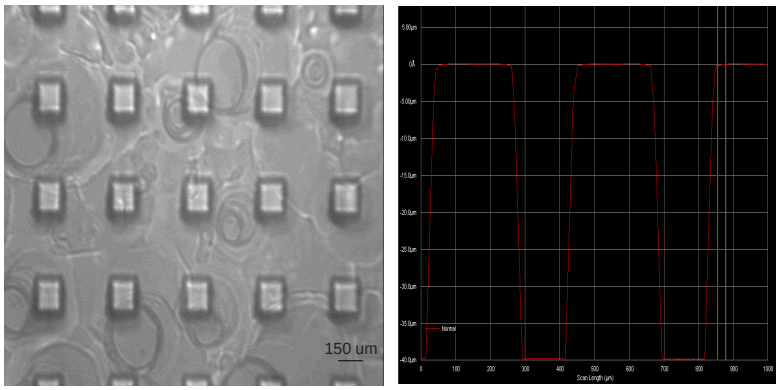

(a) Holes on 150 μm thick of home-made SU-8 film

(b) Profiler measurement of the holes deepness and the walls verticality

FIGURE 6.6: Stress free home-made SU-8 film, no cracks can be seen around the holes, good resolution and good adhesion were also achieved.

and is shown in Figure 6.6(a). Almost vertical walls were achieved, the sidewall angles were around 85^o.

The final optimized recipe of the home-made SU-8 was tested on different structures sizes, thicknesses, and shapes. It proved its functionality with high resolution structures with a good adhesion and controlled sidewall angles (between 80 to 85^o). Also bubbles, stress and cracks were minimized successfully to result in a flat and uniform SU-8 film.

Chapter 7

Device fabrication using C-MEMS technology

In this chapter, the use of C-MEMS technology is presented to construct 3D High Aspect Ratio (HAR) pillar electrodes for the development of the novel AC-electroosmotic micropump. The fabrication strategy used in this work is similar to layer-by-layers concept [134, 79], where multiple coating, irradiation and development steps were applied, each process defines structures at different levels. Problems encountered during the fabrication process and solutions to the problems for making HAR structures were explained. The use of the same material (SU-8) for a filter to improve the verticality and to increase the aspect ratio of the 3D structures during lithography was highlighted. The successfully fabricated electrically-active device was also presented. The device was constructed solely from SU-8 photoresist including the connectors, 3D electrodes, and the microfluidic channel. In this work, the fabrication of the planar electrodes has to be first, followed, by the fabrication and optimisation of the high aspect ratio electrodes and finally the fluidic channel was patterned and sealed.

7.1 Fabrication of asymmetric planar electrodes

In this fabrication approach, only SU-8 photoresist was used to fabricate the full device. The fabrication was carried out in the Integrated Nanosystems Research Facility (INRF), at the University of California Irvine. The INRF facility is a class 1000/10,000 clean room with class 100 work areas. An MA6 Karl Suss contact aligner with a UV broadband source was employed. The humidity within the lithography rooms is controlled to be between 45 and 55% RH. 4 inch diameter thermally oxidized silicon wafers with 5000$\mathring{A}$ SiO_2/Si were used. The oxide layer is required to isolate the connectors and electrodes from the silicon layer. Glass is suitable for microfluidic devices mainly it allows visualization through it and it is a low cost material. However in these particular experiments, Silicon dioxide SiO_2 substrates were used rather than glass due to the use of high temperature (900^{o}C) which is higher than the melting temperature of the glass (which is 500^{o}C).

The planar electrodes (depicted in Figure 7.1) are characterized with smooth planar surface. Their thickness is varied from one material to another, and is usually around hundreds of nanometres as reported in [50]. However dealing with photoresist, the electrodes thickness will be limited by the spinning speed of the spinner, the resist viscosity, and stiffness/fragility of the resist after pyrolysis step. A minimum thickness of 1 μm and 2 μm thick electrodes can be fabricated, however they are too fragile and can be fractured easily during any electrical test, if they are connect to external generator.

Also, in order to reduce the cost of the fabrication and reduce the number of the masks used during the fabrication, the external connectors (electrical pads) and the internal connectors (planar electrodes inside the channel) layouts were drawn on same mask, therefore an optimum thickness between the external and internal connectors was chosen to be 5 μm before pyrolysis for a few reasons. Firstly, the planar electrodes have to be kept as thin as possible, in order to not obstruct the fluid motion inside the channel. Also, the external connectors have to be thick and robust enough after pyrolysis steps in order to survive the electrical clips (alligator clips) during the electrical tests.

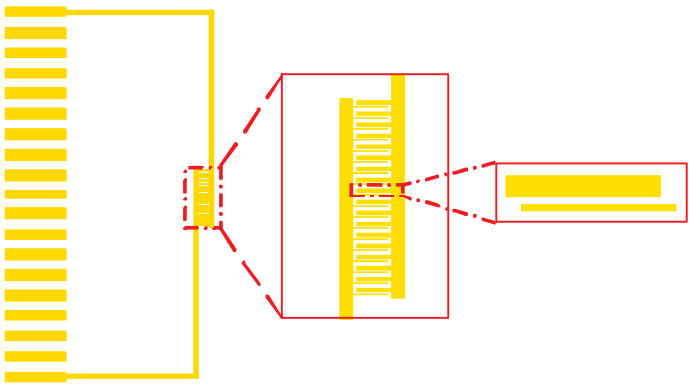

FIGURE 7.1: Shows the layouts of asymmetric planar electrodes (large and thin electrode separated by large and thin gaps) and connected to external pads made out on the same layer

Since the optimised thickness chosen for the planar electrodes in this process was between 5 μm and 7 μm, both SU-8 2 and SU-8 5 can be used.

Patterning a thin photoresist layer and making planar electrodes using photolithography is a simple process, the fabrication process and protocol are shown in Table 7.1.

Both softbake and post exposure bake were performed on a leveled hotplate, to avoid skin effect and ensure a uniform leveled SU-8 film. After the photolithography completed, the standard pyrolysis process presented previously in section 5.2.3 was applied in order to transform the planar electrodes and the connectors to a conductive polymer.

Parameters	SU-8 2	SU-8 5
Spinning Speed 1	500rpm for 10s	500rpm for 10s
Spinning Speed 2	2000rpm for 35s	3500rpm for 35s
Softbake	at 95^o for 2min	at 95^o for 3min
	Cool down for 5min at room temperature	
UV exposure Dose	$10mJ.cm^{-2}$	$10mJ.cm^{-2}$
Post exposure bake	at 95^o for 2min	at 95^o for 2min

TABLE 7.1: Fabrication parameters for making planar electrodes

The important feature in the planar electrodes is they have to be flat enough, in order to implement, the 3D pillars on top of them. A successful asymmetric planar structures were fabricated with good resolution, stress and cracks free, and is clearly

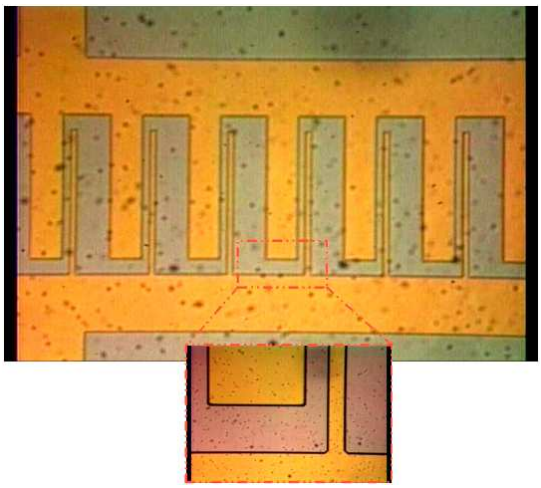

FIGURE 7.2: SU-8 photopatterned asymmetric planar electrodes on SiO_2 (in this picture SU-8 structure appears yellow), the width of the small electrode/ gap is 20 μm and 100 μm for the large one.

shown in Figure 7.2. In terms of flatness the topography of surface was inspected with a confocal microscope, and the measurement is shown by Figure 7.3. It can be seen from the measurement that the surface is over all flat with small roughness. Usually the surface flatness defects appear when the thickness of the structure or the viscosity of the resist increases. The problem are due to a spinning rims at the edge of the wafer, or unintentional tilt of the spinner chunk during spinning. Dirt particles and bubbles also affect the flatness of the surface, and sometimes a curvature of the substrate, all these parameters can reduce surface flatness.

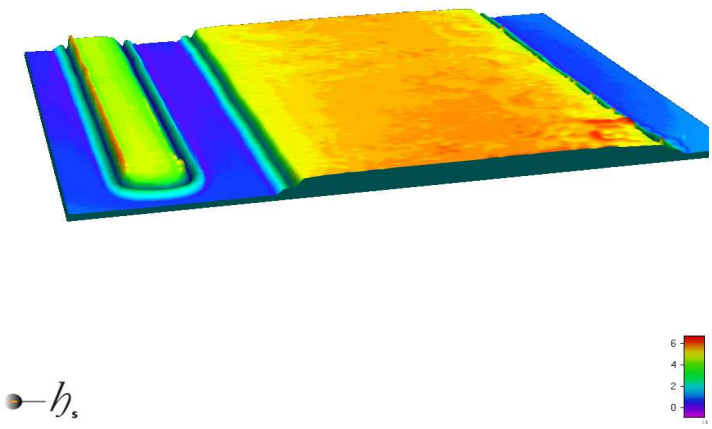

FIGURE 7.3: Planrization of asymmetric planar electrodes on SiO_2.

To enhance the surface flatness, first a good cleaning of the wafer is essential, and before spinning SU-8 photoresist, relaxation time on flat surface is required. Relaxation time is ranged from few minutes up to few hours, it depends on the viscosity of the photoresist used. Relaxation time allows reflowing photoresist, and also it allows the bubbles to be released from the photoresist. During bake steps SU-8 film has to be baked on leveled surface.

In this work the obtained surface of electrodes is flat enough to build on top of it 3D pillars, the roughness of the electrodes does not disturb the following fabrication steps as far as the surface is flat. However rough electrodes may disturb pumping efficiency, but pyrolysis process will smoothen polymers surfaces during shrinkage effect.

7.2 Fabrication of 3D-electrodes

The 3D-electrodes (pillars) are considered to be the backbone part of the micropump in terms of functionality, therefore they have to be accurately fabricated to ensure a proper functionality of the device.

The 3D-conductive electrodes were fabricated by patterning SU-8 on the top of the planar electrodes, and then they were converted to carbon. Due to the shrinkage effect which occurs during the pyrolysis step, the size of the structure can be reduced by (up to) 75%. Therefore, the polymer structures have to be in size 3 to 4 times the final height before pyrolysis. Since the desired height of the final electrodes is around 50 μm, the initial thickness of the polymer structures had to be around 150 μm. The structure is also very dense, the small gaps between 3D-electrodes are 10 μm and 20 μm, and an aspect ratio required is greater than 5:1. The pillars are shaped in squares and rectangulars with a width less than 10 μm.

The highest aspect ratio (HAR) of SU-8 structures reported in the literature were fabricated using LIGA process [15, 16]. LIGA process using X-ray exposure facility is very expensive technology. Alternatively, UV-lithography is an affordable technology

can be adopted instead of LIGA. However patterning a thick layer of SU-8 using standard lithography equipments by especially employing a broadband UV source is a very sensitive process in practice. By following the standard fabrication steps recommended by MicroChem Corp. (see Graphs in 5.3) several effects and problems were encountered during the experiment, because the process was very susceptible to small changes in cleanroom environment, to the fabrication parameters, to the structure dimensions, and shapes. Therefore it was important to optimise the lithography process according to the environment, equipments and structures by finding the optimum parameters for these particular 3D-electrodes structures. In this work it is referred to 3D-electrodes to the pillars that have an aspect ratio around 5:1 or below. Beyond this aspect ratio, the pillars are called High aspect ratio pillars. The experimental aspect ratio (AR) of the pillar is defined as the ratio of the hight to the average width as is it is shown by equation 7.1 [136]:

$$AR = \frac{H}{1/2(W_t + W_b)} \tag{7.1}$$

Where AR is the aspect ratio, H is the thickness of the photoresist, W_t amd W_b are the top and bottom widths of the pillar.

7.3 Optimisation of the lithography parameters

Process optimization were carried out on asymmetric set of pillars with 20x20 μm^2 and 20x60 μm^2 with 20 μm and 60 μm for the small and large gaps between the pillars. The mask used for the pillars is a chrom-on quartz mask (from Compugraphics international,UK) with high resolution of 0.25 μm. The most sensitive parameters in the photolithography are the softbake, UV-exposure and hardbake. Few parameters have direct effect on the structure more than others, these parameters were investigated in these fabrication processes. 6 experiments were carried out for each parameter to find out its optimum value. Each parameter was changed once a time, and all the other of parameters were kept identical. The variation in widths, lengths and gaps dimensions

were monitored and measured using a confocal microscope. The experiment which shows the approximative and the closest dimensions to the desired structure was adopted and fixed to run the rest of the next experiments. This cycle was repeated for the next experiments and at the end the final parameters were fixed. Different SU-8 thicknesses were investigated the highest aspect ratio achieved was around 5:1 for a thick SU-8 layer of 100 μm. The optimisation results are presented in Figure 7.4, widths, lengths and thicknesses were monitored in these experiments. The width and length the most sensitive because they influence on the the gaps dimensions.

The SU-8 used in the described experiments was SU-8 100 formulation (Microchem corporation, MA, USA). A volume of approximately 4 ml of SU-8 was dispensed on the center of the wafer and left for relaxation time of 5 min. Using a Laurell Technologies Corp spinner, a maximum applied spinning speed was 3000rpm, for 35s in order to produce an SU-8 film of approximately 100 μm. Softbake, UV-exposure, and hardbakes times were varied, but development time was fixed. Longer development time causes the collapsing of the pillars. The development was performed in room temperature by immersion the wafers in an agitated container of PGMEA (Propylene Glycol Methyl Ether Acetate) for 7 min, and rinsed with PGMEA followed with Isopropanol.

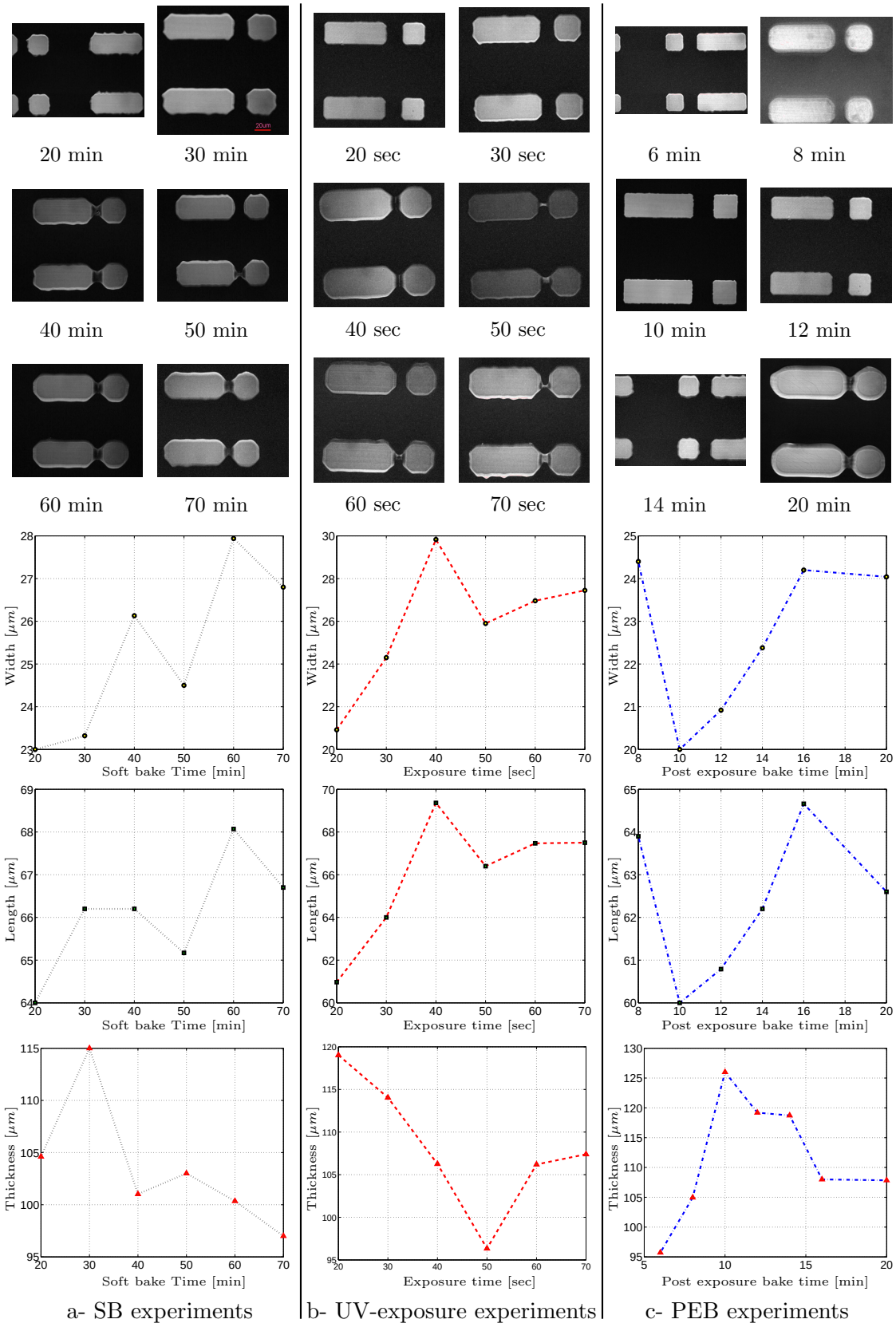

FIGURE 7.4: Experimental optimization of photolithography parameters for the high aspect ratio (HAR) electrodes. The pictures and graphs in the columns a,b, and c illustrate the experimental results for softbake, UV-exposure dose and post exposure bake respectively. The ideal dimensions for the large electrodes/ gaps are 20x60 μm^2, and 20x20 μm^2 for the small ones.

- Softbake optimisation

After the substrates were spin-coated with 100 μm thick SU-8 layers six SiO_2 wafers, a softbake stage was followed in order to transform the SU-8 layer from viscose state to solid film by removing the solvent. The softbake was performed on leveled hotplate, in order to ensure a better uniformity of the thick resist on the substrate. Usually softbake performed in two phases, the first one lasts for 5 min to 10 min at 65^oC and then followed by increasing the temperature gradually to up to 95^oC, however in these experiments, the first phase of the softbake was skipped as it is only useful to reduce the stress for large structures of SU-8. In order to investigate the influence of the softbake temperature on the lithographic performance of HAR SU-8 pillars, the temperature was fixed at 95^oC where the baking time was varied from 20 min to 70 min with a step of 10 min. All other fabrication parameters were kept identical during the experiments. The effect of the softbake on the width, length, and the thickness of large posts is shown by Figure 7.4.

The minimum duration for softbake time was chosen 20 min, because, below this time, high percentage of the solvent remains in the SU-8 film and makes it sticky, which may stick to the mask and perturbs the alignment.

In the graphs shown in Figure 7.4, both widths and lengths seem to behave in the same manner, this means that that there is a uniform variation on the overall structure. In general by increasing softbake time, there is an increase on both widths and lengths.

It can be seen clearly also from the graphs, that the variations in the thickness is independent on the the variations of the width and length. Unlike the length and width, the thickness decreases by increasing softbake time, this is due to the shrinkage accompanied to this baking process. This type of shrinkage is resulted from the evaporation of the solvent which reduces the thicknesses of the films and hence the hight of the pillars was shrunk.

The desired width and length are 20x60 μm^2, from the experiments the approximative dimensions were obtained are 23x64 μm^2, therefore the optimum value for softbake time is 20 min.

- Exposure dose optimization

Similar to previous experiments 100 μm layers of SU-8 50 were spun on SiO_2 wafers. UV-exposure was performed using MA6 Karl Suss contact mask aligner using mercury arc lamp, with a UV-broadband source which produces exposure wavelengths up to 450nm. The intensity of the UV source was adjusted to be 10mW.cm^{-2}. The recommended exposure time from MicroChem Corp. for such thickness is somewhere between 350-550 mJ.cm^{-2}, which corresponds to an exposure time between 35-55 sec. In these experiments the exposure time was varied from 20 sec to 70 sec with 10 sec step. Below 20 sec the structures will not polymerize and they end up with collapsing. The softbake time was fixed to its optimum value of 20 min, but the other parameters (post exposure bake and development time) were kept fixed (unchanged) during the experiments.

From the graphs in Figure 7.4, it can be noticed that the UV-irradiation has a uniform effect on both the widths and lengths of the structures. This means that there is a uniform absorption of UV light across the SU-8 film. In general from these graphs by increasing the exposure time both widths and lengths increase. In addition it can be seen also from the pictures in Figure 7.4 that the increase in the exposure dose prevents narrow gaps which were exposed for more than 30 sec from developing out. Any connection between rectangular and square pillars is considered as short circuit in the final structure, therefore it is important to fabricate clear gaps between the structures. From the graphs the lowest exposure time (20 sec) which corresponds to an exposure dose of 200 mJ.cm^{-2} shows the optimum value of the exposure dose, the obtained dimensions for the width and length were 21x61 μm^2.

- Post exposure bake optimization

In these experiments 100 μm layers of SU-8 50 were spun on SiO_2 wafers. The experiments were carried out in similar conditions to previous experiments, apart from the UV-exposure time was fixed to 20 sec. The post exposure bake (PEB) was performed on a leveled hotplate. The PEB time was varied between 5 min and 20 min, Microchem Corp. time recommendation is 10 min. In order to reduce the photo-acid diffusion, post exposure bake was performed immediately after UV-exposure step.

From the graphs Figure 7.4 the widths and lengths increase by increasing the Post exposure bake. In fact during post exposure has same effect as the softbake, which means exceeding the required baking time leads to crosslink unexposed regions of SU-8. The optimum post exposure time was 10 min, the width and length of the structure were 20x60 μm^2 which corresponds to the mask's dimensions with a resolution around 1-3 μm. A clear gaps between pillars were also accomplished.

7.3.1 Effect of the lithography parameters on the shape

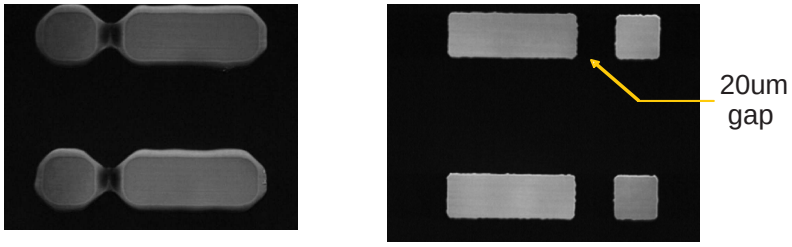

FIGURE 7.5: Show comparison between high-aspect-ratio pillars before and after optimisation process, these posts are 150 μm thick. The picture on the left shows high-aspect-ratio pillars before optimisation, the angles of the pillars are not sharp, the gaps between the large and small pillars are not clear. After optimisation of photolithography parameters, a good resolution, sharp angles, 20 μm clear gaps, and vertical walls of the pillars were archived (picture on the right).

During the optimization of the lithography parameters, not only the dimensions of the structures were changed, but also their shapes on the three axis XYZ. Considerable evaluation in shape can be seen in Figure 7.5, where starting from octagons and terminating with squares and rectangles after the optimization with good resolution.

$$r = \frac{3}{2}\sqrt{\lambda(s + \frac{1}{2}d)} \tag{7.2}$$

In terms of resolution, the theoretical resolution r of the optical lithography is given by equation 7.2 [101], in which λ is being the wavelength of the lithography lights (usually between 365nm-405nm), and s ($\cong 0.5\mu m$) is being the air gap between the mask and SU-8 layer, and d ($\cong 100\mu m$) is defined as the thickness of the SU-8 layer, this gives a resolution between 6 to 9 μm which was the case before optimization. After the optimization process, a resolution of about 3 μm was achieved.

To quantify the variations in shape, three coefficients were defined in order to monitor and characterize the behavior of these specific SU-8 structures during lithography process.

- Angle coefficient

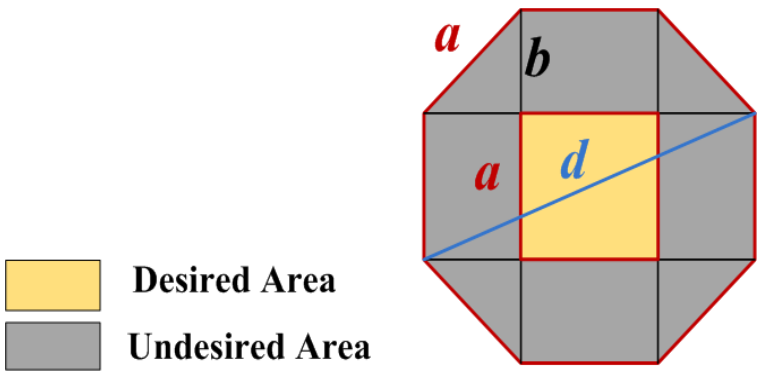

FIGURE 7.6: The square (yellow) which is the desired shape for the HAR pillars is surrounded by undesired surface to form a regular octagon (gray).

Since sharp angles of the pillars are required, to generate high electric field, therefore it is important to monitor the variation of pillars angles during the variation of lithography parameters. From the SEM images in Figure 7.4, most of the structures have an octagon shape, however the required shapes are squares and rectangles instead.

$$d = \sqrt{a^2 + (2b + a)^2} \tag{7.3}$$

In order to quantify the angle variation, the octagons are assumed to be regular (see Figure 7.6) in order to simplify the calculations. The equation of Angle coefficient is

being defined by equation 7.3. If the value of "b" decreases, the angle coefficient will also decrease, The smallest angle coefficient, the closest to a square shape.

- Verticality coefficient

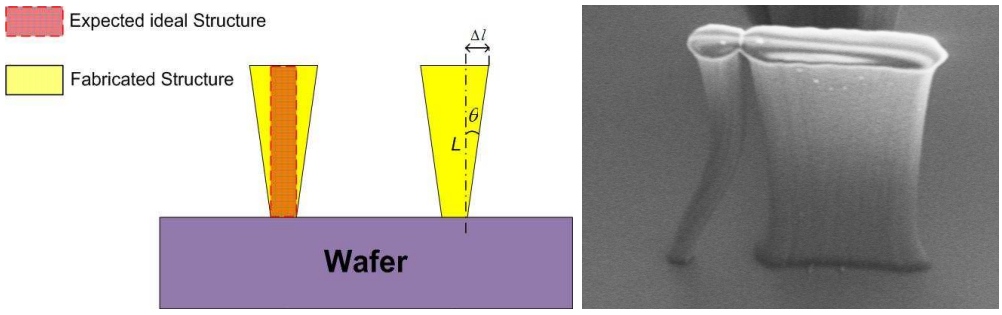

(a) (b)

FIGURE 7.7: a- Verticality schematic of the pillars. b- SEM image illustrates the inclination in the pillars walls

$$Tan\ \theta = \frac{\Delta l}{L} \tag{7.4}$$

The verticality coefficient is used to define any inclination of the pillars walls. Is being calculated by the variation in the angle θ as is shown by equation 7.4.

- Expansion coefficient

$$Expansion = Volume_{obtained} - Volume_{ideal} \tag{7.5}$$

The expansion coefficient is being the excess in dimensions of the structure, and is defined as the difference between the obtained volumes and the desired (Ideal) one.

7.3.1.1 Effect of the softbake on the shape

At 20 min, the expansion and verticality coefficients seem to be high in these tests, the only interpretation at this point that the pillars were not completely developed. All the

coefficients seem also to increase by rising the baking time, this gives clear view that the lowest baking time will give good verticality, near mask dimensions and sharper angles. Also from the angle coefficient graph it can be seen clearly that there is an isometric change in both sizes of the widths and lengths.

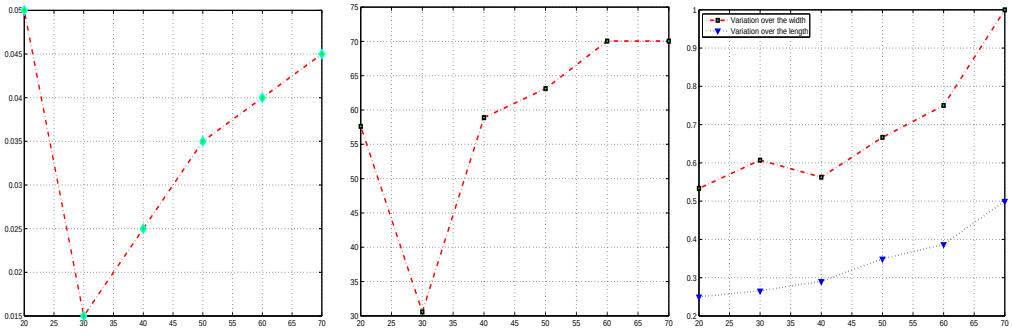

(a) Verticality coef. variation (b) Expansion coef. variation (c) Angle coef. variation

FIGURE 7.8: Graphs show the variation in the verticality, expansion, and angle's coefficients as a function of softbake variation.

Mostly in these tests, the minimum value of the coefficients gives better profile of the posts. However, by increasing post exposure bake results to an increase in crosslinking density, but will also cause the polymerization to progress further and expand the volume of the structure.

7.3.1.2 Effect of the UV-exposure on the shape

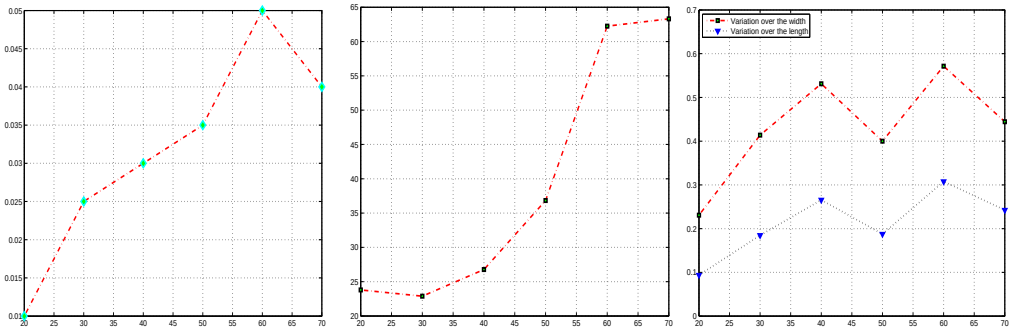

(a) Verticality coef. variation (b) Expansion coef. variation (c) Angle coef. variation

FIGURE 7.9: Graphs show the variation in the verticality, expansion, and angle's coefficients as a function of UV-exposure variation.

At the lowest exposure time (20 sec) which corresponds to an exposure dose of 200 mJ.cm^{-2}, the HAR pillars shows the lowest coefficients values. Both expansion and verticality coefficients raise dramatically by increasing the exposure time. With regard to the angles, a slow variation can be seen, a peak value for all coefficients of the exposure dose can be clearly observed at 60 sec. In these experimental the obtained results indicated that the longer exposure time resulted in an increase in side walls angle and narrower gap, therefore the optimized exposure time of 20 sec has given better profile of the pillars.

7.3.1.3 Effect of the Post exposure bake on the shape

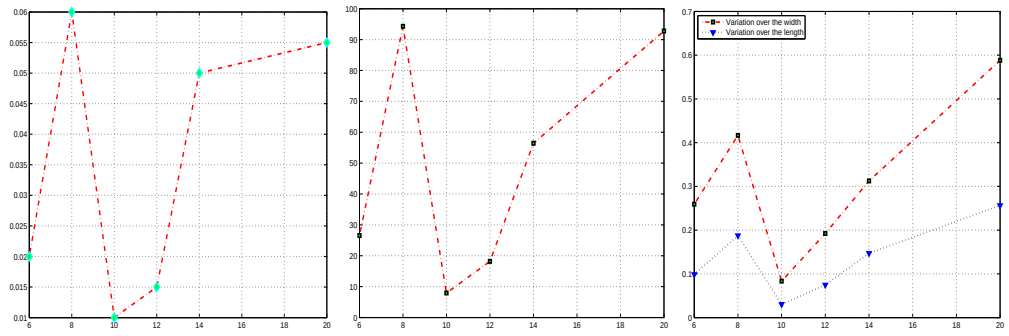

(a) Verticality coef. variation (b) Expansion coef. variation (c) Angle coef. variation

FIGURE 7.10: Graphs show the variation in the verticality, expansion, and angle's coefficients as a function of Post exposure bake variation.

The effect of the PEB on different coefficients is presented by Figure 7.10. It can be seen from all the graphs in Figure 7.10, that the optimized PEB time was 10 min. Lower baking time leads to a slight increase in all the coefficients. By increasing the PEB time, a rapid increase in all the coefficient values can be clearly seen. PEB was found to be a key factor for polymerization of the structures [76].

7.3.2 Discussion and analysis

A proposed fabrication process was derived from optimizing the lithography factors to improve the patterns quality. The obtained output structures are shown in Figure 7.4.

A HAR pillars of more around 5:1 was also obtained with straight sidewall profile, a clear gap of 20 μm was reached. Also adequate resolution on the edges of the structures has been also achieved.

In the above experiments the effects of processing parameters on the profiles and gaps of 3D-electrodes were highlighted. The softbake which was thought that has a small effect on the optimization process, but in fact has a crucial effect on the lithography process. Increasing softbake time will lead to increase the structures dimensions. This increase is due to a thermal crosslinking, which may initiate without the activation of the photoinitiator [10]. In contrast at lower softbake time the solvent remains in the structures, which affects the photoacid generation process during UV-exposure. The cation of the onium salt is destroyed and the salt decomposes, where the anionic component reacts with solvent monomer, or impurity molecules in the photoresist to form a strong acid. Increasing the solvent concentration facilitates this process, and increases the sensitivity and crosslink density [3].

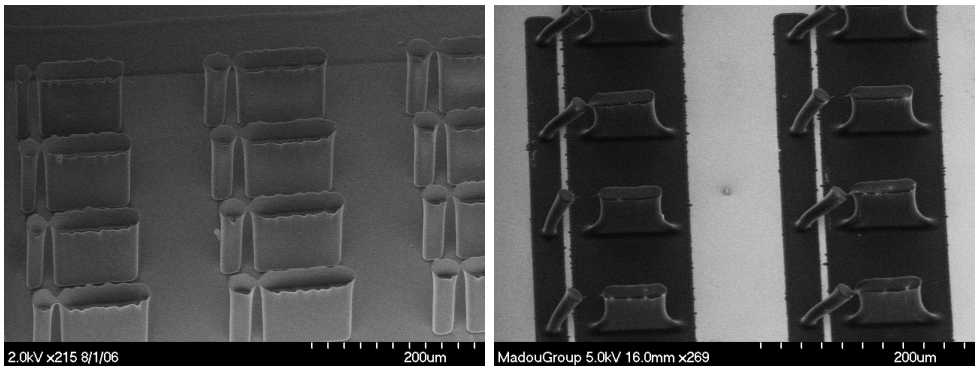

(a) Before pyrolysis (b) After pyrolysis

FIGURE 7.11: Shows skin effect. On the left the gaps between the posts are clear, however on the top of the posts a thin layer connects the large and the small posts together. On the right, this thin layer remains after pyrolysis step. Due to shrinkage effect the small posts were inclined towards the large ones after pyrolysis.

Using an oven instead of the hotplate in order to improve the structures profile, however the skin effect is introduced as an alternative problem. Skin effect is the creation of a thin layer of the resist at the top of structure, results to the enlargement of the top surface of the desired structure. The oven bakes the top part of the resist first then the bottom one, this makes the top part of the structure more exposed to the temperature

which leads to initiate a thermal polymerization. In contrast the hotplate bakes the bottom part first followed by the top part which helps to evaporate the solvent and gives more rigid structure.

Skin effect is considered as a serious problem in this work, despite the thin layer which can be formed on the top (see Figure 7.11(a)), but it lasts even after pyrolysis process. As a consequence it will cause a short circuit after converting the SU-8 structure to a conductive polymer. By taking the advantage of shrinkage effect during pyrolysis process in order to remove the hanging connection between the pillars, however the pillars tend to incline rather detach as is shown in Figure 7.11(b). The inclination of the pillar also will cause a short circuit, during the electrical tests.

Similar enlargement of the structure at the top can be occurred due to the diffraction effect of UV light (Frasnel diffraction) [101, 60]. The diffraction of UV light is caused by the presence of the air gap between the mask and SU-8 layer surface, as a consequence of unconformal contact of the two surfaces. The unconformal contact is resulted to the flatness error of the photoresist, which is inevitable for thick layers. The diffraction error increases with the increase of the resist thickness and gap distance. Consequently, it results to an increase of wall widths and sloped sidewall (inclined profile) and more severely constrains for the applications of microstructures in HAR range [75, 29, 136].

7.4 High Aspect ratio electrodes

The optimization process seemed to work for structures for an aspect ratio of up to 5:1 of 100 μm thick SU-8 layer and gaps of 20 μm. However, beyond this aspect ratio th optimization process does not work for thicker layers. A slight change in any lithography parameters leads the pillars either to bend and collapse, or the gaps between the pillars to be eliminated as it can be seen in Figure 7.12.

After the structures have been patterned, softbaked and exposed to UV-light, the resulted structures suffer from an exaggerated rough sidewall, geometry losses problems, gap elimination and collapsing.

The problem was thought that was due to the exposure dose, where many Exposure doses, were investigated. With a measured exposure time determined for the thickness of resist used, insufficient crosslinkage occurred at the base of the pillars. Figure 7.12(a) shows the result. The pillars have collapsed against each other due to the lack of structural rigidity close to the substrate.

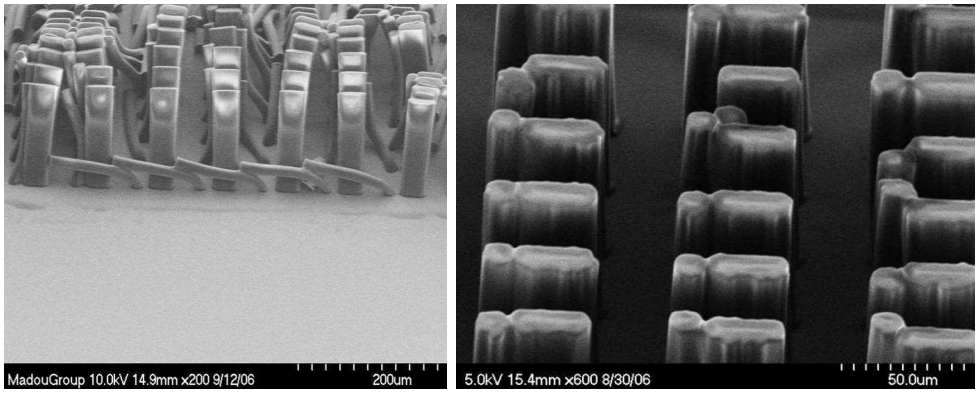

(a) Low exposure UV dose (b) High exposure UV dose

FIGURE 7.12: Shows T-topping problem. On the left at high UV-exposure T-topping effect and gaps elimination occur. On the right at low UV exposure HAR posts collapse because of weak crosslinkage at the bases of the pillars due to insufficient penetration of UV dose to the far bottom of the SU-8 layer.

Increasing the UV dose did not overcome the problem, pillars were still structurally weak at the base, but now the upper part of the pillars were over exposed and the smaller gaps did not develop out, as shown in Figure 7.12(b).

Similar effect occurred even by varying the duration of the softbake and post exposure bake. Thus was found that the problem was related directly to the UV broad-band source. The UV broad-band source combines both shorter and larger wavelengths, it exposes across the spectrum 230 nm to 450 nm range.

The structures profile was affected by the uneven penetration of UV-light inside the thick SU-8 resist layer. The light intensity drops gradually from the top to the bottom as the light is absorbed. As a result the top part of the pillar absorbs higher dose of UV-light than the bottom part, which is considered also as a major reason in creating T-topping effect. The UV absorption spectrum of unexposed SU-8 resist shows much higher absorption of short wavelengths than long wavelengths. Also the absorbance changes during the exposure, where shorter wavelengths light intensity drops very fast for thick layers which results in incomplete crosslinkage of the structures. However longer wavelengths component penetrate further down and irradiates the bottom portion of the structures [101].

7.4.1 Home made filter

During lithography process, contact mask aligner (Karl Suss) was employed, UV light source of the mask aligner was a mercury short arc lamp (OSRAM 350w) with a spectral regime starts from 210 nm to more than 500 nm as it is depicted in Figure 7.13(a) [91]. This transmission spectrum can be divided to shorter wavelengths ($<$ 365nm), and longer wavelengths ($>$ 365nm) with main peaks at 365 nm (i-line), 405 (h-line) and 436 nm (g-line). In order to expose HAR features uniformly with UV light, only longer wavelengths are desired. Therefore an optical filter is desired to provide selective illumination of only longer wavelengths.

Commercial cut-off filters are expensive, antireflection coatings (ARCs) also increases both the cost and the complexity of patterning. However SU-8 film was found that can absorb short wavelengths below 365 nm as it can be seen by Figure 7.13(b) [122]. This means that it behaviors as an optical filter, and capable to remove shorter wavelengths,

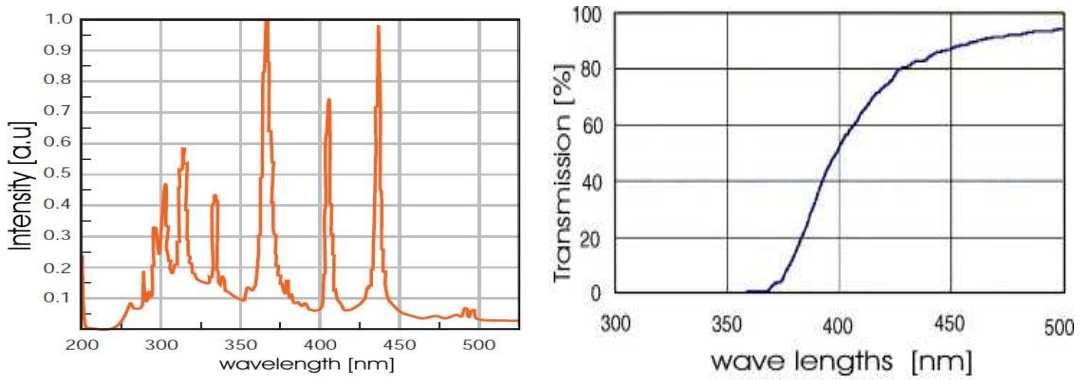

(a) Resulting transmission spectra of Karl Suss UV-broadband source with a mercury short arc lamp (OSRAM 350w). [91]

(b) UV transmission spectra after the use of SU-8 on glass filter, which eliminates undesirable shorter wavelengths.

FIGURE 7.13: UV transmission spectra of Karl Suss broadband source and of the filtration of shorter wavelengths using SU-8 filter.

below 365nm. Taking this advantage, and as a part of using SU-8, a home made filter was then fabricated.

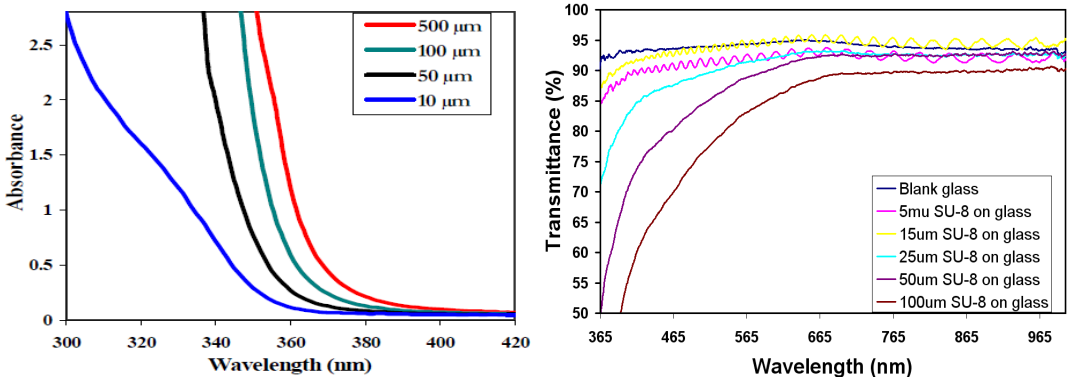

(a) (b)

FIGURE 7.14: a- SU-8 absorbance of shorter wavelengths which increases as the the thickness of the film increases [80]. b- The transmittance measurements for different thicknesses of SU-8 layers.

According to SU-8 manufacturer (MicroChem Corp.), SU-8 absorbance of shorter wavelengths increases with the increase of the thickness this can be seen clearly in Figure 7.14(a) [80], which means that thick SU-8 films are desirable as filters then the thin ones. Also the transmittance measurements for different thicknesses of SU-8 (from 5 μm to 100 μm) has shown that thin SU-8 films (5 μm and 10 μm) are have an oscillating profile of the optical transmittance.

The wobbles in the transmittance versus wavelength plots are due to interference of light reflected from the top surface of SU-8 with light reflected from the SU-8/glass interface [13]. The phase of the two reflected waves differs because of the extra distance that the light reflected from the SU-8/glass interface has traveled compared to light reflected from the SU-8 surface. There is also a π shift in phase upon reflectance from a material of a higher refractive index. If this phase difference is a whole number of wavelengths, then the two reflected waves are in phase and so constructively interfere, resulting in a high intensity. Conversely, if the phase difference is an odd multiple of half wavelengths, then the waves will be π degrees out of phase and so will destructively interfere, resulting in a low intensity. The phase difference is dependent on the wavelength and so as the wavelength is increased, the two waves alternate between constructive interference and destructive interference, through all intermediate amounts of interference, hence leading to the alternating maximum and minimum on this SU-8 transmission graphs. In this work the transmission of 5 μm SU-8 layer is modeled by Stuart A. Boden and can be shown in 7.15.

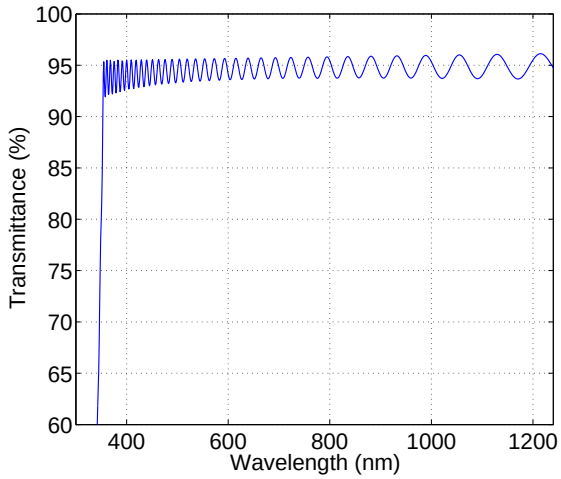

FIGURE 7.15: Modeled interference SU-8 thin films on glass.

This is only seen for the thinner films because as layer thickness is increased, the path difference becomes greater than the coherence length of the light and so interference is no longer possible.

SU-8 filter was fabricated by spinning thick SU-8 layer directly on top side of the

mask, in order to reduce, any light diffraction or refraction rise from air gaps or variation in refraction index. To avoid rippled surface and to ensure a good layer flatness and thickness uniformity, the filter thickness was limited to 100 μm. Since the mask was fabricated from glass, and the adhesion of SU-8 to the glass is weak, softbake time was increased to 1 hour under 95^oC on leveled hot plate, in order to increase the adhesion.

Then the SU-8 film was exposed to 6 multiple exposure dose of 120mJ.cm^{-2}. Multiple UV exposure time sequences were preferred instead of a single longer exposure time, in order to have a crack-free film and flat surface. The excessive amount of UV energy, heats up the polymer which may melt and deform the surface flatness or provokes cracks. Post exposure bake were performed and followed by hard bake subsequently for 2 hours on a leveled hotplate.

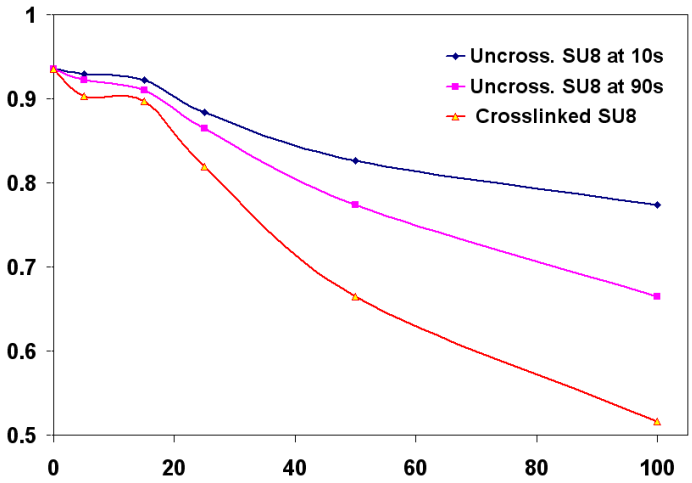

FIGURE 7.16: Energy Drops of the UV light as the function of different SU-8 thicknesses ranging from 10 μm to 100 μm for crosslinked and uncrosslinked films . The uncrosslinked filters were just exposed to UV-light for 10s and 90s without being post exposure baked before using them.

Using recommended exposure dose on SU-8 films with the presence of the home-made filter, shows that UV illumination was not enough to polymerize the SU-8 structures. An investigation was conducted to investigate the effect of the SU-8 filter on SU-8 structures, where the UV light intensity was measured on different thicknesses of SU-8 filters at the input and output of each filter. The measurements were taken by UV intensity meter detector Model 1000 Suss microtec at 405 nm wavelength. The results depicted in Figure 7.16 show that the light intensity drops as the thickness increases,

also the less SU-8 is exposed to UV light the more it can absorb UV light. Uncrosslinked SU-8, has shown high light intensity absorbance, where for 100 μm thick film there is a significant drop in light intensity, which almost to 80% of incident light. This drop of light intensity is related to the elliminated wavelengths as the high range of wavelength filtred will give low outpu ligh intensity.

Using the home-made filter which eliminates all non desirable shorter wavelengths, results in a uniform and deep polymerization of the structures.

An increase in the aspect ratio of the pillars to more than 10:1 was achieved, with straight wall profiles. A good geometries and shapes fidelity was also achieved. High resolution of the structures with very smooth edges also obtained. However a new problem was raised where the top of each pillar sticks to the adjacent one as it is shown in Figure 7.17 .

7.4.2 Stiction effect

T-topping and structure enlargement, collapsing problems were solved, the aspect ratio was doubled from 5:1 using a broadband source to more than 10:1 using an SU-8 filer. However, a new problem was raised, where the top of small pillars overhang the top of large pillars (see Figure 7.17).

This problem was first thought that the problem was due to the low stiffness of the structure as a consequence insufficient softbake. However, by increasing the softbaking time to up to 30 hours at 95^oC for a 200 μm thick layer did not show any improvement.

Also drying up process after development with gentle stream of air or nitrogen was thought that was the responsible for making this effect to occur. However, by leaving the structure to dry up without applying any additional drying source did not give any positive results.

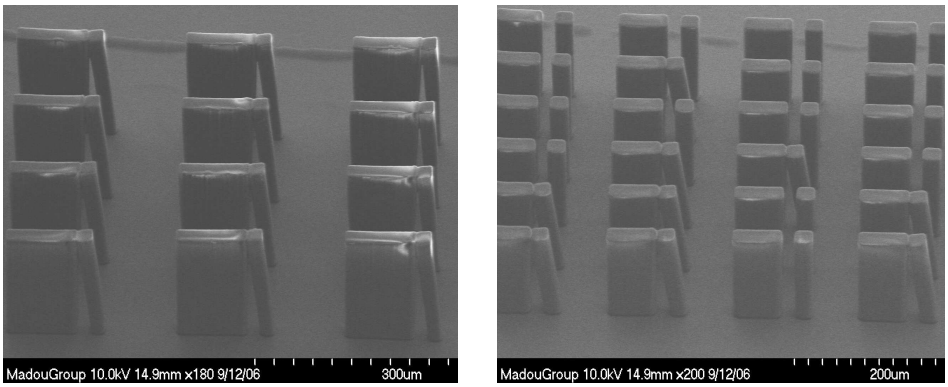

FIGURE 7.17: Shows stiction effect, each pair of large and small electrodes can stick together (picture on the left), or it can be partially where only few pairs can stick together (picture on the right), but in both cases it remains a problem as it creates a short circuit in the final device.

Also was thought that it was due to the aggressive agitation of the structures during the development process. Therefore, alternative, techniques were used, mainly leaving the structure inside the developer for longer period without any agitation, however long development time leads SU-8 structures to delaminate and cause the collapsing. Neither smooth stirring nor ultrasonic developments gave good results also.

To figure out what was the problem, the development process was performed under the microscope. After diffusion of developer molecules into uncrosslinked photoresist, and a complete diffusion of solvated uncrosslinked polymer chains into the developer, the SU-8 structure was removed from the developer container. Immediate inspection, showed that the pillars seemed to be straight with the presence of the solution. However, immediately after the developer evaporates the pillars started to hang each other, this phenomenon was known as stiction effect [62, 37, 124, 93].

During the development process, due to the capillary forces acting on the on the SU-8 walls, the developer rises between each pair of pillars, and then the solvent droplets evaporate. As this occurs, the thin pillars bend as they are less stiff than the larger ones, which brings the two adjacent pillars heads together because the pillars are high enough and so are very sensitive to any motion from the top. The pillars heads are then stuck firmly together due to the presence of viscous SU-8. Capillary forces increase with

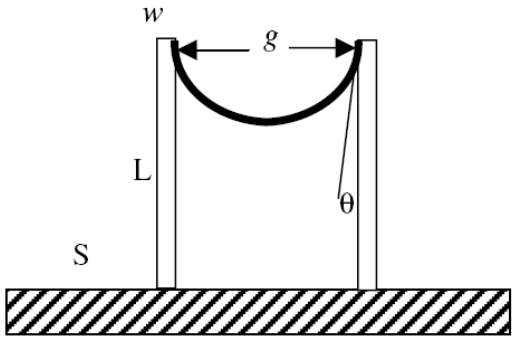

FIGURE 7.18: Schematic shows stiction effect, where between two pillars with a gap g, width w, and hight L, a fluid droplet can be subjected to porous effect, the droplet moves from the bottom to the top of the pillars, before it evaporates, it will bring the tops of the pillars together.

the increase of surface tension of the developer, and decrease the contact angle between liquid and resist as it can be seen in Figure 7.18 [69].

In order to workout this problem, a dry release process can be used [27, 57, 123], however it requires a special set of equipments and large processing time. However, other fabrication processes were tested, where after removing the wafer from the developer container, was put immediately on a hotplate in order to accelerate the evaporation speed. However, the stiction effect was always present and no changes were noticed by using different temperatures (between 95^oC and 200^oC).

According to equations 7.6 and 7.7 that the dimensions of the pillars determine their strength, and the distance between them defines the strength of the attractive force. The force increases according to the gap between the pillars. The small, closely spaced pillar are more subjected to the stiction effect. The capillary forces which cause the stiction effect between two planes of square pillars with side cross section "w", and hight L, separated by a gap "g", and a surface tension of the evaporated solvent γ is given by equation 7.6 [69, 66]

$$F = \frac{2\pi w L \gamma cos\theta}{g} \tag{7.6}$$

The stiffness of the pillars is defined by Young modulus, a high Young modulus after processing is important to insure a good mechanical stability of the pillars. The critical Young's modulus in which the pillars withstand the capillary drainage is given by equation 7.7 [69]:

$$E = \frac{24\gamma L^4}{w^3 g^2} \tag{7.7}$$

From equation 7.7, it can be seen that Young modulus of SU-8 is constant (4.4 GPa), the pillars dimensions (w, L), and the gap g, that are fixed constants and can not be changed. However, reducing the surface tension γ of the last liquid used to wash the samples can reduce the force on the pattern during drying and thus prevent pattern collapse. Therefore, immediately after developing steps using SU-8 developer, the wafer was immersed for 2 minutes in an Isopropanol container, since Isopropanol is an environment friendly compatible with SU-8 developer. Then the wafer was immersed for an other 2 min in methanol container to ensure that the pattern was filled with methanol as replacement to the SU-8 developer and Isopropanol. Replace SU-8 developer with methanol because it has relatively high surface tension to Isopropanol and Methanol according to reference [108].

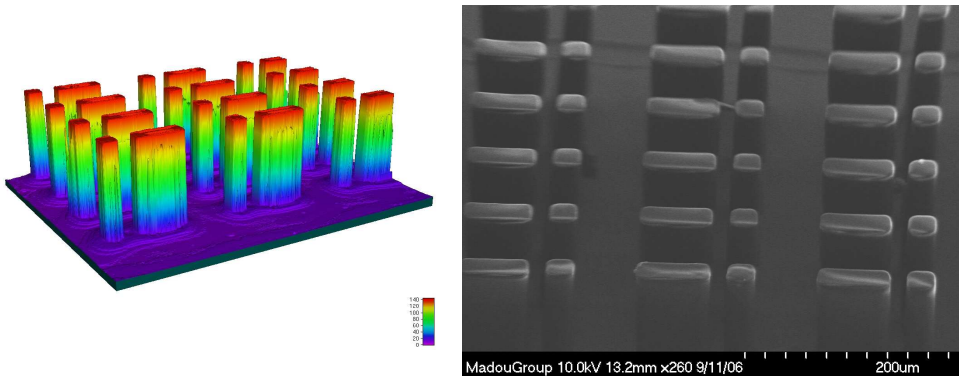

FIGURE 7.19: After the elimination of the stiction effect, 150 μm high-aspect-ratio posts with clear gaps, high resolution were achieved

After drying up the structures, good results were easily achieved using this approach, where a dense structure with 150 μm high and 20 μm gaps was achieved successfully as depicted by Figure 7.19.

7.5 Combination of Planar and 3D

After the fabrication processes for both asymmetric planar and HAR pillar electrodes were completely optimized, at this stage the combination of both planar and HAR 3D-electrodes is required. At first a 5 μm layer of SU-8 was spun and patterned on the wafer, then pyrolized. The resulting structure is a carbon asymmetric electrodes pattern with approximately 4 μm thickness (see Figure 7.20(a)).

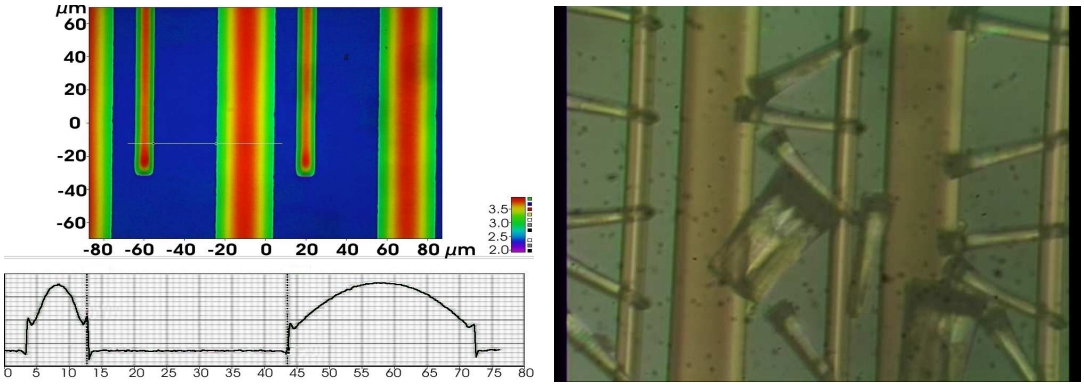

(a) (b)

FIGURE 7.20: (a) The profile of planar electrodes was measured with confocal microscope after pyrolysis process, the surface of the electrodes was changed due to shrinkage effect. (b) Collapsing of HAR SU-8 posts after patterning them on the top of Carbon-planar electrodes. SU-8 posts collapse due to non-uniform profile of pyrolyzed planar electrodes.

It can be clearly seen from Figure 7.20(a) that the planar electrodes are not flat, showing curved surface due to the shrinkage effect occurring during pyrolysis [92]. This makes secondary fabrication of HAR pillars on the top of bumped surface almost impossible in the next step. By spinning a thick layer of 150 μm on the pyrolyzed planar electrodes, and pattern them, was resulting to pillars collapsing as it can be seen in Figure 7.20(b), all the pillars collapsed due to the bumped surface.

The initial intention was to fabricate the planar electrodes layer, perform pyrolysis, and then test the electrical conductivity before progressing to next step. However, this electrical inspection was skipped as the HAR pillars set has to be implemented on the top of flat planar electrodes surface before the pyrolysis step. Consequently, the

pyrolysis process is performed once the combination of both planar and HAR electrodes are patterned and aligned together as one block.

7.5.1 Refractive index problem

Due to the same reflexion index of both SU-8 5 and SU-8 100 (n= 1.667 at $\lambda = 365$nm, 1.650 at $\lambda = 405$nm) for planar electrodes and HAR electrodes respectively, consequently by spinning a thick layer of SU-8 100 on a 5 μm patterned layer of SU-8 5 the alignment of both layers during the lithography process became impossible since the alignment marks on the bottom layer cannot be distinguished from the top layer.

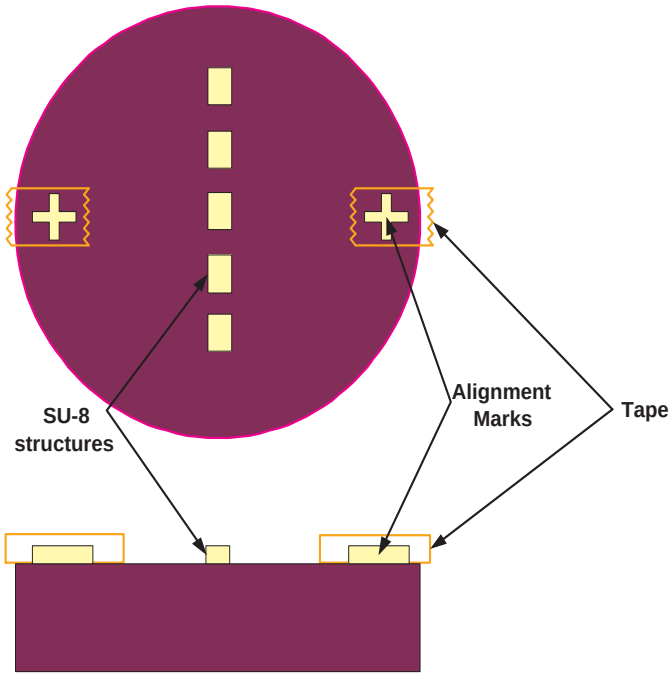

FIGURE 7.21: Top and cross section views of the alignment marks on the wafer. The main alignment marks were covered with tape from the next spinned SU-8 layer

In order to overcome this problem, the alignment marks of the the first layer were covered by tape before spinning as it can be seen in schematic in Figure 7.21. The tape was removed immediately after performing the softbake before the SU-8 layer cooled down and solidified. Alternatively, changing the the optical characteristics of the SU-8 5 can be possible approach, by adding ink to SU-8. The first approach was used due to its ease and practicality, in contrast to the latter one which requires more investigation

time to optimize the process parameters. The only inconvenient with this method is by Spinning SU-8 100 on top of the tape will slightly disturb the uniformity and the planarization of SU-8 film on the edges, since the tape is thick relatively to the SU-8 layer. Consequently this may affect the proximity-gap between the mask and SU-8 layer which leads to diffraction. However, this can be minimized by using air gap compensation Glycerol liquid.

Recently a colored SU-8 has been released in the market and can be a good solution also instead [59].

7.5.2 Drag effect

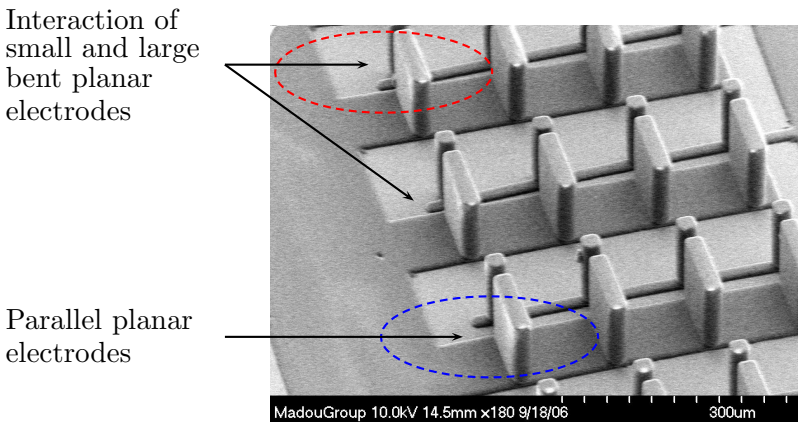

FIGURE 7.22: SEM image of pillar electrodes on asymmetric electrodes. The circled areas show the drag effect, where the planar electrodes were dragged by high viscous photoresist during the second spinning step in the photolithography process. It can be seen clearly that some of thin electrodes and large electrodes are in contact, by comparison the lower (blue) circled area shows an undisturbed electrode.

Since the thickness of the HAR electrodes had to be at least 150 μm, a thick photoresist such as SU-8 100 was required. However, due to the high viscosity of SU-8 100 (51500 cSt), due to viscous and centrifugal forces, the existing thin patterned layer of SU-8 5 (the planar electrodes on the bottom) were dragged and moved from thier initial positions as shown in Figure 7.22. This results in two problems. First the design (shape, size and position) of the electrodes is essential in generating the fluid pumping action, therefore any variation will affect the pumping. Second, if the electrode is dragged into

contact with an adjacent electrode which will introduce a short circuit to the device. A short circuit renders the device unusable. Therefore, in order to circumvent this problem the viscosity of the SU-8 100 was reduced using the organic solvent gamma-butyrolactone (GBL), or by using multiple coats of SU-8 50 which has a lower viscosity (12250cSt).

7.6 Pyrolysis step

Using the previous optimized techniques, a full array of HAR electrodes was successfully patterned on top of an asymmetric set of planar electrodes. The sample is then subjected to pyrolysis process, which consists of heating up the structures inside a furnace at 900^oC. It is performed in a non-reactive environment, which takes place in flow-through furnace using a quartz tube. This process lasts for approximately 7 hours spited into two steps. Firstly the SU-8 structure is postbaked for 40 min at 300^oC under Nitrogen gas (N_2) for 10 min, followed by heating up to 900^oC under N_2. Secondly the sample is maintained at 900^oC but this time in the presence of the forming gas ($95\%N_2$, $5\%H_2$) for 1 hour. Finally, the wafer was left to cool down to room temperature under N_2 gas for around 10 hours.

During pyrolysis process the SU-8 polymer was transformed into a conductive glassy carbon material with an amorphous structure. A reduction in volume occurs during pyrolysis can clearly seen in Figure 7.23(b). The base of the structure being closely adhered to the substrate, does not deform noticeably, while the top of the structure shrinks considerably. As the width of the structures increases the curvature increases.

Overall uniform structures were obtained with smooth surfaces and high resolution as is shown by Figure 7.23(a). A final aspect ratio of more than 12:1 of 4 μm square sides electrodes and a gap of less than 15 μm, was achieved as it is depicted(Figure 7.23(b)).

7.6.1 Shrinkage effect

After HAR pillars were fabricated using SU-8, pyrolysis step was devoted. Because the high temperature applied the structures were downsized. SEM pictures in Figure 7.24

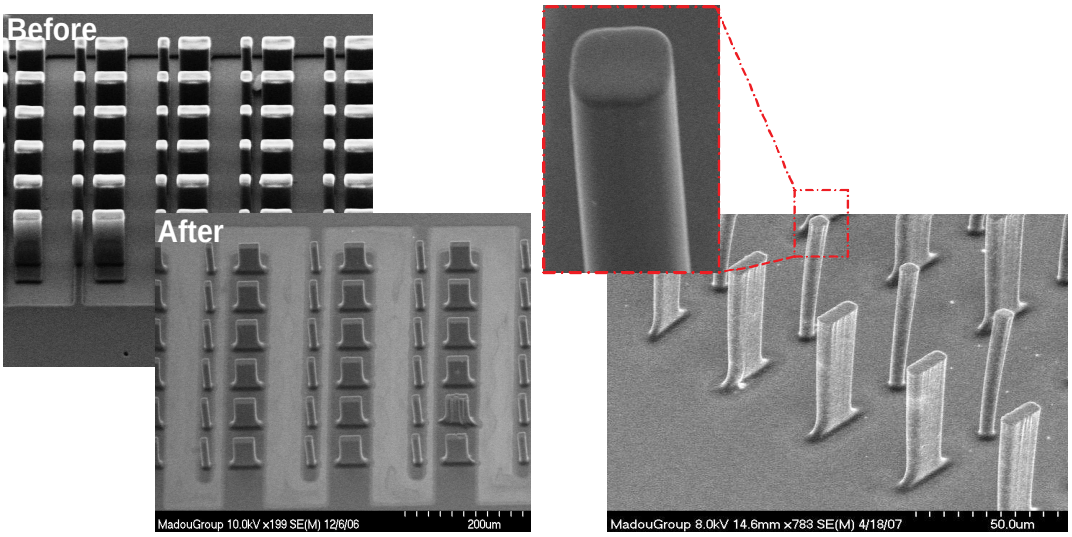

(a) (b)

FIGURE 7.23: (a) SEM images showing a set of HAR pillars before and after pyrolyzation. (b) SEM image showing HAR pyrolyzed electrodes arrays (12:1), the thin pillars are 4x4 μm^2, the height is 50 μm and the gap between large and thin electrodes less than 15 μm, also it shows high resolution and smoothness of the electrodes.

taken in the same scale, shows the variation of the same structures dimensions and shape before and after pyrolysis. Although the shrinkage effect is not controllable, but HAR structures can shrink to up 75% with the shape being preserved. This effect is well known in C-MEMS field as shrinkage effect [92]. The shrinkage seems to be isometric in areas away from the interface between SU-8 and substrate due to the good adhesion between both materials. However this adhesion affect the wall profile and ends up with smooth curved walls.

After crosslinking SU-8, unreacted percentage of monomers and solvent remains inside SU-8 polymer structure. Typically these monomers and solvent have chemical bonds between atoms (C-H, C-C, C-O, Si-H, Si-C), these bonds have certain energies, strengths, and bond lengths. When the polymer is subjected to high thermal energy (heat) and this energy exceeds their bond energy, then it will result in decomposition and Chain Scission of the polymer chains. During this reaction the hydrogen molecules from the forming gas, absorb the oxygen from the polymers forming water molecule (H_2O) which evaporates immediately due to high temperature in the oven. Consequently this

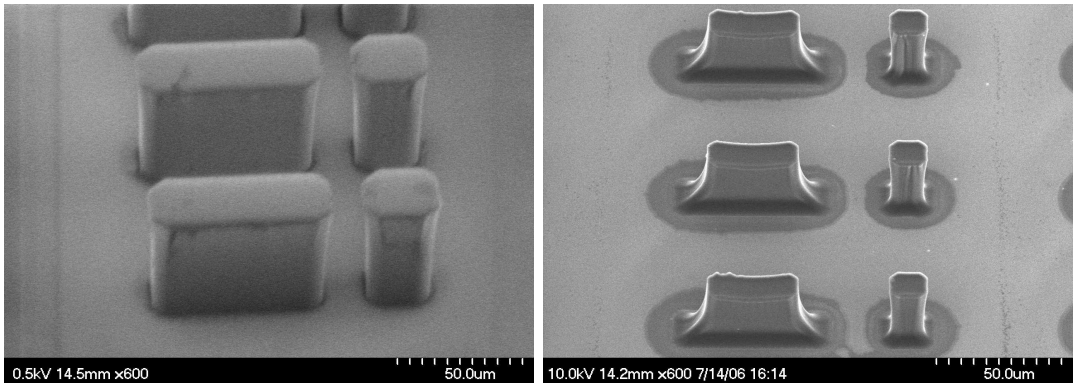

(a) Before pyrolysis (b) After pyrolysis

FIGURE 7.24: The Shrinkage effect on the pillars. On the left the SU-8 pillars before pyrolysis step. On the right the same pillars after pyrolysis process, the pillars shrunk with more than 50%.

change in physical properties results into polymer shrinkage which makes the over all structure to shrink.

7.6.2 Final Device

A full set of the connectors/asymmetric electrodes and the 3D electrodes were fabricated successfully using SU-8. With the aid of clear carbon alignment marks at this stage, high accuracy alignment was archived, where the HAR electrodes are superposed on top of planar electrodes with high precision. The presence of the planar electrodes on the bottom, insure the good adhesion for the HAR 3D-electrodes, and therefore they help to prevent pillars collapsing. The full set of electrode were than pyrolyzed using standard parameters discussed previously, and the final structure is shown in Figure 7.25.

The full set of the electrodes seem to have uniform pillars height which can be seen throughout all the structure. This confirms that the shrinkage effect is isotropic. The dimensions of HAR pillars were downsized in the 3 axes (X, Y, and Z), and the expected electrodes dimensions were obtained with their preserved original shapes and geometries (squares and rectangular) before pyrolysis.

The final dimensions of the pillars are controllable, in Figure 7.25, in order to achieve finale Carbon electrodes with 50 μm thick the SU-8 pillars hight has to be around 150

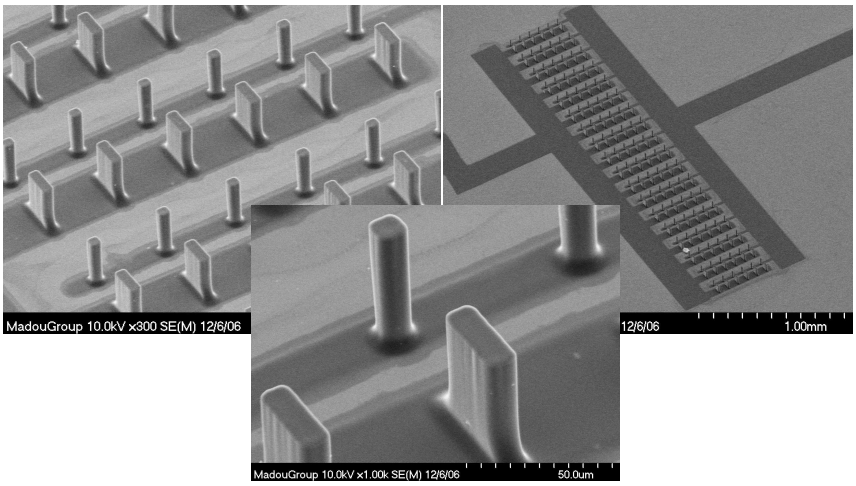

FIGURE 7.25: Final Electrodes configuration, combines planar electrodes and high-aspect-ratio conductive pillars on the top, a good uniformity, resolution and verticality were achieved.

μm. In contrast to the gaps, which are limited with a minimum gap and this gap will increase during pyrolysis. For example a gap of 10 μm will become 15 μm after pyrolysis. In order to obtain a final HAR carbon structure with 10 μm gap, the initial gap has to be below 7.5 μm, which almost impossible to achieve with standard equipments according to the anther experience. Although, an increase in gaps and spaces between pillars, can be clearly seen in the final structure, but they remain homogeneous all over the structure. High resolution of the structure can also noticed with high walls smoothness that were obtained.

7.7 Electrical inspection

After the pyrolysis step and before encapsulating the electrodes in fluidic channel, an electric inspection was performed by measuring the resistance between the wide and the narrow electrodes. Theoretically the value should be a very large value (out of range), however it was found to be between few kΩ to few MΩ as shown by the bar chart Figure 7.26. The short circuit between the electrodes was due to the remained SU-8 residue between the narrow and wide electrodes which was pyrolyzed also and introduced a short circuit(see Figure 7.27). This remained traces of SU-8 could not be

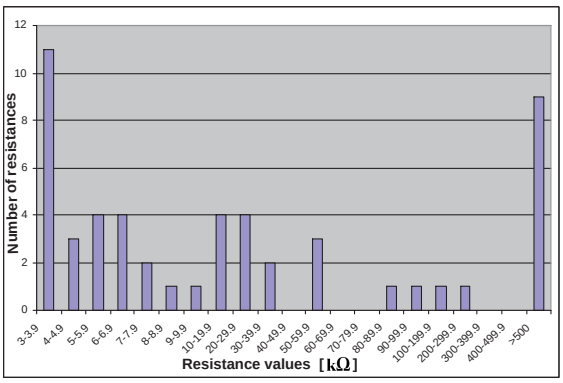

FIGURE 7.26: Percentage of the devices resistance after pyrolysis

prevented either by increasing the developing time as the planar electrodes are subjected to cracks, or by just rinsing the wafer with SU-8 developer.

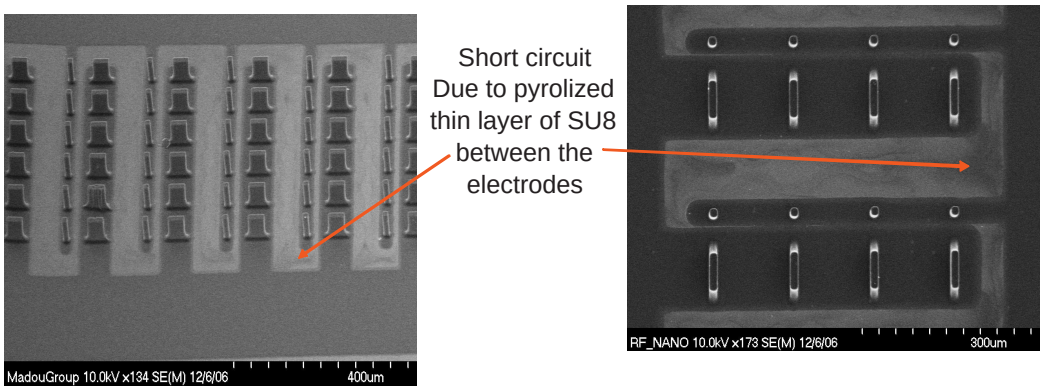

FIGURE 7.27: Visible conductive thin layer between the electrodes

This residue layer can be visible only after pyrolysis step, and only for some wafers (7.27). This thin SU-8 layer was absorbed by the oxide layer which acts as a sponge. It is possible that the carbon contaminated the furnace re-deposited a thin layer of carbon between the electrodes during the pyrolysis process. This thin carbon layer was reduced or removed using dry etch employing a slow O_2 plasma etch. Table 7.2 shows the variation of the short circuit resistance between the electrodes before and after the exposure to O_2 Plasma etch. The large resistances ($\geq$ 200 kΩ) are easy to remove by O_2 Plasma etch and results to an open circuit device (open circuit is assumed to be a resistance of more than 2 MΩ).

Before O_2 Plasma etch	After O_2 Plasma etch
13.8 kΩ	29.8 kΩ
55.3 kΩ	83.8 kΩ
87.6 kΩ	173.1 kΩ
227 kΩ	2.2 MΩ
511 kΩ	2.2 MΩ
1.1 MΩ	2.2 MΩ
2 MΩ	2.2 MΩ

TABLE 7.2: Variation of the resistance between the electrodes before and after the exposure to O_2 Plasma etch.

Although this step is unavoidable, but also has a roughening effect on the electrodes' surface, which may affect the fluid flow velocity [135].

7.7.1 Channel

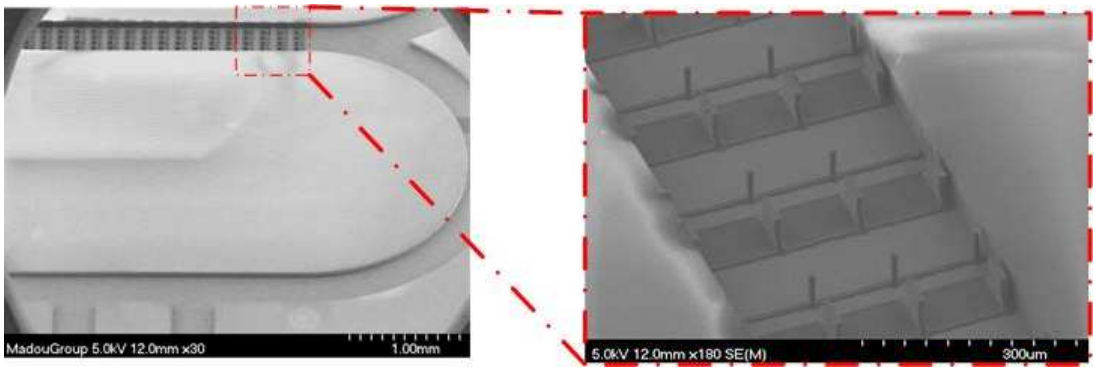

FIGURE 7.28: Fully fabricated a novel 3D AC-electroosmosis micropump, including, planar electrodes, high aspect-ratio conductive pillars and fluidic channel. The full device was made only SU-8 photoresist.

The last stage in the device fabrication is the fabrication of the microfluidic channel. An oval channel with a width of 500 μm and 50 μm in thickness which circumvents the pillars. A layer of SU-8 25 was spun in two steps, at 500rpm for 10 sec followed by 1250 rpm for 35 sec with an acceleration of 310 rpm/sec, than was baked for 20 min at 95^{o}C. Afterward, it was exposed to 20mW/cm^2 of UV light, followed by post exposure baked for 5 min. Finally, the SU-8 layer was developed. Usually fluidic channels are made manually using PDMS, or PMMA, [89, 119] due to their fabrication simplicity. However due to the small nature of the structures, alignment was required and, hence the

photolithography was involved. The use of SU-8 photoresist to make a channel instead of PDMS or PMMA because it is characterized with high fidelity and preserve the shape of the channel.The choice of the SU-8 25 is due to its low viscousity in comparison to SU-8 50, and it can reach thickness of more than 50 μm. Where the structure risks to be peeled-off by spinning high viscous resists.

The final shape of the device is illustrated by Figure 7.28, the HAR 3D carbon electrodes were robust enough which can withstand this fabrication step without breaking, bending, or peeling off as is shown in Figure 7.28.

Chapter 8

Fluid flow induced by nonuniform AC-electric field

In this chapter experimental tests on C-MEMS made fluidic micropump were carried out. The devices were first prepared and encapsulated before performing the characterization. In order to characterize the micropump, a home-made setup was configured for visualization and measurements, which is also highlighted in this chapter. Fluid flow generation based on AC-electroosmosis mechanism using carbon electrodes is introduced in this chapter. Tests and comparison between both planar and 3D structures are also presented. Finally The AC-electroosmosis flow on carbon electrodes was characterized, the fluid flow measurements were performed on different geometries, conductivities and beads sizes.

8.1 Devices Preparation and packaging

8.1.1 Devices dicing

After the electrodes were encapsulated in fluidic channel, dicing process was accomplished by using $K\&S$ 775 mechanical Dicing Saw. To prevent devices breaking, and to keep the inside of the channels clean from any debris during dicing process, 2 μm thick layer of Shipley 1818 positive photoresist (from Shipley Co., Inc) was spun on top of the device, and the bottom side was covered by a thin layer of dicing tape. Shipley photoresist was preferred to cover the channel and electrodes instead of the dicing tape, in order to avoid any electrodes lifting off upon removing the tape. Each wafer was diced into 12 devices with 20mm X 20mm sizes. At the end of the process, the tape was peeled off, and the devices were washed with Acetone in order to remove Shipley photoresist, then were dried up with air nitrogen.

8.1.2 Packaging

Initially the device was designed to be tested in a home-made device holder, as it is depicted in Figure 8.1. The device holder is an interface that connects the device to the external environment. It contains of fluidic connections that are designed to inject beads and fluids into the microchannel. It consists also of electric connectors that are used to link the device with any external electric source. It incorporates also a visualization access, that allows the access for any microscope monitoring.

The chip holder was designed to deal with transparent glass. But when it comes to silicon wafers as substrate, it will be impossible to align the chip inlets and outlets into the right positions. Also, using external electrical connectors harms and breaks the pads of the chip as they are made out of carbon. Alternatively many approaches were tried instead to seal and pack the device. Mainly, by sealing SU-8 channel with PDMS, however, PDMS did not bond to SU-8. Also bonding a uncrosslinked SU-8 to a crosslinked SU-8 channel shows partial success. Although uncrosslinked SU-8 is very adhesive material and bonds easily to the channel layer, but the device was suffering

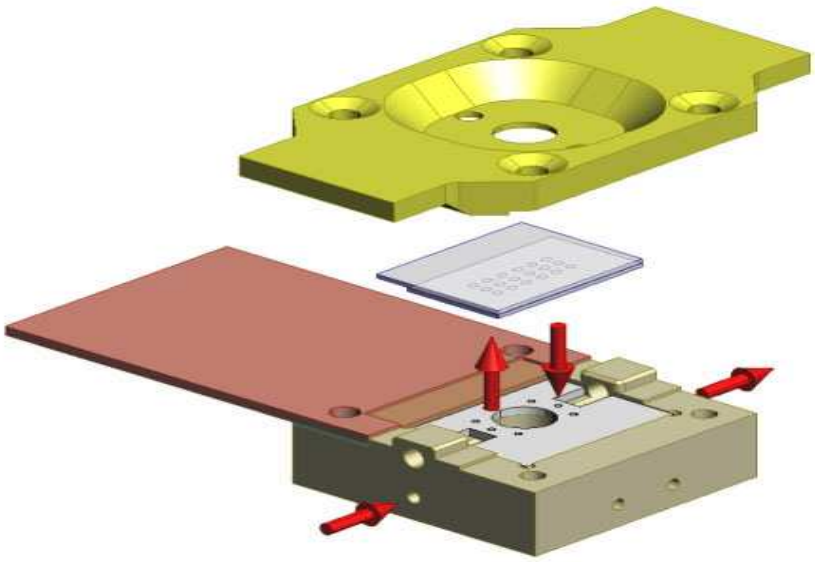

FIGURE 8.1: Device holder which consists of 4 layers, bottom bulky layer that is used for fluidic connections (with inlets and outlets as it is illustrated with the red arrows), a gasket which comes between the device and the bottom layer in order to eliminate any fluidic leakage. Electrical connections layer which comes in direct contact with the electrical pads of the device, a top layer with four holes on the sides for screws in order to tight up both top and bottom layers together, and a large middle hole to allow microscopic visualization.

from leakage. Using uncrosslinked SU-8 may conduct also the channel to be blocked up by SU-8 during baking step upon bonding process.

Since the life time of the device was very limited (will be explained more in details later in this chapter), and due to previous constrains, the packaging process was simplified in order to perform the fluid flow measurements. Therefore, the device was sandwiched between two microscopic glass slides, using strong double sided scotch. For more strong bonding, clippers were mounted on the optical microscope stage on both sides of the device for more firm holding.

8.1.3 Wiring and external electrical connections

The device Carbon pads were around 5 μm thick, in order to connect them to an external electric source, electrical crocodile clippers were used, yet the carbon pads were too fragile to withstand to the clippers gripping. Soldering was not promising option as

the brazing filler metal does not stick easily to thin carbon layer. Alternatively using silver conductive glue with silver nano-particles was the best solution to connect the external electrical connection. Due to the fragility of the electrodes, 1mm diameter electrical wires were used in order to secure the pads from lifting off from the substrate, as they have low stiffness coefficient.

8.2 Experimental material and methods

8.2.1 Stock solutions

In these experiments, ionic solutions with different conductivities were prepared. At first, a single tablet of Phosphate Buffered Saline (PBS) from Oxoid (Unipath Ltd., Basingstoke, UK) was dissolved in 100 ml of DI water for 10 min. The electrical conductivity of the solution was then measured using EC 215 Conductivity meter (from Hanna Instrument with accuracy 0.1%) to be found 1.6 S/m as it was indicated by the manufacturer. Then, DI water was added to the solution to dilute it until 1 S/m conductivity was reached. Afterwards, the latter solution was diluted 10, 100, and 1000 times with DI, resulting to 100 mS/m, 10 mS/m and 1 mS/m solution conductivities respectively with a pH of 7.4. PBS was preffered in these experiments, as it contains both NaCl and KCl salts, these salts that contains Na^+, K^+, Cl^- ions which are suitable for electroosmosis pumping testes, as they form the electrical double layer.

8.2.2 Beads

Both fluorescent polymer microspheres and micro and latex nanoparticles were used as flow tracing devices, Polystyrene beads crosslinked (from Duke Scientific Corporation), with density 1.05 g/cm3, in mean diameters between 0.03 to 8 μm packaged as 10% solids in water were purchased from Duke Scientific Corporation. Before using the beads, they have to be washed twice in the appropriate conductivity solution and finally resuspended, and then were mixed in the sonicator for 5 minutes. All bead solutions were refrigerated and used within one month.

8.3 Test Setup

A home-made setup was assembled and configured as it can be seen in Figure 8.3. This home-made setup runs on the top of an anti-vibration table.

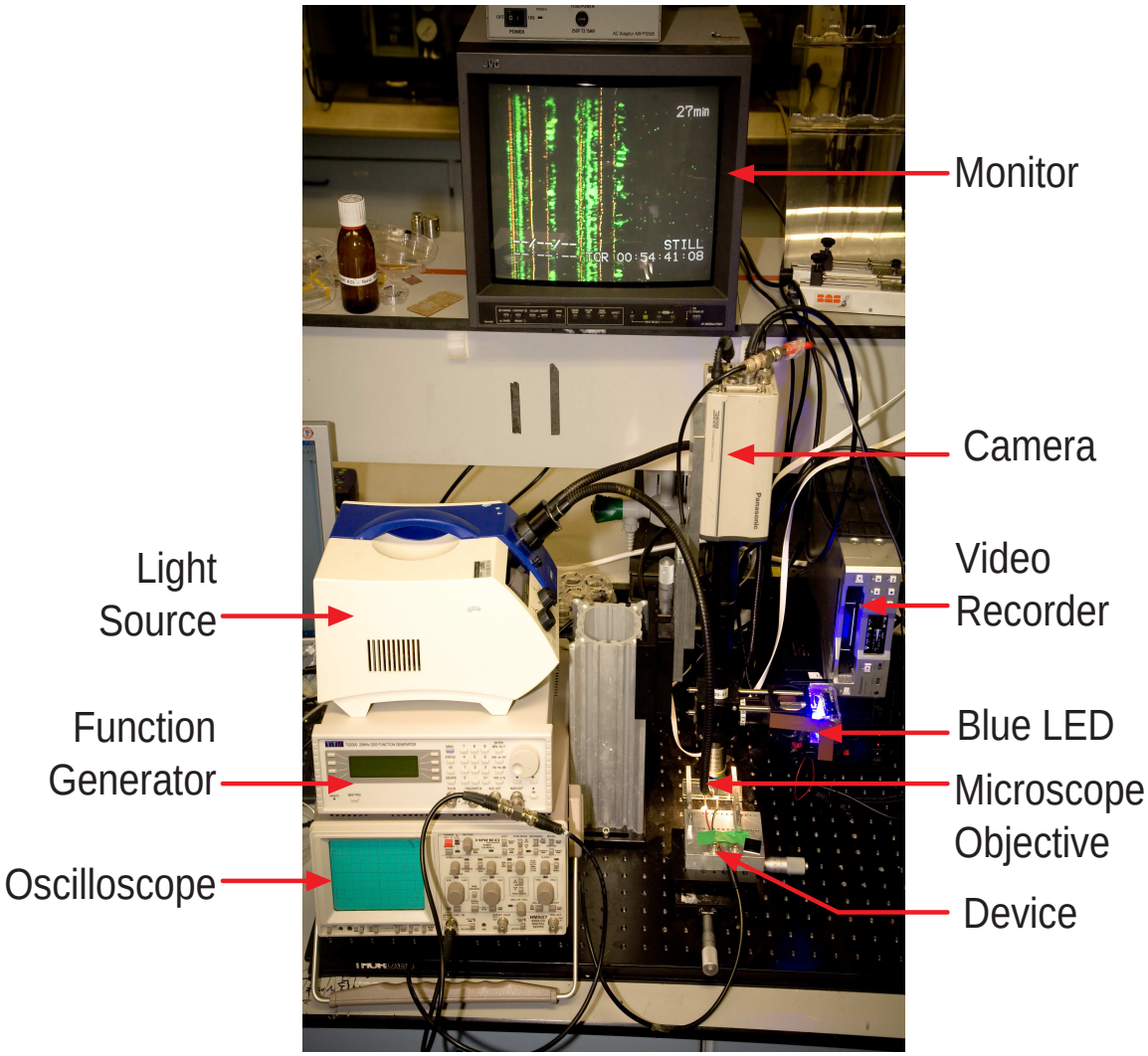

FIGURE 8.2: Illustrates the home-configured experimental setup that is used during the tests. It consists from a device holder, the electrical excitation systems (function generator and the oscilloscope), optical system (Microscopic objective and light sources), and measurements and monitoring systems (Camera, video recorder, and monitor).

It consists mainly of:

- A device holder attached to an XY micro-positioning stage in order to move the device in XY direction.

- An electrical excitation function generator that is connected to an oscilloscope to monitor the output electrical signal,
- Optical system that consists from the main objective, optical filters and light sources (Bleu LED + white light),
- The visualization and measurement system which consists from the camera, monitor and the video recorder.

8.3.1 Optics

The device were observed under customized optical setup, the upright lens is Nikon Japan Plan Fluor, with 10 X magnification and Numerical Aperture N.A. 0.30, DIC differential interference contrast (DIC), Type of Prism L/N1.

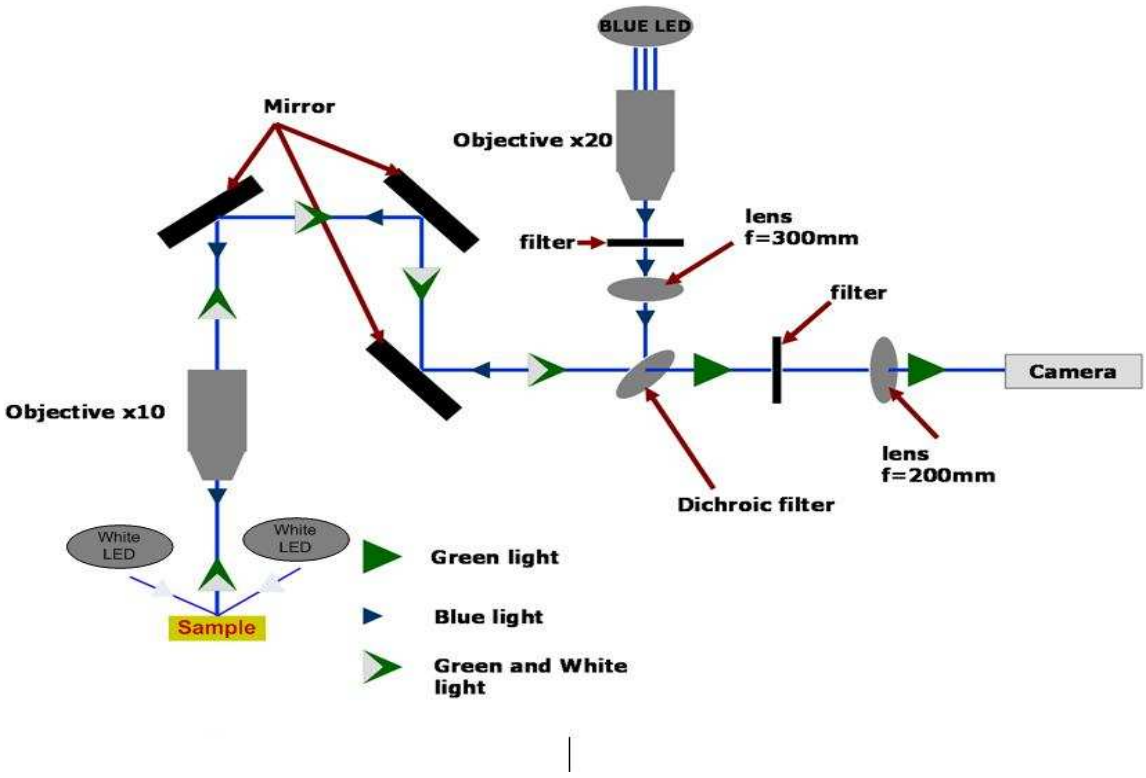

FIGURE 8.3: The optical system used to monitor fluorescence particles based on blue light excitation. The incident blue light is generated by the blue LED and amplified and guided toward the fluoresces beads, where the reflected light consists of blue, green and white signal are filtered where only the green light can pass through to the camera.

Using blue LEDs (LUXEON V STAR BLUE- from FARNELL) with 16.0 mm a working distance objectives. The videos and images could be captured using Panasonic 3CCD digital convertible video camera and Panasonic AGDV2500 digital video recorder.

8.3.2 Electrical excitation

An electric AC-signal of up to 40 MHz and 20 V_{pp} was generated by TTI "TGA1244", a four channel Arbitrary Waveform Generator (from Test Equipment Solutions). The signal was applied directly in contact with the external pads at the edge of the device. Agilent 54641D Mixed Signal Oscilloscope (Mega Zoom 350 MHz 2GSa/s), was connected to the signal generator to double-check the waveform frequency and the amplitude produced.

8.3.3 Fluid Flow velocity measurements

The motion of the particles along the microchannel was viewed by the optical microscope through the glass. The video images of the particles velocities and trajectories were captured using a high speed CCD camera, and recorded using a video cassette recorder. Video recording subsequently was transferred and digitized to JPEG or AVI format with Adobe Premier video capture software. The same software was used for analysis of particles trajectories and velocities using frame by frame option.

8.4 Producing fluid flow using C-MEMS electrodes

First use of the Carbon-MEMS electrodes was applied in micro batteries applications, but were never tested on fluidic applications. The aim of these experiments is to prove the functionality of the carbon electrodes for generating fluid flow. To simplify the experiments, a free of channel set of asymmetric planar electrodes were employed, the dimensions of the electrodes were 20 μm and 100 μm gaps, and their thickness was 5 μm. In these tests 8 μm latex beads diluted in low conductive medium were used as fluid flow tracers.

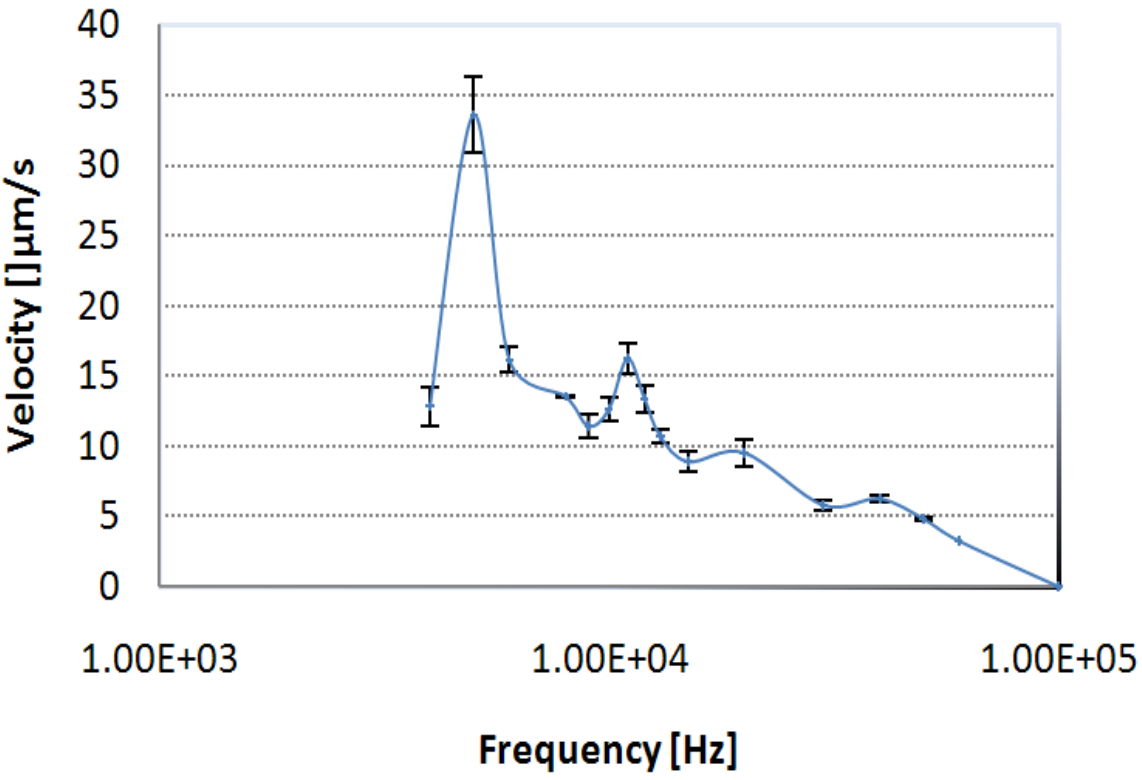

FIGURE 8.4: Fluid flow velocity measurements versus the variation in frequency of free of channel asymmetric planar carbon electrodes with 20 μm and 100 μm gaps, the applied voltage fixed at 16 V_{pp} and 8 μm latex tracer particles at low conductive medium were used.

The latex beads were injected on the top of the planar electrodes using micropipette. For good microscopic observation a glass cover slip was put on the top of electrodes

array. The applied AC-electric potential was fixed at 16 V_{pp}, and the frequency was varied to up to 10 MHz.

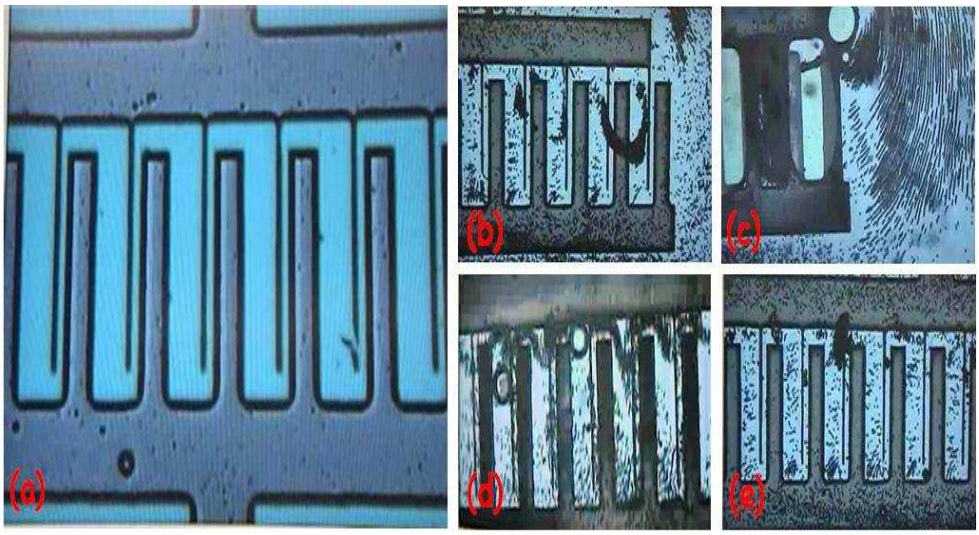

FIGURE 8.5: Fluid flow test using 8 μm latex beads on asymmetric electrodes with 100 μm large electrodes/ gaps and 20 μm for the small electrodes/ gaps . (a) Empty planar electrodes (before the injection of latex beads). (b, c, d, and e) Show different effects occurring on the top of planar electrodes while the frequency was varied, where (b) shows a mass transportation of latex beads on the top electrodes, (c) shows bubbles generation and uniform distribution of latex beads at the exit of the array, (d) shows the motion of the beads at the ends of the large electrodes, and (e) the beads were trapped mostly at the end of the thinner electrodes and beginning of the large ones.

By tracking latex beads, the experiments have shown that a steady motion of the beads can be seen on top of carbon electrodes. The graph in Figure 8.4 shows that the high fluid flow velocity was achieved is in the range of 5 kHz, as the frequency increases the fluid flow velocity decreases gradually. Similar experiments were conducted on a free of channel 3D electrodes array of 50 μm high pillars with an aspect ratio of 7:1, a maximum fluid flow velocity achieved was 120 μm/s.

In these experiments, the motion of latex beads on on top of carbon electrodes can not necessarily prove that the generated fluid motion is an AC-electroosmosis pumping. This is because other effects were observed occurring concurrently with the fluid motion. These effects can be seen in Figure 8.5, which are mainly a mass transportation of the beads on the top of the electrodes (b), bubbles generation (c), motion of the beads at the end of large electrodes (d), and trapping of the beads between the end of the

thinner electrodes and the beginning of the large electrodes (e). In order to decouple different effects occurring at the same time as the AC-electroosmosis pumping, therefore few limitations were taking in consideration.

8.5 System characterisation and effects decoupling

The AC-electroosmosis pumping is not related directly only to the applied electric signal (frequency and amplitude) or to the electrodes geometry, but also to the positioning of the electrodes in the channel, conductivity of the medium used, and the type of tracer particles used. Therefore it is necessarily to optimize these factors. Besides these factors, there are other factors which may affect the particles and the fluid medium. However, there is almost no control on these particular effects. These phenomena are mainly, the gravity, Brownian motion, buoyancy, and natural convection. However, these effects will be neglected at some extent.

8.5.1 Minimization of DEP effect

Previously 8 μm latex beads were use as tracking particles. Theses particles are made from dielectric material. This material can be subjected to the dielectrophoresis force (DEP), which is distinctly different in nature from electroosmosis. DEP is defined as the translational motion of neutral matter as a result of polarisation effects in electric fields [26, 85]. Under the influence of non uniform electric field, these neutral particles will always move toward the high or low field regions. The DEP is a controllable effect, which is dependent to the frequency, medium and particles size. According to equation 8.1 the size of the particle is proportional to the DEP force. Consequently, by reducing the particles size, the DEP force will be then reduced.

$$\langle F \rangle = \pi \epsilon_m a^3 Ref_{CM} \nabla |E|^2 \tag{8.1}$$

where $\nabla |E|^2$ is the gradient of the square of the electric field and Ref_{CM} is the real part of the Clausius-Mossotti factor, which is defined by the limit $-0.5 < Ref_{CM} < 1$.

Therefore, by using nano-particles, will definitely reduce the DEP force on the particles, which may affect the electroosmosis flow. In addition to the DEP minimization, nanoparticles can be easily refine the visualization and help to show the fluid motion in details such as fluidic vortices around the edges.

8.5.2 Electrothermal effect

Due to the small size of the electrodes the application of relatively low voltages can produce very high electrical field strengths (in the order of $10^6 V/m$). These high field strengths can generate a large power dissipation in the fluid surrounding the electrodes. The power generated per unit volume is proportional to the conductivity of the medium σ_m and the magnitude of the electric field E squared and is expressed as:

$$W = \sigma_m E^2 \tag{8.2}$$

The electrical power density can be highly non-uniform due to the non-uniform fields produced by microelectrodes, with the highest power density localised at and close to the electrodes. This results in the formation of temperature gradients in the fluid, leading to gradients in viscosity, density, permittivity and conductivity of the fluid. These gradients can give rise to fluid flow in two ways, natural convection and electrothermal fluid flow. Consequently, in order to reduce the electrothermal force, the conductivity of the KCl medium was kept as low as 14.5 $\mu S/cm$.

8.5.3 Minimization of Ends effect

In this context the ends effect is defined as the natural formation of horizontal vortices at the ends of the arrays (see Figure 8.6), this effect is due to the distortion of the electric field around and at the end of the large electrode. This effect is not well understood, but it can be interpreted as the distortion of the electric field at this area since the thinner electrode's region is characterized with high electric field zone. This effect may disturb and reduce the pumping efficiency. This effect is inevitable and may not be totally eliminated, but it can be reduced experimentally. In oder to reduce this effect, the electrodes' ends were covered by the fluidic channel walls in order to keep the fluid away from the distorted electric field region.

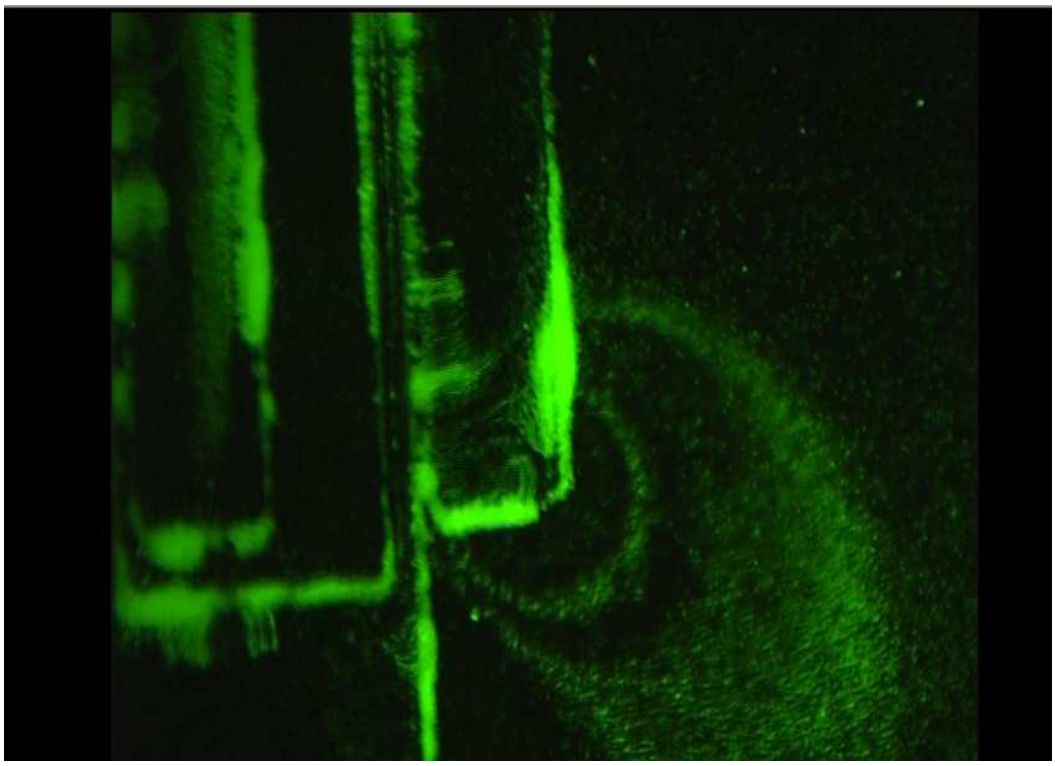

FIGURE 8.6: Illustrates ends effect, where large population of fluorescence beads accumulate around the end of the large electrode and rotate horizontally (parallel to the planar electrode) resulting in vortices.

8.5.4 Minimization of bubbles generation

Micro-bubbles were found to be generated at low frequencies below 100 Hz. Bubbles disturb the pumping efficiency and obstruct the flow as they increase the flow resistance in the microchannel [11], and contribute in delaminating the planar electrodes from the wafer. In order to prevent bubbles generation, 100 Hz was set to be the minimum applied frequency.

8.6 AC-electroosmosis fluid flow

In these experiments 500nm and 1000 nm, fluorescent Molecular Probes (Eugene, OR) latex spheres particles were used. The use of nano-particles minimize the DEP force during the pumping. Also the use of the fluorescent microspheres is to trace the fluid behaviour and help to visualize pumping effect during the experiment. The particles were carboxylate-modified latex spheres, hence, these spheres had a net negative charge. The particles were suspended in 1 mM and 100 μM conductive mediums of KCl. The conductivity of the medium was measured with conductivity meter (EC215 from Hanna Instruments and was found to be 148 $\mu S/cm$ and 19 $\mu S/cm$ respectively for 1mM and 100 μM. Low concentration mediums were preferred in order to prevent any electrothermal pumping to occur. The end edges of the electrodes were covered by the channel walls to reduce the ends effect.

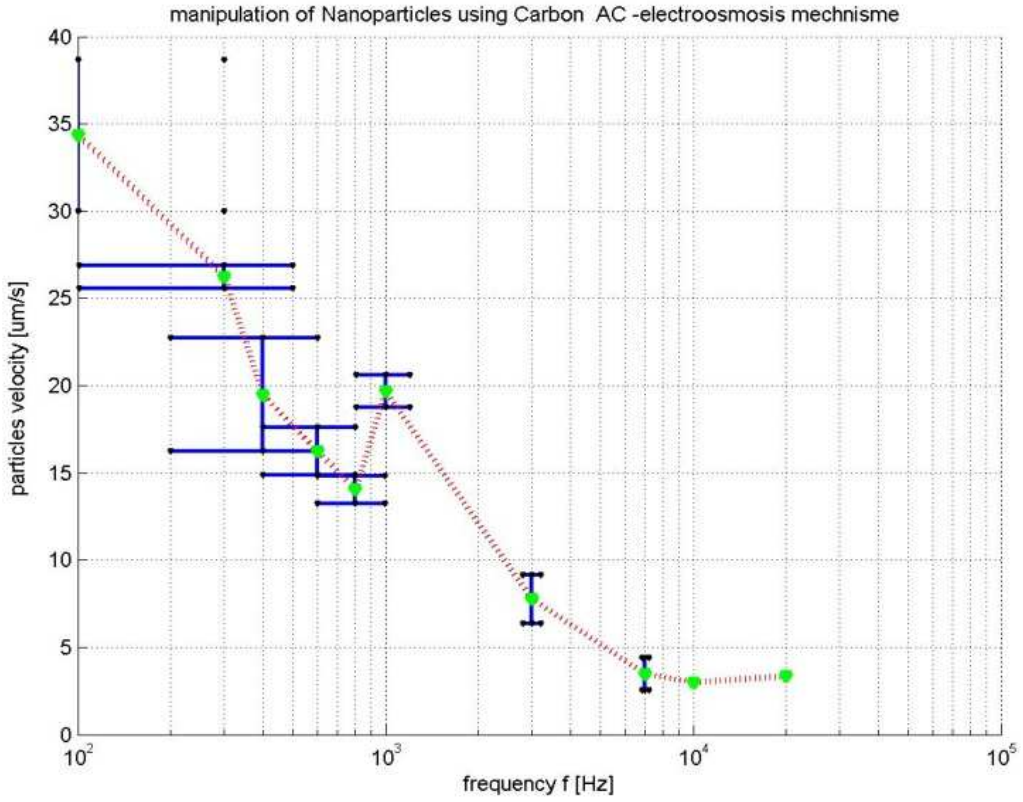

FIGURE 8.7: AC-electroosmosis fluid flow velocity as function of frequency, the measurements were taken C-MEMS planar electrodes using 500 nm fluorescence particles

When 20 V_{pp} voltage was applied, the fluorescence spheres were observed to move inside the channel as results of the fluid motion. The generated fluid motion was steady and moving in one direction. The fluid flow velocity was frequency dependent as it can be seen in Figure 8.7. Unlike in previous tests using 8 μm latex beads, the fluid flow using nanoparticles was occurring at low frequencies between 100 Hz and 200 Hz. Pumping frequency dependency characterization will be discussed later.

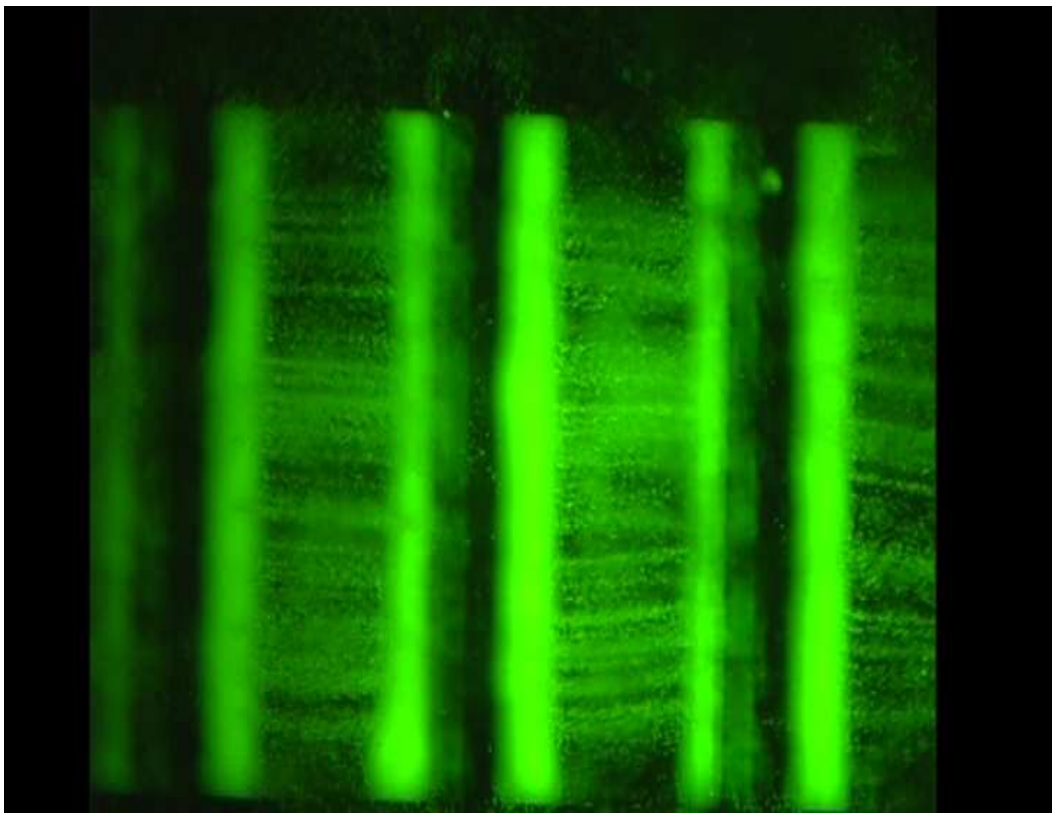

FIGURE 8.8: Tracking fluid flow motion generated by C-MEMS made electrodes using 500 nm fluorescence particles, a steady and uniform fluid flow stream can clearly be seen on top of the electrodes inside 500 μm wide fluidic channel.

On the of top of the carbon electrodes, fluorescence particles were observed to move away from the small electrodes over the small gap across the large electrode in a periodical manner. The beads were traveling from the thin electrode to the large one in different levels. This can be seen clearly in Figure 8.8, where the fluorescence beads seem to travel just over the large gap between the electrodes. The motion of the beads over the small gaps was out of focus, which illustrates that the trajectory of the fluid over

the electrodes was not linear. It can also be noticed from Figure 8.8 that an intensive population of fluorescence beads were presented on the top of the electrodes. This is not only due to the particles trapping, but in addition is due to the generation of rolling motion of the fluid that is generated at every electrodes edge. Large rolls can be seen at the edges of large electrodes (where there is a high contrast of fluorescence beads), and small rolls over the edges of the small electrodes (low contrast of fluorescence beads).

Despite these rolls may increase the longitudinal diffusion with respect to the flow direction, it is noted by Debesset et al. [35] that the rolls may cause a dramatic drop in the net flow. Bazant et al. [8] developed a 3D stepped electrodes model to reduce the drawback effects of these rolls. This model has shown an improvement in the flow velocity at some extent. On the other side the generated fluid rolls are considered as the motors which drive the flow inside the channel. By increasing the number of these rolls along the channel, the fluid flow will increase, the new designed micropump with 3D-HAR will fit in this category.

According to Debesset et al. [35] that the dimension of the vortices to be of the order of the electrodes sizes. This is in agreement with the experimental rolls sizes that are generated around the carbon electrodes.

According to Ramos et al. [97], the rolls over the small electrode are of similar size, moving in opposite direction, and, therefore, do not contribute substantially, to the global directional fluid flow. The rolls over the big electrode are more asymmetric, with the higher velocity occurring at the edge closest to the small electrode. The fluid moves outwards from the inner edge of the large electrode, then up and over the outer edge and the small electrode, and then down towards the next large electrode. This results in a directional flow along the electrode array as seen in the experiment. These rolls responsible for driving the fluid are mainly generated by the electric field.

When the alternating potential difference is applied to each pair of the asymmetric 3D-planar electrodes, a nonuniform electric field will be created. The electric field generated by the electrodes has two components normal and tangential. The component of the field normal to the electrode induces a charge in the diffuse double layer; where the

tangential component of the field produces a force on the induced charge in the opposite electrode. It is mentioned by Ramos et al. [97] that the double layer accumulates electrical energy as a capacitor; the normal current to the interface charging the double layer. It is expected that the normal current to the interface and the electrical energy stored in the double layer are more uniform along the small electrode than along the large electrode, since they are distributed over a shorter distance. As results the rolls are symmetrical around the small electrode edges and asymmetrical around the edges of the large one. This also can be seen from an other perspective, according to Ramos's et al. [99] electrical model, the AC-electroosmosis mechanism can be represented by RC circuit, where the electrical double layer represents the capacitors and the fluid represents the current tube resistors of a varying length through the bulk solution. Because the resistance is smaller (where the field is strong) adjacent to the gap, the inner capacitors of the electrical double layer on top of the electrodes charge faster than the outer capacitors. This uneven charges distribution on top of the electrodes leads to the generation of the fluidic rolls.

The force has a nonzero time average because if the sign of the field reverses, so does the sign of the charge. This means that the direction of the fluid flow does not change with the potential switch, because the ions are switched also. This force produces the electroosmotic slip velocity, which consists of an oscillatory and a nonzero time-averaged component. The arrangement of a single pair of the 3D-planar asymmetric electrodes produces a non-symmetric local flow (in contrary to symmetric electrodes which generates symmetrical local flow). Ultimately by using an array of electrodes, generates a global flow around the channel in the direction of broken symmetry. For frequencies in range of 100 Hz to 10 kHZ, it is the time-averaged velocity that is observed and gives rise to the observed fluid flow.

8.7 Characterization of 3D ACEO-micropumps made from C-MEMS

In the following experiments, the fluid flow velocity for both ACEO pumps with 3D-planar and 3D-HAR Carbon MEMS electrodes is compared. The fluid flow velocity was measured as a function of conductivity, voltage and frequency.

8.7.1 Effect of the SU-8 layer resistance on pumping efficiency

Due some fabrication limitations discussed previously a resistive thin carbon layer formed between the electrodes. Although O_2 plasma etch shows some success to reduce the electrical resistivity of this layer, but can not be totally removed in most cases. This layer makes an additional large electric resistance (may vary between few kΩ to the order of MΩ) between the electrodes. Since the AC-electroosmosis mechanism can initially be described by an equivalent RC circuit, where the diffuse layers act like capacitors, and the fluid as resistors tubes [99], therefore, it is important to investigate the effect of this short circuit carbon layer (referred as SU-8 resistance) on the pumping performance.

In these experiments, the fluid flow was generated by two different devices with small and large SU-8 resistance. The smallest SU-8 resistance was about 52 kΩ, where the large one was around 2 MΩ. The fluid flow was measured as a function of the voltage, and for 2 different conductivities (10 μM, and 10 mM). At least 3 measurements were taken at each point measured in the experiments.

- Results

The measured graphs are depicted in Figure 8.9, show the fluid flow velocity as a function of voltage variation for two SU-8 resistances and conductivities. For low conductivity (10 μM), both devices behave in the same manner. They experience forward and reverse pumping for the same voltages. The graphs seem almost identical with small changes of about 10% for the large voltages.

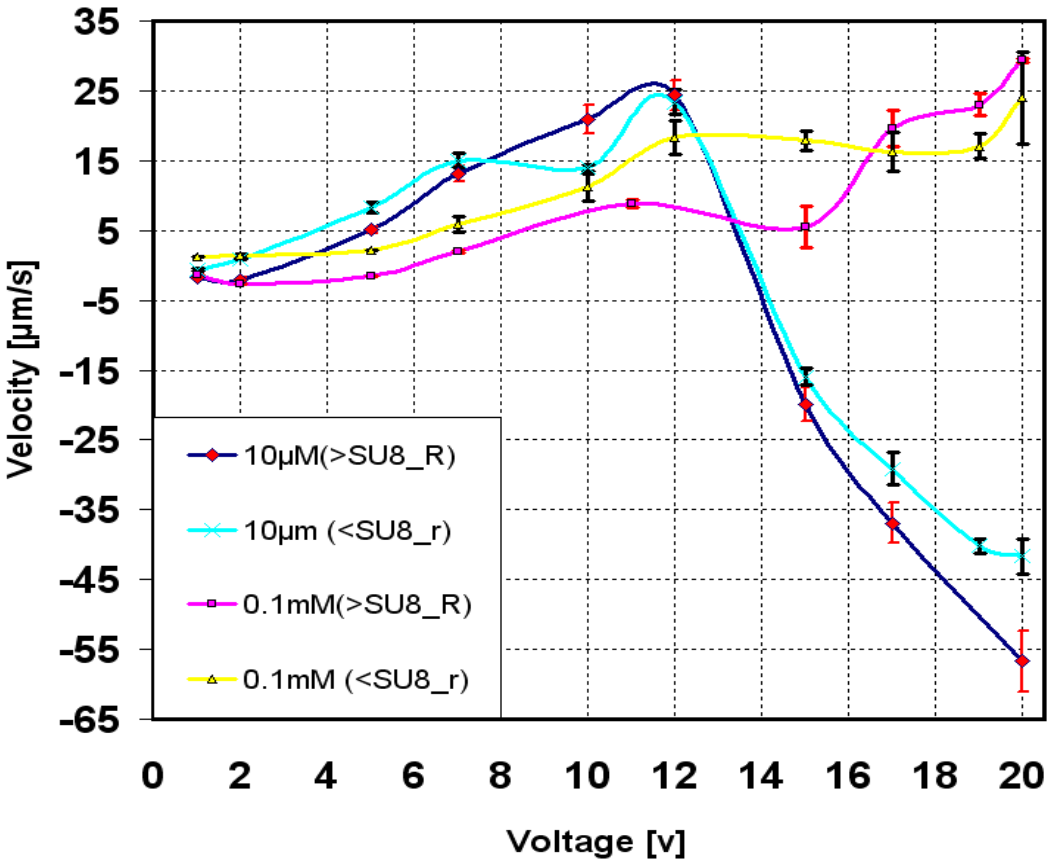

FIGURE 8.9: Fluid flow velocity as a function of the voltage for 3D-planar electrodes structure, for two different medium concentrations (10 μM and 0.1 mM), and two different SU-8 resistance

For higher conductivity (10 mM), although there is some fluctuations for both graphs, but mostly they increase as the voltage increases. From the experiments, it can be seen that both devices behave almost the same (small variations $< 15\%$), therefore this leads to conclude that the SU-8 resistance does not affect the ACEO pumping.

8.7.2 Effect of the voltage on the fluid flow velocity

In these experiments, two types of AC-electroosmosis micropumps with different electrodes structures were tested. The first type 3D-planar asymmetric C-MEMS made electrodes were used to generate fluid flow, whereas in the second model in addition to the 3D-planar electrodes as baseline case for the new design, 3D-HAR electrodes were also involved. The electrodes dimensions may vary after pyrolysis due to shrinkage effect.

Therefore, for consistent measurements and reliable comparison, the electrodes dimensions were measured and chosen to be roughly the same after pyrolysis. The dimensions of planar electrodes were approximately about 60 μm $\pm 5\mu m$ for large electrodes, and 20 μm $\pm 3\mu m$ for narrow ones. The fluidic channel encountered the electrodes was 500 μm wide and 50 μm high.

The velocity data were presented as a function of the applied potential, and electrolyte concentration. It was measured at a fixed frequency of *f=1 kHz* for 10 values of AC voltages, linearly distributed between 1 V_{pp} and 20 V_{pp}. Since the pumps experience, both forward (positive) and reverse (negative) flow pumping, the positive direction is assigned from the small electrode to narrow gap to the large electrode toward the large gap direction. In these experiments, each micropump characterized was operating for at least two hours continuously.

8.7.2.1 3D planar electrodes

For the lowest conductive medium with ions concentration of 10 μM and small applied voltages ($< 3V_{pp}$), a slight reverse pumping was occurring. Increasing the voltage, leads the fluid flow velocity to increase to up 13 V_{pp}, where a maximum forward fluid flow velocity 26 $\mu m/s$ was reached. Beyond this point any further increase in voltage leads to a decrease in the flow velocity. By Applying voltages, more than 14 V_{pp} conducts the reverse pumping again to a maximum value of -55 $\mu m/s$ which corresponds to an applied voltage 20 V_{pp}. For higher conductivity medium with concentration of 10 mM, the micropump was also experiencing reverse pumping for small applied voltages below 5 V_{pp}. For such medium conductivity any increase in the applied voltage beyond 5 V_{pp}, leads to an increase in the froward flow velocity. Although fluid flow velocity slope rises slower than in previous medium conductivity, but no reverse pumping can be seen after 5 V_{pp}, where a maximum forward fluid flow velocity of 27 $\mu m/s$ was reached for an applied voltage of 20 V_{pp}.

For higher medium conductivities with concentrations of 1 mM and 10 mM, no fluid flow velocity can be seen for a range of the applied voltages between 1-20 V_{pp}.

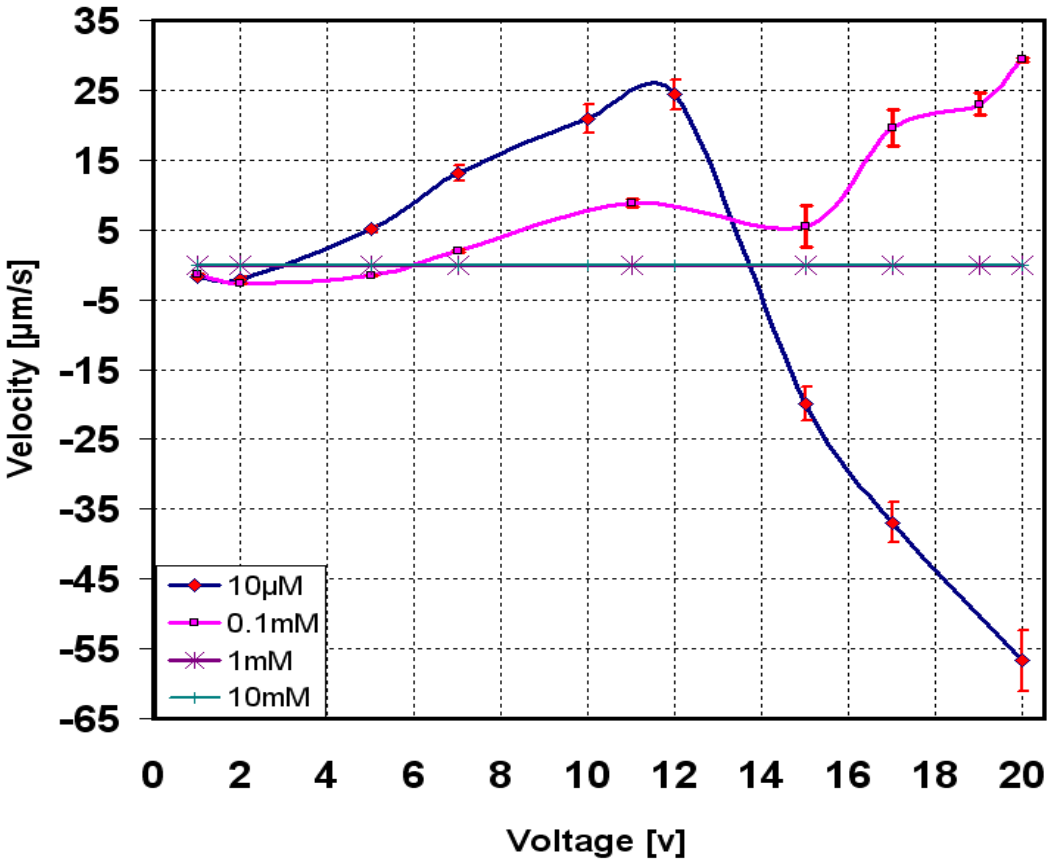

FIGURE 8.10: Fluid flow velocity versus voltage for 3D-planar electrodes, for different medium concentrations

8.7.2.2 3D HAR electrodes

For the lowest conductive medium (with a concentration of 10 μM), the fluid flow velocity increases exponentially to up to 160 $\mu m/s$, increasing the voltage to 20 V_{pp} resulted to decrease the fluid flow velocity.

Using higher conductive medium with a concentration of 0.1 mM, shows almost similar fluid flow pumping behaviour, with lower magnitude. For applied voltages below 10 V_{pp} the velocity increases slowly, above this voltage, the velocity increases exponentially to approximately 120 $\mu m/s$ and then drops after increasing the voltage to 20 V_{pp}.

For medium concentration of 1 mM, in this case the fluid flow velocity can be driven by 3D HAR electrodes unlike planar ones. Although the fluid flow slope was very slow,

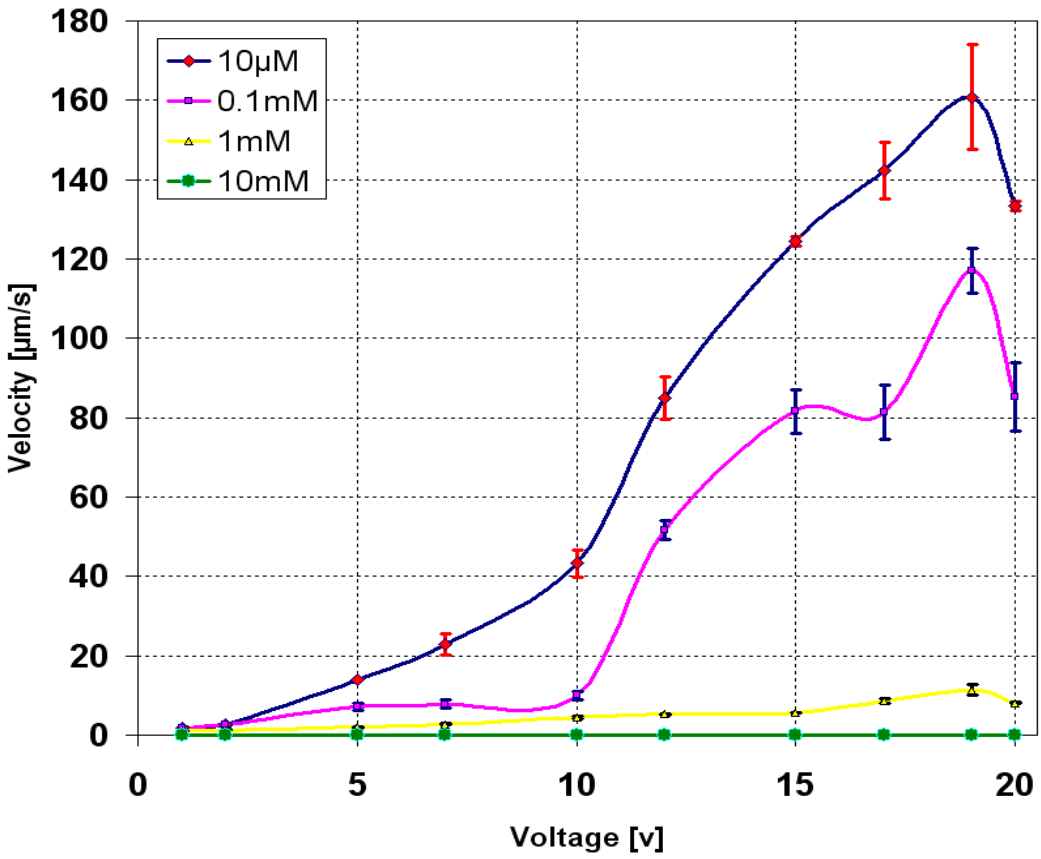

FIGURE 8.11: Fluid flow velocity versus voltage for 3D-HAR electrodes, for different medium concentrations

a maximum velocity, of 10 $\mu m/s$ was achieved at 19 V_{pp}, and then it decreases at 20 V_{pp}.

For the highest medium concentration (10 mM), no fluid flow motion was observed.

- Discussion

Previously the use of elevated AC voltages more than 10 V_{pp}, was a problem for AC-electroosmosis micropumps as it may harm the electrodes. It is reported by Studer et al. [111], by using gold electrodes and applying AC signal above than 4 V_{rms} at a fixed frequency corresponding to 1 kHz, in low conductivity media (1 mM, 0.1 mM), leads to damage the electrodes. However, in the above experiments by using carbon electrodes a maximum voltage of 20 V_{pp} was applied, but no damage on the electrodes was seen.

Moreover, despite the carbon electrodes have limited life time, during the testes, each micropump was running for more than 120 min continuously. This obviously is considered as an advantageous improvement to overcome the short life time of previous meals made devices. It was reported by Debbesset et al. [35], that the life time of the gold electrodes used in their AC-electroosmosis micropump was estimated to be approximately 90 min in similar conditions, where in the case of Studer's device was running for only 30 min.

In most AC-electroosomsis micropump, the electrodes are made out of gold due to its good conductivity and the simplicity in fabrication [35]. However, the corrosion occurs upon applying an electrical potential due to electrolysis effect, and leads to deteriorate the electrodes. The electrolysis enhances the bubbles formation obstructing visualization of the beads during the measurements. Also it contaminates the electrolyte and changing the ionic concentration, due the interchange of electrolyte atoms and ions by the removal or addition of electrons from the electrode. This variation in the electrolyte concentration leads to an inaccurate fluid flow measurements.

To overcome this limitation, some efforts were conducted by other research groups, mainly by covering gold electrodes using protective Titanium layer [99], or by using Indium Tin Oxide (ITO) [86]. However the electrolysis effect remains present with the use of metallic electrodes.

However, electrodes degradation, dissolution, hydrodynamic instability, and sample contamination effects can be reduced by using carbon electrodes as it is chemically resistive material.

With regard to the pumping behaviour, overall the pumping response is not linear to the applied voltages for both 3D-planar and 3D-HAR micropumps. This characteristic, distinguishes the AC-electroosmosis pumps on the DC-electroosmosis ones. The DC-electroosmosis pumps are characterised with linear response to the applied voltage. It is reported by [129], that a DC-electroosmosis, generates just 100 μ/s for an applied voltage of 100 V, and increases linearly with the voltage. Therefore, this requires high applied voltages in order to achieve higher fluid flow velocities.

For AC-electroosmosis, according to Ramos's theory which is based on the capacitive charging of the diffuse layer of the electrical double layer, the velocity $u \propto V^2$, a simplified mathematical model of of AC- electroosmosis flow is given by:

$$\langle u \rangle \propto \frac{\epsilon V^2}{\eta(1+\delta)G\left[\frac{\omega}{\omega_c}+\frac{\omega_c}{\omega}\right]^2} \tag{8.3}$$

where V is the applied voltage, ϵ and η are the permittivity and viscousity of the bulk fluid which are assumed constant. G is the electrode gap, δ is the ratio of the diffuse layer to compact layer, capacitances which are assumed constant also. ω_c, is the characteristic frequency, and is given by:

$$\omega_c \propto \frac{D(1+\delta)}{\lambda G} \tag{8.4}$$

λ is the Debye length of the electrical double layer, and D is the characteristic ionic diffusivity.

Ramos's model was based on the assumption of the applied voltages on the electrical double layer is in the order of $k_BT/e = 25mv$. However, the use of carbon electrodes requires voltages up 20 V_{pp} in order to drive the fluid. As a consequence the induced double-layer voltages should be >>25 mv.

According to Bazant et al. [4], at this stage a variety of new effects could become important, essentially Steric effect of finite molecular kinetics [68, 6], viscoelectric effects, discreet electrostatic correlations, dissociation and de-solvation kinetics,and Faradaic electrochemical reactions. Some theoretical work was connected by the same group, where they found that the fluid flow velocity $u \propto |E|$ (electric field) or $|V|$ (applied potential). However, neither the response of the 3D-planar micropump nor the 3D-HAR to the applied voltages seem to agree with this model. This is probably is due the electrochemical properties of carbon electrodes, to the rough surface of the electrodes, or to the porosity of the electrodes.

With regards to the reverse pumping, was only observed in the 3D-planar structures at low voltages below 5 V_{pp} first and then at high voltages more than 14 V_{pp}. The magnitude of the velocity during reversal pumping is observed to be higher than the peak velocities prior reversal flow .

In comparison to previous work using metallic electrodes [54, 111, 4, 118], reversal pumping was observed only at elevated voltages, but not at low voltages as it is the case for 3D-planar carbon electrodes. Reversal pumping is not a common effect that arises in AC-electroosmosis pumping. It is not well yet fully understood, and was just reported by limited number of research groups [54, 111, 4, 118], and no complete mathematical model was yet been developed. However the obtained experimental results of reversal pumping at high voltages, agreed with the hypothesis that was proposed by Jie-Wu [130]. This hypothesis is based on Faraday's law, and states that there exists two charging mechanism on the electrodes surface, capacitive and Faradaic charging mechanisms. Capacitive charging mechanism is resulted from the electrical double layer capacitor charging, where Faradaic charging is due to the generation of the co-ions instead to counter ions from the electrochemical reactions of the electrodes at certain applied voltages.

Faradaic and capacitive charging mechanism generate ions of opposite signs for an applied electric potential. However, the capacitive charging can not generate a charge density may exceeds the equilibrium charge density on the electrode. While, Faradaic charging can generate charge densities orders of magnitude beyond that equilibrium charges, as a consequence, the flow generated by Faradaic charging is stronger than the one generated by capacitive charging. This can be seen clearly in Figure 8.10, for a concentration of 10 μM, where the velocity rises slowly by increasing the voltage, this is due to the capacitive charging, and then it decreases exponentially due to Faradaic charging. According Jie-Wu [130], the AC-electroosmosis flow generated by the two charging process behaves in different manners as a function of the applied voltage, where the electrical charge $Q_{Cap} \propto V^2$ for the capacitive charging and $Q_{Far} \propto exp(V)$ for Faradaic charging respectively.

Based always on the same hypothesis, the explanation of a slight reversal pumping at low voltages for a given frequency, was also due to the presence of both charging mechanisms. however the reversal pumping was never seen at low voltages, this probably is due to the use of Carbon electrodes which may generate more charges than metal ones.

For higher conductivities, no reversal pumping can be seen as this can be due to ions crowding effect in the diffuse layer [4, 7], which will be discussed later in section 8.7.4.

With regard to 3D-HAR electrodes, no reverse pumping can be seen, because the capacitive charge mechanism predominates as there is a large electrodes surface, which allows the formation of large electrical double layer. This electrical double layer in turns is responsible for the capacitive charging mechanism. Because there is a threshold voltage for Faradaic reaction to occur [4], capacitive charging predominates at low voltages below 19 V_{pp}, while Faradaic charging start to take over at voltages greater than 19 V_{pp}.

By comparing both 3D-planar and 3D-HAR devices, the new design has shown a good performance and can generate faster fluid flow than the base line device. The fluid flow pumping was increased with a factor of 5 in forward direction, and about 3 times as velocity magnitude. The 3D-HAR micropump has a larger voltage range (1-19 V_{pp}) to generate forward pumping before it decreases, where the 3D-planar electrodes switches to reverse pumping at 12 V_{pp} for low conductive media.

8.7.3 Effect frequency on the fluid flow velocity

Similarly to previous experiments, two different AC-electroosmosis micropumps with different electrodes structures were tested. The electrodes sizes of the micropumps were kept the same. The fluid flow was measured as the variation of the frequency for different conductivities. The applied potential was fixed to 20 V_{pp}. The measurements were taken in 16 points.

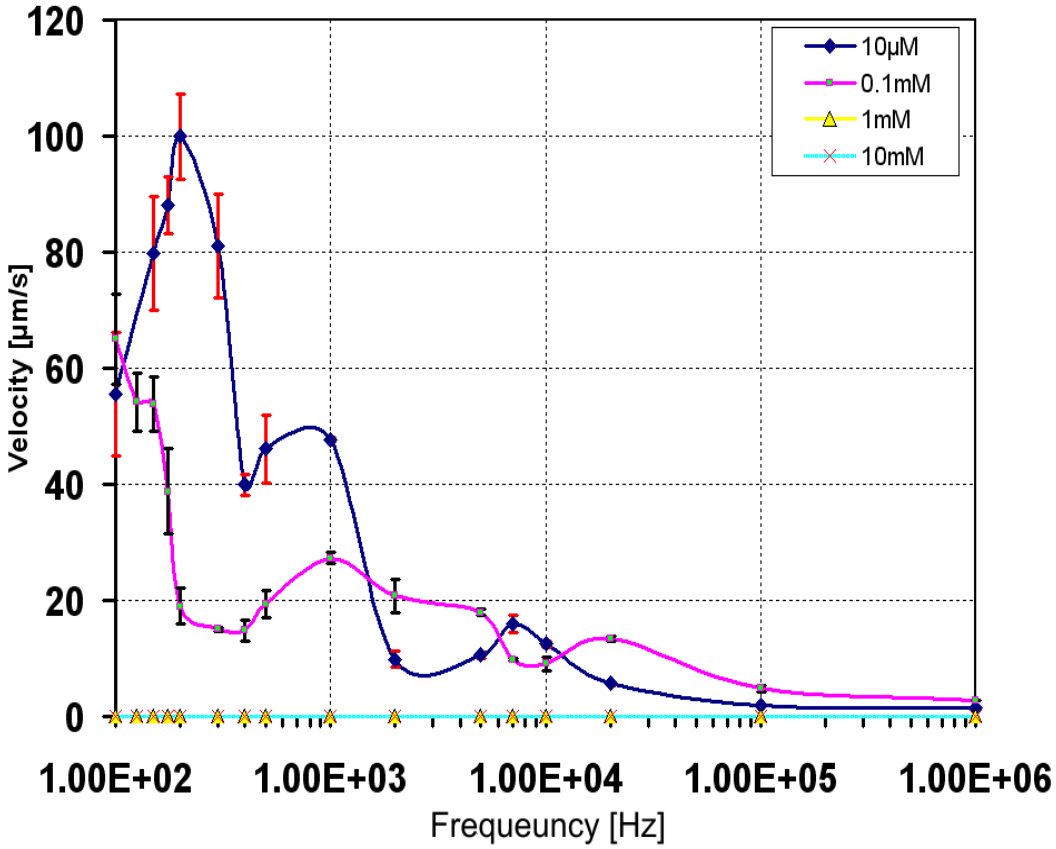

FIGURE 8.12: Fluid flow velocity versus frequency variation for 3D-planar electrodes, for different medium concentrations.

8.7.3.1 3D-planar electrodes

Similar to previous experiments, for high conductive media (with concentrations of 1 mM and 10 mM), no response of the micropump can be seen as a variation of the applied signal. The highest fluid flow velocities can only seen at low frequencies below 10 kHz. It can be seen from Figure 8.12 that the fluid velocities achieved at 10 μM medium are higher than the one reached at 0.1 mM one. At the lowest conductivity medium with a concentration of 10 μM, the maximum fluid flow velocity that was achieved is 100 $\mu m/s$ at a correspondent frequency of 200 Hz, where for 0.1 mM medium is about 65 $\mu m/s$. Also it can be seen that both spectra seem to fluctuate before to settle down at high frequencies.

8.7.3.2 3D HAR electrodes

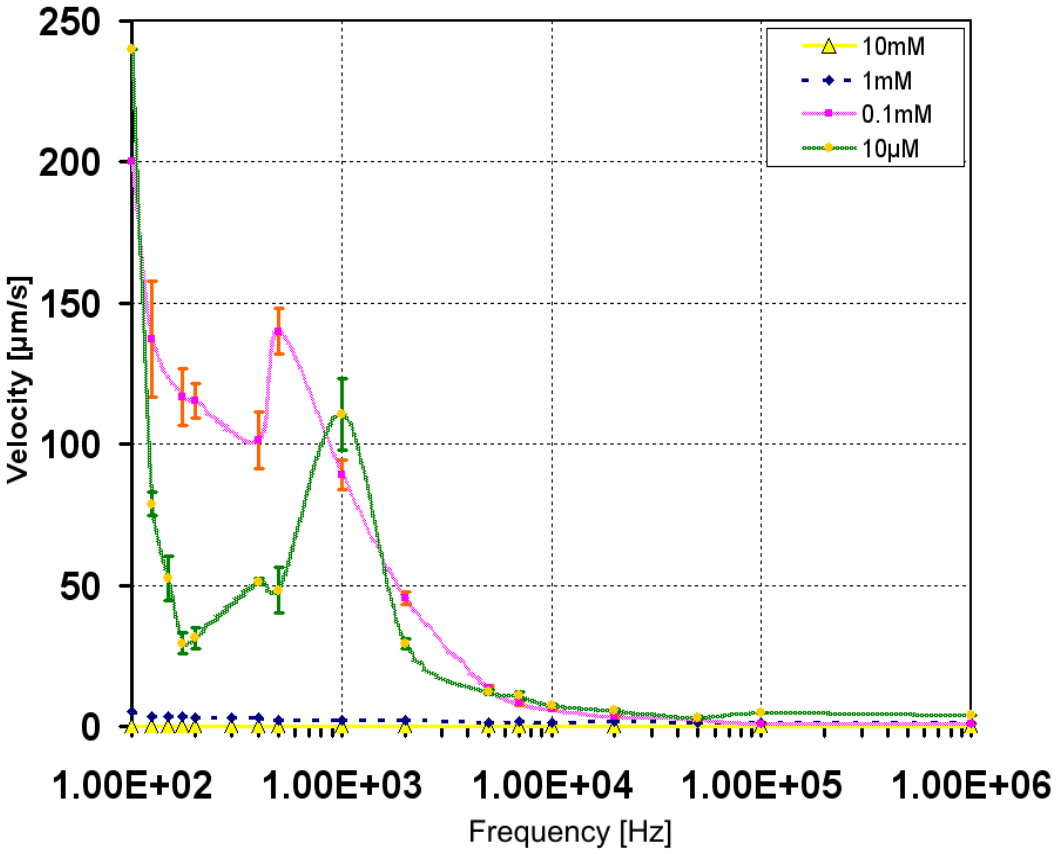

FIGURE 8.13: Fluid flow velocity versus frequency for 3D-electrodes, for different medium concentrations.

Unlike the 3D-planar electrodes micropump, the 3D-HAR electrodes ones behave in different manner as the frequency varies. For the lowest electrolyte conductivity the micropump shows a maximum fluid flow velocity of 240 $\mu m/s$ at 100 Hz, then it decreases very fast as the frequency increases to reach to 30 $\mu m/s$ at 175 Hz. Afterward it increases gradually to achieve 120 $\mu m/s$ at 1 kHz, which seems to be the characteristic frequency. Beyond this frequency the fluid flow velocity declines again as the frequency increases to stabilize after 10 kHz and remains steady. Increasing the electrolyte concentration to 0.1 mM also shows that the maximum fluid flow velocity (200 $\mu m/s$) rises at 100 Hz, then decreases gradually to 100 $\mu m/s$ at 400 Hz. Then at 500 Hz the velocity increases again to 140 $\mu m/s$, but above this frequency it drops slowly to 5 $\mu m/s$ at 10 kHz. Beyond 10 kHz the velocity remains steady at the range of high frequencies up to 1 MHz. For

higher electrolyte concentration 1 mM, a slight pumping can be seen, a maximum fluid flow velocity of 5 $\mu m/s$ is reached at 100 Hz. Then it declines slowly, to 3 $\mu m/s$ at 200 Hz, to increase slightly again at 300 Hz to 3.2 $\mu m/s$. Subsequently, beyond these frequencies, it drops gradually to a minimum velocity of 1.3 $\mu m/s$ at high frequencies. However for the highest electrolyte concentration corresponds to 10 mM, no fluid flow velocity can be generated.

- Discussion

In these experiments, the minimum frequency used was 100 Hz in order to prevent the carbon electrodes from any damage may occur at low frequency. Unlike metal electrodes, Carbon ones do not dissolve at low frequencies, but instead, they brake. It is reported by Zaouk et al. [135] that pyrolysis process generates microporous in carbon structure. By merging these carbon electrodes in liquids, they behave like sponge and absorb the electrolyte. The absorption of the electrolyte reduces the adhesion of the electrodes to the substrate. By applying low frequencies less than 100 Hz, this leads to a complete electrodes delamination. The electrodes will then acts like floating cantilevers since they are not attached to the substrate, and vibrate in the electrolyte. The mechanical motion of the electrodes leads to generate bubbles, and then ends up by breaking up. Apart from the electrodes vibration at low frequencies, gas bubbles can be also generated at this range of frequencies due the electrochemical reactions.

It was proved experimentally and theoretically for AC-electroosmosis pumping using metallic electrodes, mainly gold and titanium [50, 47, 51, 90] that the response of the fluid flow velocity as a function of the frequency, has a bell shape . Between a pair of two electrodes, when a switching potential is applied, the charge layers migrate away and the opposite charges comes down. On the positive electrode, positive ions move away, and negative ions comes down. Opposite behaviour happens in the other electrodes. However, the AC-electroosmosis dominates at the boundary between no field in the bulk and high field in the bulk. At low frequencies no field penetrates to the bulk as the electrical double layer behaves as a capacitor and would see the applied potential as DC signal. At high frequencies no electrical double layer can be formed on the top of the

electrodes, therefore nothing will happen as all the electric field penetrates to the bulk. Therefore AC-electroosmosis only happens in the middle range frequencies. At these intermediate frequencies a peak frequency f_c will be achieved, this frequency is known as characteristic frequency.

For 3D-planar electrodes, from the experimental data represented in Figure 8.12, the characteristic frequency f_c at the lowest electrolyte concentration (10 μM) is 200 Hz. However, for the electrolyte concentration of 0.1 mM, for the f_c is not clear but it can be analytically predicted for medium concentrations (in the range of hundreds μM).

Similarly to 3D-planar structure, 3D-HAR electrodes the characteristic frequencies in both 10 μM and 0.1 mM electrolytes concentrations are 1 kHz and 500 Hz respectively. The variation in the characteristic frequency changes from one solution to another, because to its dependency to the solution concentration [7], this will be discussed in section 8.7.4.

At low electrolyte concentrations (10 μM, 0.1 mM), at low frequencies around 100 Hz, the flow velocity was observed to be at a maximum fluid flow velocity and then decreases for most graphs. This is mainly due to the generation of an extra numbers of ions in the electrical double layer due to electrochemical reactions.

As the frequency increases the fluid flow velocity decreases. However, the 3D-planar micropump behaves differently from the 3D-HAR one. The 3D-planar device, exhibited few peaks in velocity instead of a single one as the frequency varies. A secondary peak in the velocity spectrum was observed also by Urbanski et al. [118], but still not explained by the standard theory of the AC-electroosmosis. For the 3D-HAR device, apart from the initial starting peak around 100 Hz and the second peak around 1 kHz, no additional peaks can be seen. The 3D-HAR electrodes are the combination of planar electrodes array (on the bottom) and HAR pillars (on the top), therefore the two peaks in the velocity spectrum may represent the characteristic frequencies for the planar electrodes array and for the 3D-HAR pillars. The peaks are occurring in different frequencies since the gap between the pillars is larger than the distance between the planar electrodes which

was due to the shrinkage effect. To distinguish which peak represents the characteristic frequency for planar electrodes or for HAR pillars, the characteristic frequency can be calculated for the intermediate concentrations where the electroosmosis mechanism dominates. The characteristic frequency is defined by:

$$f_c = \frac{1}{2\pi\tau} \tag{8.5}$$

where τ: is the charge relaxation time for the electrical double layer capacitance.

$$\tau = R'C' \tag{8.6}$$

where, C' is the capacitance per unit area. R' is the the semicircular resistors as it is highlighted in chapter 3 where an AC-electroosmosis system can be modeled electrically by an RC circuit which is given by:

$$R' = \frac{d}{\sigma} \tag{8.7}$$

where d is length of the semicircular resistor and is given by $d = \pi r$, and "r" is being the half size of the gap between the electrodes. σ is the conductivity of the medium.

The capacitance per unit area can be estimated from the Debye-Huckel theory as:

$$C' = \frac{\epsilon}{\lambda_d} \tag{8.8}$$

where ϵ is the permittivity of the medium and λ_d is the thickness of the double layer and is given by:

$$\lambda_d = \sqrt{\frac{D\epsilon}{\sigma}} \tag{8.9}$$

where D is the the mean diffusion coefficient of the ions.

From the formulas 8.5, 8.6, 8.7, and 8.8 the characteristic frequency f_c becomes:

$$f_c = \frac{\sigma \lambda_d}{2\pi^2 r \epsilon} \tag{8.10}$$

To predict the characteristic frequency formula 8.10 is used. For the 0.1 mM solution, the characteristic frequency for the array is found 966 Hz and 460 Hz for the shrunken pillars. This gives an approximation for the main peaks where the the first peak is generated by the pillars where the second is generated by the planar array. For the 10 μM solution, it is difficult to judge since the concentration is very low which is almost water and not well-behaved. The rise at lower frequencies is likely to be electrochemical in nature.

Also several effects can take part in this behaviour. AC-electroosmosis, Faradaic charging, Steric effect, concentration polarization, Electrodes porosity and electrolyte absorbency. These effects may generate fluid flow on both reverse and forward directions, and may dominate at different range of frequencies. The activation of each mechanism at different frequencies may be responsible for the observed peaks. However, there is not enough data to distinguish between the frequency range, the direction and the magnitude of each effect.

Under the application of high frequencies signals ($>$ 20 kHz), both 3D-planer and 3D-HAR micropumps behave similarly, where the fluid flow velocity was decreased to a minimum value (close to zero) as the frequency increases. This means that there is almost no electrical double layer formed on top of the electrodes. With the absence of the ions of electrical double layer, no fluid flow pumping can be generated. This falls in agreement with previous work performed on metallic electrodes [18, 47, 50, 51, 90, 97, 118]. However in certain cases using metallic electrodes, a reversal pumping has been reported as the frequency increases [111, 118], which is not the case for carbon electrodes micropump. Although, there is no recent theoretical study that confirms this prediction, but was reported by Lastochkin et al. [74] that was attributed to Faradaic reactions also.

8.7.4 Effect of the medium concentration on the fluid flow

In previous experiments were presented in sections 8.7.2 and 8.7.3, have shown the decay of the of AC-electroosmosis flow velocity as the salt concentration increases, and effectively vanished at 1 mM and 10 mM for 3D-planar and 3D-HAR devices respectively. Similar effect was observed before [7, 111], but no concrete study was provided.

According to Kilic et al. [68], and Bazant [7], that the classical Poisson-Boltzmann theory assumes a dilute solution of point-like ions in thermal equilibrium in the mean potential. There exists a concentration c_{max}, above which this approximation breaks down. In AC-electroosmosis, the concentration dependence is roughly logarithmic for all frequencies where [7]:

$$u(\omega) \propto log(\frac{c_{max}}{c}) \tag{8.11}$$

where u, ω and c: are being the flow velocity, the frequency, and the actual concentration respectively. This proportion extrapolates to zero around $c_{max} \approx 10$ mM.

Chapter 9

Conclusions and Future work

9.1 Conclusions

In this thesis a new 3D AC-electroosmosis micropump is introduced, where a bulk (volumic) pumping of the fluid inside the channel is generated, this new design is based on increasing the electrodes surface by fabricating high-aspect-ratio conductive pillars on top of asymmetric planar electrodes. Since AC-electroosmosis is a surface driven effect, increasing the surface area increases the power coupled into the fluid movement. By taking the channel volume and filling it with conductive pillars, the surface area therefore increases, but the volume remains the same, increasing the drive per unit volume. This has the effect of increasing the pumping capabilities generated by the electrodes. However making high-aspect-ratio electrodes, for small dimensions below 10 μm and as thick as 50 μm can not be easily made by standard microfabrication techniques.

The fabrication flow first required patterning of planar electrodes followed by high aspect ratio pillars, than the fluidic channel. Due to the shrinkage effect occurring during the conversion of the polymer to carbon, planar electrodes thickness was chosen to be 5 μm, hence SU-8 5 formulation was used to make thin SU-8 layer. The optimum fabrication parameters to make planar electrodes were used are: a spinning speed was 500 rpm for 10 s, soft baked at 95^{o}C for 3min and then exposed to 33 mJ/cm^2 UV light,

the post exposure baked for 2 min. This layer was patterned on Silicon dioxide wafer. Silicon dioxide wafers were used due to their thermal resistance where they withstand to a temperature of more than 1000^{o}C during pyrolysis process. The wafers were cleaned and dehydrated at 150C for 1 hour before use their first use. Following the patterning of planar electrodes, high aspect ratio pillars fabrication was required. The optimization of UV photolithography parameters was first carried out, where an aspect ratio of 5:1 was made for a 100 μm thick layer and pillars dimensions below 20 μm. An improvement in the shape also was achieved, and clear gap between the pillars was obtained using SU-100. The final fabrication protocol found for making such structure is 3000 rpm spinning speed for 35 s, 20 min for softbake, $200mJ/cm^2$ and 10 min post exposure bake.

However, increasing the aspect ratio using standard UV-lithography to more than 5:1 was a problem. The first limitation was due the usage of a broadband source, where the short wavelengths below 365 nm seem to expose only the top side of the SU-8 layer and do not penetrate to the bottom part, hence the top part was overexposed while the bottom part of the structure was less exposed. Therefore a home-made filter using also a layer of SU-8 100 was fabricated to cut off the shorter wavelengths that penetrates to the pillars layer. The protocol for making SU-8 filter is 100 μm thick layer of SU-8 softbaked for 1 hour, and then exposed to 6 multiple exposure dose of $120mj/cm^2$ and subsequently baked for 2 hours. Using thick SU-8 filter ensure a good filtration however a drop in the UV-light intensity to up to 50% was expected and hence and increase in exposure time is required.

Although, removing the short wavelengths of the UV-source gave a high aspect ratio structure with high resolution, but a stiction effect where each two adjacent pillars stick together as a result of porous effect, the problem was found to be related directly to the surface tension between SU-8 developer solution and SU-8 pillars, this was solved by replacing the SU-8 solution by methanol which has lower surface tension than SU-8 developer as a consequently a the stiction effect was eliminated.

The following step was the combination of planar electrodes and high-aspect pillars

which was also a problem. Carbon planar electrodes become bumpy after pyrolization process, which make the high-aspect-ratio pillar to collapse if they are patterned on top of planar ones. Therefore it was important to pattern the HAR pillars ontop of SU-8 planar electrodes (before pyrolization). However upon spinning the pillars layer on top of the planar electrodes, the alignment marks can not be viewed and align both layers as both material have the same refraction index. Therefore a new intermediate layer of tape was used to cover the planar electrodes alignment marks from being covered by SU-8 and remove it afterward. This technique allowed us to align both planar and pillars layers successfully.

Combining both planar and high aspect electrodes resulted in dragging the planar electrodes form their initial positioning. This was due to high viscousity of SU-8 100 solution, which drags the electrodes during spinning process. Using two layers of SU-8 50 which has low viscousity than SU-8 100 formulation, this eliminated the drag effect problem successfully.

After the combined structure of planar and 3D HAR electrodes was successfully made using SU-8, the conversion of the polymer to a conductive polymer (carbon) was required. The structure was baked in a special furnace at 900^oC in a forming gas contains (95% N_2 and 5%H_2) for 1 hour and then cooled down for 10 hours. An aspect ratio of more than 12:1 for pillars with 4x4 μm_2 and 50 μm thick was achieved with gaps less than 15 μm. These electrodes dimensions were never achieved previously using standard lithography techniques. One effect occurs during pyrolysis process is the shrinkage effect, where the initial polymer structure loses its initial dimensions. This effect remains uncontrollable but it does not affect the functionality of the device.

Before encapsulating the electrodes in a fluidic channel, an electric inspection was performed on the electrodes. A short circuit resistance varies between 3-500 $k\Omega$ between the large and thin electrodes were found. The resistance was due to the inevitable remaining residues of SU-8 layer during developing. This layer was then removed by dry etch techniques using O_2 plasma etch.

Due to small dimensions of the electrodes, and the important positioning of the channel around the electrodes, SU-8 photoresist was employed instead of other polymers such as PDMS or PMMA,.. SU-8 25 photoresist was used to encapsulate 50 μm thick 3D pillars, the spinning speed was 1250 rpm for 35 s, and baked for 20 min at 95^{o}C, then exposed to 20 mJ/cm^2 UV light, followed by post exposure bake for 5 min.

For proof of concept set of planar electrodes free of channel were tested firstly using low conductive solution and 8 μ latex beads, a 30 $\mu m/s$ beads motion was achieved, as well as many effects occurred, such as DEP, ends effect, electrochemical effect, and bubbles generation. Therefore 500 nm diameter nanoparticles were used to minimize the influence of the DEP force, the minimum frequency used was limited to 100 Hz to minimize any electrochemical reaction and bubbles generation may occur, and finally the ends edges of the electrodes were covered with the fluidic channel to minimize the ends effect. Minimizing all these effects resulted to a fluid flow velocity of 35 $\mu m/s$ using carbon planar electrodes.

The effect of SU-8 resistance which was appeared between the large and thin electrodes during the fabrication was found that do not affect the fluid flow pumping.

The variations in voltage the carbon planar electrodes are capable to generate reverse and forward fluid flow, at low voltages below 5 V_{pp} and high voltages above 14 V_{pp} for 10 μM medium concentration. The maximum forward fluid flow velocity was achieved is 27 $\mu m/s$ at 20 V_{pp} in a medium concentration of 0.1 mM. Where the fastest reverse fluid flow velocity achieved was 55 $\mu m/s$ at 20 V_{pp} in lower conductive medium with concentration of 10 μM .

The ACEO pump with 3D-structure did not show reverse pumping, a maximum fluid flow pumping that was achieved is 160 $\mu m/s$ at 19 V_{pp}. It was seen that as the conductivity of the medium increases the velocity decreases which is in agreement with other research groups.

For the frequency, carbon micropumps also behave similarly to previous designs experiencing the characteristics frequency peak, however at low frequencies for 3D high-aspect-ratio structures a high fluid flow velocity was achieved, this is thought to be due

to some electrochemical reactions. A maximum fluid flow velocity achieved was 250 $\mu m/s$ using 3D high-aspect ratio electrodes structure.

Moreover, most of the AC-electroosmosis micropumps fabricated so far are characterized with short time life electrodes due to metal corrosion and electrolysis upon applying an electric potential to the electrodes, this thesis greatly extends the state of durability, biocompatibility and life time of AC-electroosmosis pumping using carbon electrodes. The new developed 3D high-aspect-ratio carbon pillars have shown not only a stronger holding against fluid flow, but also a good chemical resistance upon applying an electric potential as they do not undergo chemical reactions unlike gold electrode which may dissolve in few minutes under the presence of the electric potential.

9.2 Future work

- One important parameters in pumping is the back pressure generated. Since the 3D high-aspect-ratio micropump generates bulk pumping, it is assumed that the back pressure inside the channel is also increased. The next step will be the back pressure measurement.

- The behaviour of electrical double layer is not totally understood, therefore impedance spectroscopy are required to explain the behaviour the electrical double on top of C-MEMS structures, and its relationship between the flow rate and and the back pressure.

- Dimension and thickness of the electrodes, and gaps have to be optimized. Due to the inevitable shrinkage effect occurring during pyrolysis process, the gap dimensions can not be controlled. However, with the appearance of the new KPMG photoresist which has similar characteristics of SU-8, but it can easily removed, a high aspect ratio molds with small features can be made, and therefore making metallic high aspect ratio electrodes will be possible.

- Using triangles shaped electrodes instead of rectangles will be also investigated, since sharpest angles generates more strong electric filed forces which may improve pumping capabilities.

9.3 Publications

So far the following papers have been published:

[A] ***H. A. Rouabah***, B. Y. Park, R. B. Zaouk, H. Morgan, M. J. Madou and N. G. Green, AC Design and fabrication of a fully functional AC-electroosmosis micropump with 3D high-aspect ratio electrodes using only SU-8, Micromech. Microeng., 2009 (Invited paper. In preparation).

[B] N.G. Green, D. Malleo, ***H. A. Rouabah*** and H Morgan, AC electroosmotic micropumps: novel designs and fundamental experimental investigations, MIT Workshop on Electrokinetics, Cambridge, MA, Oct. 2008

[C] ***H. A. Rouabah***, B. Park, R. Zaouk, M. Madou, N. Green, Producing Fluid Flow Using 3D Carbon Electrodes, In: J. of Physics: Conf. Series, Vol. 142, pp. 012072-012075. 2008

[D] ***H. A. Rouabah***, B. Y. Park, R. B. Zaouk, H. Morgan, M. J. Madou and N. G. Green, AC Electroosmotic pumping in 3D C-MEMS structures. In: Proc. 12th International Conference on Miniaturized Systems for Chemistry and Life Sciences, San Diego, CA. USA. Oct. 2008

[E] ***H. A. Rouabah***, N. G. Green, B. Y. Park, R. B. Zaouk, M. J. Madou, H. Morgan, Measuring and testing of a novel 3D AC Electroosmosis carbon micro-pump fluid flow velocity using Nano-particles. In: the 12th annual European conference on micro & nanoscale technologies for biosciences, Montreux, Switzerland, Nov. 2008

[F] ***H. A. Rouabah***, B. Y. Park, R. B. Zaouk, H. Morgan, M. J. Madou, N. G. Green, Fabrication of Fully Functional AC-Electroosmosis Micropump with 3D High Aspect Ratio Electrodes Using Only SU-8. In: Proc. the 18th MicroMechanics Europe Workshop, pp. 317-320. Guimaras, Portugal, Sept. 2007

[G] Martinez-Duarte, R., ***Rouabah, H. A.***, Green, N., Madou, M. and Morgan, H. High efficiency and throughput particle separation with 3D C-MEMS dielectrophoresis. In: Proc. 11th International Conference on Miniaturized Systems for Chemistry and Life Sciences, Vol.3, pp 826-829, Paris, France, Oct. 2007

Appendices

Appendix A

Masks

There are 3 different masks are used for the fabrication. The first mask combines the planar electrodes, the pads, and the electrical leads. The second mask contains the high aspect ratio pillars features, and the last one is the channel mask. Due to small dimensions (up to $10mum$) The masks were chrome on glass made, they were printed with high resolution of $0.25\mu m$.

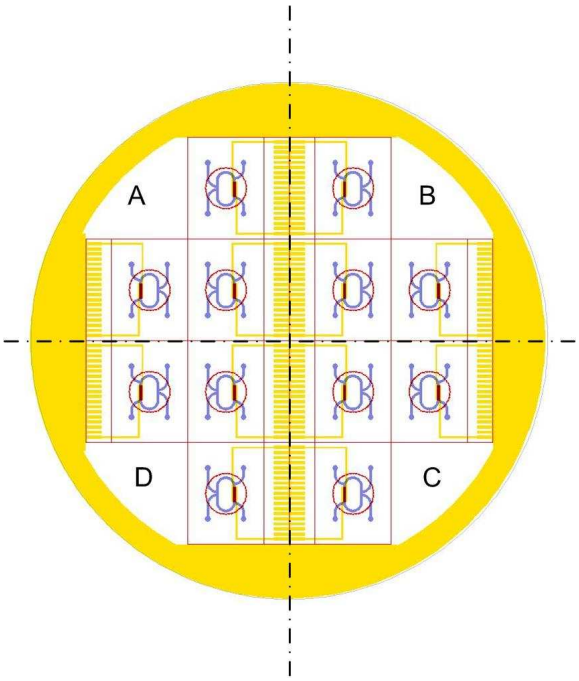

FIGURE A.1: Shows the layouts of the three masks used during the fabrication. The wafer is spitted to 4 regions (A,B,C, and D) with different electrodes dimensions. The wafer contains 12 devices, each device measure 2x2cm.

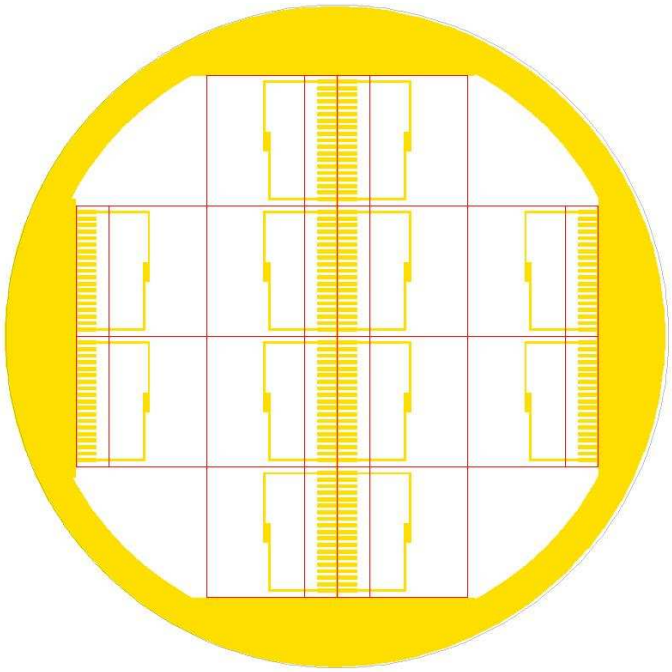

FIGURE A.2: Shows the layout of the mask for the planar electrodes, external pads, and electrical leads which are combined in as single layer

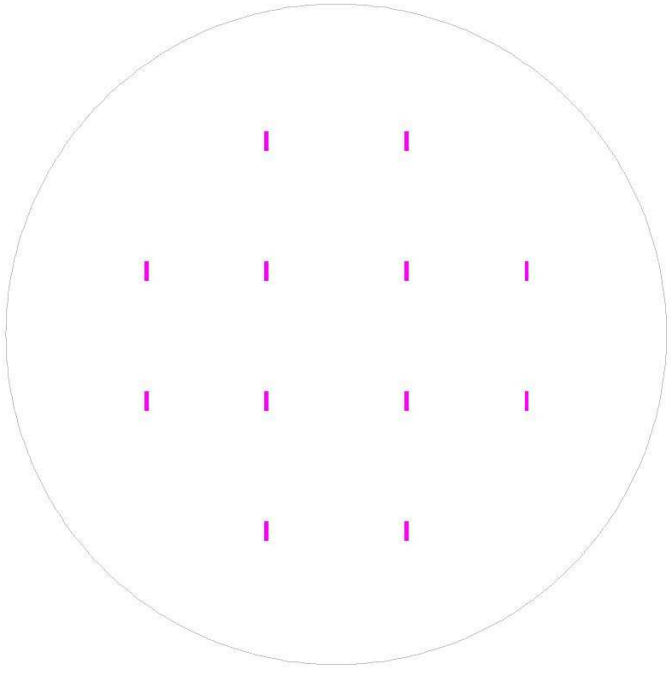

FIGURE A.3: Shows the layout of the mask for the 3D high-aspect-ratio electrodes, this layer follows the planar electrodes layer.

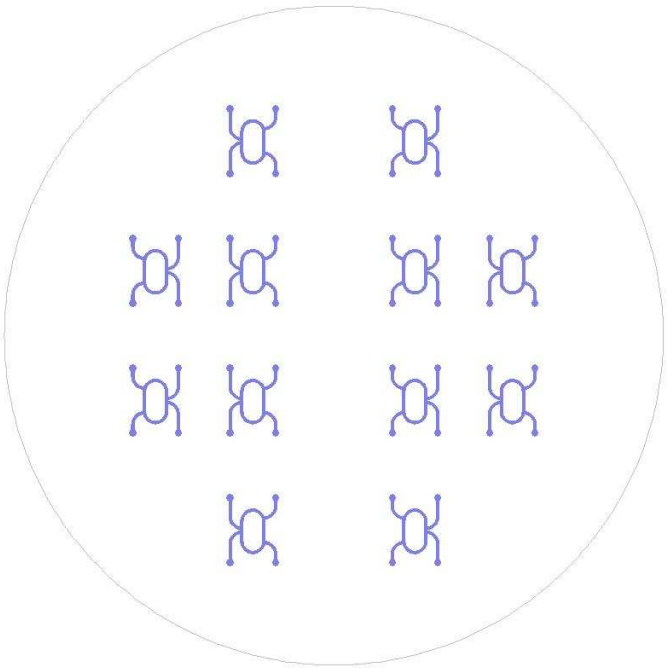

FIGURE A.4: Shows the layout of the mask for the channels, the channel width is $500\mu m$. The channel was designed to have two inlet and two outlets.

Label	Layout	Description	
A	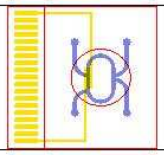	 10/30	Large electrode 30µm Large gap 30µm Narrow electrode 10µm Narrow gap 10µm Distance between Pillars: 86µm
B	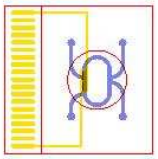	 20/60	Large electrode 60µm Large gap 60µm Narrow electrode 20µm Narrow gap 20µm Distance between Pillars: 74µm
C	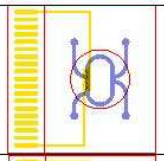	 10/50	Large electrode 50µm Large gap 50µm Narrow electrode 10µm Narrow gap 10µm Distance between Pillars: 86µm
D	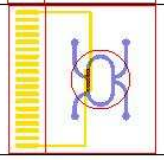	 20/100	Large electrode 100µm Large gap 100µm Narrow electrode 20µm Narrow gap 20µm Distance between Pillars: 77µm

FIGURE A.5: Shows the positioning of the electrodes inside the fluidic channel. It shows also different dimensions of both planar electrodes and high-aspect ratio pillars and the distance between each pillar.

Appendix B

SU-8 filter modulation

Matlab code adopted from Stuart Borden (NSI Group, University of Southampton), for the calculation of reflectance, transmittance and absorbance for a thin film of SU-8 on a glass substrate (B270 Crown glass) for light in the wavelength range 300-1240 nm, at normal incidence.

```
clear

%old wavelenth range

OldWave =

[300 305 310 315 320 325 330 335 340 345 350 360 370 380 390 400 410 ...

420 430 440 450 460 470 480 490 500 510 520 530 540 550 570 593 610 ...

630 656 668 690 710 718 724 740 753 758 763 768 780 800 816 824 832 ...

840 860 880 905 915 925 930 937 948 965 980 994 1040 1070 1100 1120 ...

1130 1145 1161 1170 1200 1240];

%Define new wavelength range

A = [300:1:1240];

%set angle of incidence to zero (normal incidence) Bdeg = 0; B = Bdeg./180.*pi;

X=A; Y=B; Ydeg = (Y./pi()).*180;

%refractive index of surrounding medium (i.e. air)
```

n0 = 1;

%refractive index of Su8 layer

$thinfilm1 =' Su8_Hamza.txt'$;

n1 = dlmread(thinfilm1);

%thickness of layer in nm

d(1) = 200;

$\%Definetherefractiveindexof B270crownglass, fromNagel99$

$(seeRefIndexB270glass_and_EVA.xlsand.JNB)$

nS = [1.54275 1.5424625 1.542175 1.5418875 1.5416 1.5413125 1.541025 ... 1.5407375 1.54045 1.5401625 1.539875 1.5393 1.538725 1.53815 1.537575 ... 1.537 1.536425 1.53585 1.535275 1.5347 1.534125 1.53355 1.532975 1.5324 ... 1.531825 1.53125 1.530675 1.5301 1.529525 1.52895 1.528375 1.527225 ... 1.5259025 1.524925 1.523775 1.52228 1.52159 1.520325 1.519175 1.518715 ... 1.51837 1.51745 1.5167025 1.516415 1.5161275 1.51584 1.51515 1.514 ... 1.51308 1.51262 1.51216 1.5117 1.51055 1.5094 1.5079625 1.5073875 ... 1.5068125 1.506525 1.5061225 1.50549 1.5045125 1.50365 1.502845 1.5002 ... 1.498475 1.49675 1.4956 1.495025 1.4941625 1.4932425 1.492725 1.491 ... 1.4887];

%interpolate to get glass refractive index for new wavelength range

ns = interp1(OldWave,nS,A);

%Thetat (Qt) for each layer

for k = 1:length(n)

Qtk = asin((n0.*sin(Y))./nk);

end

Qs = asin((n0.*sin(Y))./ns);

%————————————

%s polarisation, E vector perpendicular to plane of incidence.

%————————————

$Y0 = (n0. * (sqrt((8.854. * 10.^(-12)). * (4. * pi. * 10.^(-7))))). * cos(Y));$

$Ys = ns. * (sqrt((8.854. * 10.^{(}-12)). * (4. * pi. * 10.^{(}-7)))). * cos(Qs);$

%Y1s for each layer

for k = 1:length(n)

$Ymsk = nk. * (sqrt((8.854. * 10.^{(}-12))$

$. * (4. * pi. * 10.^{(}-7)))). * cos(Qtk);$

end

%deltam for each layer

for k = 1:length(n)

deltamk = (((2.*pi())./X).*nk.*d(k).*cos(Qtk));

end

%matrix elements of characteristic matrix for each layer

for k = 1:length(n)

m1mk = cos(deltamk);

m2mk = ((i.*sin(deltamk))./Ymsk);

m3mk = ((i.*sin(deltamk)).*Ymsk);

m4mk = cos(deltamk);

end

%Product of characterisatic matrices for first two layers or if there is only one layer, the transfer matrix is the characteristic matrix for this layer only.

if length(n) ¿1

m11 = ((m1m1.*m1m2)+(m2m1.*m3m2));

m21 = ((m1m1.*m2m2)+(m2m1.*m4m2));

m31 = ((m3m1.*m1m2)+(m4m1.*m3m2));

m41 = ((m3m1.*m2m2)+(m4m1.*m4m2));

else

```
m11 = m1m1;

m21 = m2m1;

m31 = m3m1;

m41 = m4m1;

end

%For more than two layers, this part calculates the product of all the

%characteristic matrices. The end matrix elements are the elements for the

%transfer matrix of the multilayer stack.

if length(n)¿2

for k = 2:(length(n)-1)

m1k = (m1k-1.*m1mk+1) + (m2k-1.*m3mk+1);

m2k = (m1k-1.*m2mk+1) + (m2k-1.*m4mk+1);

m3k = (m3k-1.*m1mk+1) + (m4k-1.*m3mk+1);

m4k = (m3k-1.*m2mk+1) + (m4k-1.*m4mk+1);

end

else

end

%Matrix elements of the transfer matrix of the multilayer stack.

MT1s = m1end;

MT2s = m2end;

MT3s = m3end;

MT4s = m4end;

%The reflection coefficient, rs, in terms of the transfer matrix elements for s

%polarization.

rs = (((Y0.*MT1s)+(Y0.*Ys.*MT2s)-MT3s-(Ys.*MT4s))
```

./((Y0.*MT1s)+(Y0.*Ys.*MT2s)+MT3s+(Ys.*MT4s)));

%The reflectance, R, for s polarization.

Rs = rs.*(conj(rs));

%The transmission coefficient, ts, in terms of the transfer matrix elements for s

%polarization.

ts = (2.*Y0)./((Y0.*MT1s)+(Y0.*Ys.*MT2s)+MT3s+(Ys.*MT4s));

%The transmittance, T, for s polarization.

Ts = (Ys./Y0).*(ts.*(conj(ts)));

%————————————————————

clear m1m m2m m3m m4m m1 m2 m3 m4 Y0 Ys

%————————————————————

%p polarisation. E vector parallel to plane of incidence.

%————————————————————

$Y0 = (n0. * (sqrt((8.854. * 10.^{(} - 12))$

$. * (4. * pi. * 10.^{(} - 7)))))./cos(Y));$

$Ys = ns. * (sqrt((8.854. * 10.^{(} - 12)). * (4. * pi. * 10.^{(} - 7)))))./cos(Qs);$

%Y1s for each layer

for k = 1:length(n)

$Ympk = (nk. * (sqrt((8.854. * 10.^{(} - 12))$

$. * (4. * pi. * 10.^{(} - 7))))))./cos(Qtk);$

end

%deltam for each layer

for k = 1:length(n)

deltamk = (((2.*pi()).*/X).*nk.*d(k).*cos(Qtk));

end

```
%matrix elements of characteristic matrix for each layer
for k = 1:length(n)
m1mk = cos(deltamk);
m2mk = ((i.*sin(deltamk))./Ympk);
m3mk = ((i.*sin(deltamk)).*Ympk);
m4mk = cos(deltamk);
end
%Product of characterisatic matrices for first two layers or if there
%is only one layer, the transfer matrix is the characteristic matrix for
%this layer only.
if length(n) ¿1
m11 = ((m1m1.*m1m2)+(m2m1.*m3m2));
m21 = ((m1m1.*m2m2)+(m2m1.*m4m2));
m31 = ((m3m1.*m1m2)+(m4m1.*m3m2));
m41 = ((m3m1.*m2m2)+(m4m1.*m4m2));
else m11 = m1m1;
m21 = m2m1;
m31 = m3m1;
m41 = m4m1;
end
%For more than two layers, this part calculates the product of all the
%characteristic matrices. The end matrix elements are the elements for the
%transfer matrix of the multilayer stack.
if length(n)¿2
for k = 2:(length(n)-1)
```

```
m1k = (m1k-1.*m1mk+1) + (m2k-1.*m3mk+1);

m2k = (m1k-1.*m2mk+1) + (m2k-1.*m4mk+1);

m3k = (m3k-1.*m1mk+1) + (m4k-1.*m3mk+1);

m4k = (m3k-1.*m2mk+1) + (m4k-1.*m4mk+1);

end

else

end

%Matrix elements of the transfer matrix of the multilayer stack.

MT1p = m1end;

MT2p = m2end;

MT3p = m3end;

MT4p = m4end;

%The reflection coefficient, rp, in terms of the transfer matrix elements

%for p polarization.

rp = (((Y0.*MT1p)+(Y0.*Ys.*MT2p)-MT3p-(Ys.*MT4p))

./((Y0.*MT1p)+(Y0.*Ys.*MT2p)+MT3p+(Ys.*MT4p)));

%The reflectance, R, for p polarization.

Rp = rp.*(conj(rp));

%The transmission coefficient, tp, in terms of the transfer matrix elements

%for p polarization.

tp = (2.*Y0)./((Y0.*MT1p)+(Y0.*Ys.*MT2p)+MT3p+(Ys.*MT4p));

%The transmittance, T, for p polarization.

Tp = (Ys./Y0).*(tp.*(conj(tp)));

%————————————- %Film absorption calculations

Absorbs = 1-Rs-Ts;
```

```
Absorbp = 1-Rp-Tp;

AbsorbAve1=real((Absorbs+Absorbp)./2);

%Identify non-zero absorption. This has to be done to get rid of the very

%small numbers that result from 1-R-T when there is no absorption. These %will mess up the plot so need to be made equal to zero.

AbsorbSig = AbsorbAve1¿0.000001;

AbsorbAve = AbsorbAve1.*AbsorbSig;

%If absorptance is zero, plot won't work because the z data is %constant. Therefore, identify this and add a very small value to the %absorptance at (1,1)

if sum(AbsorbAve)==0;

AbsorbAve(1,1)=0.00001

else

end

%Average reflectance

Rave = (Rs + Rp)./2;

%Average transmittance

Tave = real((Ts + Tp)./2);

%Data of R, T and A for normal incidence

Ravenorm = 100.*Rave(1,:)';

Tavenorm = 100.*Tave(1,:)';

Aavenorm = 100.*AbsorbAve(1,:)';

%plot nomal incidence R, T and A

figure(1)

subplot(3,1,1)

plot(A,Ravenorm)
```

```
xlabel('Wavelength (nm)');

ylabel('Reflectance (%)');

axis([300,1240,0,10]);

subplot(3,1,2)

plot(A,Tavenorm)

xlabel('Wavelength (nm)');

ylabel('Transmittance (%)');

axis([300,1240,60,100]);

subplot(3,1,3)

plot(A,Aavenorm)

xlabel('Wavelength (nm)');

ylabel('Absorptance (%)');

axis([300,1240,0,40]);
```

1.7374-0.0076703i, 1.7344-0.0073956i, 1.7313-0.0071209i, 1.7286-0.0068499i, 1.7262-0.0065818i, 1.7238-0.0063137i, 1.7214-0.0060456i, 1.7195-0.006i, 1.7178-0.006i, 1.716-0.006i, 1.7143-0.006i, 1.7127-0.006i, 1.7111-0.006i, 1.7095-0.006i, 1.7079-0.006i, 1.7064-0.006i, 1.7049-0.006i, 1.7034-0.006i, 1.7019-0.006i, 1.7005-0.006i, 1.699-0.006i, 1.6976-0.006i, 1.6961-0.006i, 1.6951-0.005783i, 1.6942-0.0055472i, 1.6932-0.0053113i, 1.6923-0.0050755i, 1.6912-0.0048437i, 1.6901-0.0046138i, 1.6889-0.0043839i, 1.6878-0.004154i, 1.6868-0.0039262i, 1.6861-0.0037025i, 1.6854-0.0034787i, 1.6848-0.003255i, 1.6841-0.0030313i, 1.6831-0.003i, 1.682-0.003i, 1.6809-0.003i, 1.6798-0.003i, 1.6788-0.0029427i, 1.6779-0.0027304i, 1.6771-0.002518i, 1.6762-0.0023057i, 1.6754-0.0020934i, 1.6745-0.0018848i, 1.6737-0.001679i, 1.6729-0.0014733i, 1.6721-0.0012675i, 1.6712-0.0010617i, 1.6704-0.00085972i, 1.6696-0.00065932i, 1.6688-0.00045892i, 1.668-0.00025852i, 1.6672-5.8116e-005i, 1.6663, 1.6653, 1.6644, 1.6634, 1.6624, 1.6616, 1.6608, 1.66, 1.6593, 1.6585, 1.658, 1.6574, 1.6568, 1.6563, 1.6557, 1.6551, 1.6545, 1.654, 1.6535, 1.6529, 1.6524, 1.6518, 1.6511, 1.6504, 1.6498, 1.6491, 1.6484, 1.6478, 1.6475, 1.6472, 1.6468, 1.6465, 1.6462, 1.6458, 1.6453, 1.6448, 1.6443, 1.6438, 1.6433, 1.6428, 1.6424, 1.6419, 1.6414, 1.6409, 1.6405, 1.64, 1.6396, 1.6392, 1.6388, 1.6384, 1.638, 1.6374, 1.6369, 1.6366, 1.6363, 1.636, 1.6357, 1.6354, 1.6351, 1.6347, 1.6343, 1.6339, 1.6334, 1.633, 1.6326, 1.6321, 1.6318, 1.6315, 1.6313, 1.631, 1.6307, 1.6304, 1.6302, 1.6299, 1.6296, 1.6294, 1.6291, 1.6288, 1.6286, 1.6283, 1.628, 1.627,

1.6267, 1.6264, 1.6261, 1.6258, 1.6255, 1.6253, 1.625, 1.6247, 1.6245, 1.6242, 1.624, 1.6237, 1.6235, 1.6232, 1.623, 1.6227, 1.6225, 1.6223, 1.622, 1.6218, 1.6215, 1.6213, 1.6211, 1.6208, 1.6206, 1.6204, 1.6201, 1.6199, 1.6197, 1.6194, 1.6192, 1.619, 1.6188, 1.6185, 1.6183, 1.6181, 1.6179, 1.6176, 1.6174, 1.6172, 1.617, 1.6169, 1.6168, 1.6167, 1.6166, 1.6165, 1.6163, 1.6162, 1.6161, 1.616, 1.6158, 1.6156, 1.6154, 1.6152, 1.615, 1.6148, 1.6146, 1.6144, 1.6142, 1.614, 1.6138, 1.6136, 1.6134, 1.6132, 1.613, 1.6128, 1.6126, 1.6124, 1.6122, 1.612, 1.6118, 1.6116, 1.6115, 1.6113, 1.6111, 1.6109, 1.6107, 1.6105, 1.6103, 1.6101 , 1.6099, 1.6098, 1.6096, 1.6094, 1.6092, 1.609, 1.6088, 1.6087, 1.6085, 1.6083, 1.6081, 1.608, 1.6079, 1.6078, 1.6077, 1.6076, 1.6075, 1.6074, 1.6074, 1.6073, 1.6072, 1.6071, 1.607, 1.6069, 1.6068, 1.6068, 1.6067, 1.6066, 1.6065, 1.6064, 1.6063, 1.6063, 1.6062, 1.6061, 1.606, 1.6059, 1.6057, 1.6055, 1.6054, 1.6052, 1.6051, 1.6049, 1.6047, 1.6046, 1.6044, 1.6043, 1.6041, 1.604, 1.6039, 1.6038, 1.6037, 1.6037, 1.6036, 1.6035, 1.6034, 1.6034, 1.6033, 1.6032, 1.6031, 1.6031, 1.603, 1.6028, 1.6027, 1.6025, 1.6024, 1.6022, 1.6021, 1.6019, 1.6018, 1.6017, 1.6015, 1.6014, 1.6012, 1.6011, 1.601, 1.6009, 1.6008, 1.6008, 1.6007, 1.6006, 1.6005, 1.6005, 1.6004, 1.6003, 1.6003, 1.6002, 1.6001, 1.6001, 1.6, 1.5999, 1.5999, 1.5998, 1.5997, 1.5997, 1.5996, 1.5995, 1.5995, 1.5994, 1.5993, 1.5993, 1.5992, 1.5991, 1.5991, 1.599, 1.5989, 1.5989, 1.5988, 1.5987, 1.5987, 1.5986, 1.5986, 1.5985, 1.5984, 1.5984, 1.5983, 1.5982, 1.5982, 1.5981, 1.5981, 1.598, 1.5979, 1.5977, 1.5976, 1.5975, 1.5974, 1.5973, 1.5972, 1.597, 1.5969, 1.5968, 1.5967, 1.5966, 1.5964, 1.5963, 1.5962, 1.5961, 1.596, 1.5959, 1.5959, 1.5958, 1.5958, 1.5957, 1.5956, 1.5956, 1.5955, 1.5955, 1.5954, 1.5954, 1.5953, 1.5952, 1.5952, 1.5951, 1.5951, 1.595, 1.595, 1.5949, 1.5949, 1.5948, 1.5947, 1.5947, 1.5946, 1.5946, 1.5945, 1.5945, 1.5944, 1.5944, 1.5943, 1.5943, 1.5942, 1.5942, 1.5941, 1.594, 1.594, 1.5939, 1.5938, 1.5937, 1.5936, 1.5935, 1.5934, 1.5933, 1.5932, 1.5931, 1.593, 1.5929, 1.5928, 1.5927, 1.5926, 1.5925, 1.5924, 1.5923, 1.5922, 1.5921, 1.592, 1.5919, 1.5919, 1.5918, 1.5918, 1.5917, 1.5917, 1.5916, 1.5916, 1.5915, 1.5915, 1.5915, 1.5914, 1.5914, 1.5913, 1.5913, 1.5912, 1.5912, 1.5911, 1.5911, 1.591, 1.591, 1.5909, 1.5909, 1.5908, 1.5908, 1.5907, 1.5907, 1.5907, 1.5906, 1.5906, 1.5905, 1.5905, 1.5904, 1.5904, 1.5903, 1.5903, 1.5902, 1.5902, 1.5902, 1.5901, 1.5901, 1.59, 1.5899, 1.5899, 1.5898, 1.5898, 1.5898, 1.5897, 1.5897, 1.5896, 1.5896, 1.5896, 1.5895, 1.5895, 1.5894, 1.5894, 1.5894, 1.5893, 1.5893, 1.5892, 1.5892, 1.5892, 1.5891, 1.5891, 1.589, 1.589, 1.589, 1.5889, 1.5889, 1.5889, 1.5888, 1.5888, 1.5887, 1.5887, 1.5887, 1.5886, 1.5886, 1.5886, 1.5885, 1.5885, 1.5884, 1.5884, 1.5884, 1.5883, 1.5883, 1.5883, 1.5882, 1.5882, 1.5881, 1.5881, 1.5881, 1.588, 1.588, 1.5879, 1.5878, 1.5878, 1.5877, 1.5876, 1.5876, 1.5875, 1.5874, 1.5873, 1.5873, 1.5872, 1.5871, 1.5871, 1.587, 1.5869, 1.5869, 1.5868, 1.5867, 1.5866, 1.5866, 1.5865, 1.5864, 1.5864, 1.5863, 1.5862, 1.5862, 1.5861, 1.586, 1.586, 1.586, 1.586, 1.586, 1.586, 1.586, 1.586, 1.586, 1.586, 1.586,

1.586, 1.5859, 1.5859, 1.5859, 1.5858, 1.5858, 1.5858, 1.5857, 1.5857, 1.5857, 1.5857, 1.5856, 1.5856, 1.5856, 1.5855, 1.5855, 1.5855, 1.5854, 1.5854, 1.5854, 1.5854, 1.5853, 1.5853, 1.5853, 1.5852, 1.5852, 1.5852, 1.5851, 1.5851, 1.5851, 1.585, 1.585, 1.585, 1.585, 1.5849, 1.5849, 1.5849, 1.5848, 1.5848, 1.5848, 1.5848, 1.5847, 1.5847, 1.5847, 1.5846, 1.5846, 1.5846, 1.5846, 1.5845, 1.5845, 1.5845, 1.5844, 1.5844, 1.5844, 1.5844, 1.5843, 1.5843, 1.5843, 1.5843, 1.5842, 1.5842, 1.5842, 1.5841, 1.5841, 1.5841, 1.5841, 1.584, 1.584, 1.5839, 1.5839, 1.5838, 1.5838, 1.5837, 1.5837, 1.5836, 1.5836, 1.5835, 1.5835, 1.5834, 1.5834, 1.5833, 1.5833, 1.5832, 1.5832, 1.5831, 1.583, 1.583, 1.5829, 1.5829, 1.5828, 1.5828, 1.5827, 1.5827, 1.5826, 1.5826, 1.5825, 1.5825, 1.5824, 1.5824, 1.5823, 1.5823, 1.5822, 1.5822, 1.5821, 1.5821, 1.582, 1.582, 1.582, 1.5821, 1.5821, 1.5821, 1.5821, 1.5822, 1.5822, 1.5822, 1.5822, 1.5823, 1.5823, 1.5823, 1.5823, 1.5824, 1.5824, 1.5824, 1.5824, 1.5825, 1.5825, 1.5825, 1.5825, 1.5826, 1.5826, 1.5826, 1.5826, 1.5827, 1.5827, 1.5827, 1.5827, 1.5828, 1.5828, 1.5828, 1.5828, 1.5828, 1.5829, 1.5829, 1.5829, 1.5829, 1.583, 1.583, 1.583, 1.583, 1.5829, 1.5829, 1.5829, 1.5829, 1.5829, 1.5828, 1.5828, 1.5828, 1.5828, 1.5827, 1.5827, 1.5827, 1.5827, 1.5827, 1.5826, 1.5826, 1.5826, 1.5826, 1.5825, 1.5825, 1.5825, 1.5825, 1.5825, 1.5824, 1.5824, 1.5824, 1.5824, 1.5823, 1.5823, 1.5823, 1.5823, 1.5823, 1.5822, 1.5822, 1.5822, 1.5822, 1.5821, 1.5821, 1.5821, 1.5821, 1.5821, 1.582, 1.582, 1.582, 1.582, 1.5819, 1.5819, 1.5819, 1.5819, 1.5819, 1.5818, 1.5818, 1.5818, 1.5818, 1.5818, 1.5817, 1.5817, 1.5817, 1.5817, 1.5817, 1.5816, 1.5816, 1.5816, 1.5816, 1.5816, 1.5815, 1.5815, 1.5815, 1.5815, 1.5815, 1.5814, 1.5814, 1.5814, 1.5814, 1.5814, 1.5813, 1.5813, 1.5813, 1.5813, 1.5813, 1.5812, 1.5812, 1.5812, 1.5812, 1.5811, 1.5811, 1.5811, 1.5811, 1.5811, 1.581, 1.581, 1.581, 1.581, 1.581, 1.5809, 1.5809, 1.5809, 1.5809, 1.5809, 1.5809, 1.5808, 1.5808, 1.5808, 1.5808, 1.5808, 1.5807, 1.5807, 1.5807, 1.5807, 1.5807, 1.5807, 1.5806, 1.5806, 1.5806, 1.5806, 1.5806, 1.5805, 1.5805, 1.5805, 1.5805, 1.5805, 1.5804, 1.5804, 1.5804, 1.5804, 1.5804, 1.5804, 1.5803, 1.5803, 1.5803, 1.5803, 1.5803, 1.5802, 1.5802, 1.5802, 1.5802, 1.5802, 1.5801, 1.5801, 1.5801, 1.5801, 1.5801, 1.5801, 1.58, 1.58, 1.58, 1.58, 1.58, 1.5799, 1.5799, 1.5799, 1.5799, 1.5799, 1.5799, 1.5798, 1.5798, 1.5798, 1.5798, 1.5798, 1.5798, 1.5797, 1.5797, 1.5797, 1.5797, 1.5797, 1.5797, 1.5796, 1.5796, 1.5796, 1.5796, 1.5796, 1.5796, 1.5795, 1.5795, 1.5795, 1.5795, 1.5795, 1.5795, 1.5794, 1.5794, 1.5794, 1.5794, 1.5794, 1.5794, 1.5793, 1.5793, 1.5793, 1.5793, 1.5793, 1.5793, 1.5792, 1.5792, 1.5792, 1.5792, 1.5792, 1.5792, 1.5791, 1.5791, 1.5791, 1.5791, 1.5791, 1.5791, 1.579, 1.579, 1.579

References

[1] A. Ajdari. Pumping liquids using asymmetric electrode arrays. *Physical Review E (Statistical Physics, Plasmas, Fluids, and Related Interdisciplinary Topics)*, 61(1):45–8, 2000.

[2] A. Ajdari. Electrokinetic 'ratchet' pumps for microfluidics. *Applied Physics A (Materials Science Processing)*, A75(2):271–4, 2002.

[3] T. A. Anhoj, A. M. Jorgensen, D. A. Zauner, and J. Hubner. The effect of soft bake temperature on the polymerization of su-8 photoresist. *Journal of Micromechanics and Microengineering*, 16(9):1819–1824, 2006.

[4] M. Z. Bazant, M. S. Kilic, B. Storey, and A. Ajdari. Nonlinear electrokinetics at large applied voltages. *eprint http://www.citebase.org/abstract?id=oai:arXiv.org:cond-mat/0703035*, 2007.

[5] M. Z. Bazant, J. A. Levitan, S. Devasenathipathy, V. Studer, Y. Ben, T. Thorsen, and T. M. Squires. Experimental observation of induced-charge electro-osmosis around a metal wire in a microchannel. *Colloids and Surfaces A (Physicochemical and Engineering Aspects)*, 267(1-3):122–32, 2005.

[6] M. Z. Bazant, K. Thornton, and A. Ajdari. Diffuse-charge dynamics in electrochemical systems. *Physical Review E - Statistical, Nonlinear, and Soft Matter Physics*, 70(2 1):021506–1–021506–24, 2004.

[7] M. Z. Bazant, J. P. Urbanski, J. A. Levitan, K. Subramanian, M. S. Kilic, A. Jones, and T. Thorsen. Electrolyte dependence of ac electro-osmosis. In *11th International Conference on Miniaturized Systems for Chemistry and Life Sciences (MicroTAS)*, pages 285–287., Paris, France, 2007.

[8] M. Z. Bazant and Ben Yuxing. Theoretical prediction of fast 3d ac electro-osmotic pumps. *Lab on a Chip*, 6(11):1455–61, 2006.

[9] B. Berge. Electrocapillarity and wetting of insulator films by water. *C. R. Acad. Sci. Paris II 3*, vol. 317(17):157–163, 1993.

[10] Ong Biow Hiem, Yuan Xiaocong, Tao Shaohua, and Tjin Swee Chuan. Photothermally enabled lithography for refractive-index modulation in su-8 photoresist. *Optics Letters*, 31(10):1367–9, 2006.

[11] B. Blackmore, D. Li, and J. Gao. Detachment of bubbles in slit microchannels by shearing flow. *Journal of Colloid and Interface Science*, 241(2):514–520, 2001.

[12] L. Bo, L. Miao, and C. Quanfang. Low-stress ultra-thick su-8 uv photolithography process for mems. *Journal of Microlithography, Microfabrication, and Microsystems*, 4(4):43008–1, 2005.

[13] S. A. Boden and D. M. Bagnall. Sunrise to sunset optimization of thin film antireflective coatings for encapsulated, planar silicon solar cells. *Progress in Photovoltaics: Research and Applications*, 17(4):241–252, 2009.

[14] A. L. Bogdanov. Use of su-8 negative photoresist for optical mask manufacturing. volume 3999 (II) of *Proceedings of SPIE - The International Society for Optical Engineering*, pages 1215–1225, Santa Clara, CA, USA, 2000. Society of Photo-Optical Instrumentation Engineers, Bellingham, WA, USA.

[15] A. L. Bogdanov and S. S. Peredkov. Use of su-8 photoresist for very high aspect ratio x-ray lithography. volume 53 of *Microelectron. Eng. (Netherlands)*, pages 493–6, Rome, Italy, 2000. Elsevier.

[16] Shew Bor-Yuan, Li Han-Chieh, Pan Ci-Ling, and Ko Cheng-Hao. X-ray micromachining su-8 resist for a terahertz photonic filter. *Journal of Physics D (Applied Physics)*, 38(7):1097–103, 2005.

[17] A. Brask. *Principles of Electroosmotic Pumps*. PhD thesis, Technical University of Denmark, 2003.

[18] A. B. D. Brown, C. G. Smith, and A. R. Rennie. Pumping of water with ac electric fields applied to asymmetric pairs of microelectrodes. *Physical Review E (Statistical Physics, Plasmas, Fluids, and Related Interdisciplinary Topics)*, 63(1, pt.1-2):016305–1, 2001.

[19] G. J. Brug, A. L. G. van den Eeden, M. Sluyters-Rehbach, and J. H. Sluyters. Analysis of electrode impedances complicated by the presence of a constant phase element. *Journal of electroanalytical chemistry and interfacial electrochemistry*, 176(1-2):275–295, 1984.

[20] K. Busch, S. Llkes, R. B. Wehrspohn, and H. Fll. *Photonic Crystals: Advances in Design, Fabrication, and Characterization*. Wiley-VCH, 2004.

[21] S. Bystrova, R. Luttge, and A. van den Berg. Study of crack formation in high-aspect ratio su-8 structures on silicon. *Microelectronic Engineering*, 84(5-8):1113–16, 2007.

[22] B. P. Cahill, L. J. Heyderman, J. Gobrecht, and A. Stemmer. Electro-osmotic streaming on application of traveling-wave electric fields. *Physical Review E*, 70(3 2):036305–1, 2004.

[23] F. Carmona. Conducting filled polymers. volume 157 of *Physica A (Netherlands)*, pages 461–9, Paris, France, 1989.

[24] L. G. Carrascosa, M. Moreno, M. Alvarez, and L. M. Lechuga. Nanomechanical biosensors: A new sensing tool. *TrAC - Trends in Analytical Chemistry*, 25(3):196–206, 2006.

[25] A. Castellanos, A. Ramos, A. Gonzalez, N. G. Green, and H. Morgan. Electrohydrodynamics and dielectrophoresis in microsystems: Scaling laws. *Journal of Physics D: Applied Physics*, 36(20):2584–2597, 2003.

[26] A. Castellanos, A. Ramos, A. Gonzalez, H. Morgan, and N. Green. Manipulation of bio-particles in microelectrode structures by means of non-uniform ac electric fields. volume 97 of *American Society of Mechanical Engineers, Materials Division (Publication) MD*, pages 165–170, New Orleans, LO, United States, 2002. American Society of Mechanical Engineers, New York, NY 10016-5990, United States.

[27] Kim Chang-Jin, J. Y. Kim, and B. Sridharan. Comparative evaluation of drying techniques for surface micromachining. volume A64 of *Sens. Actuators A, Phys. (Switzerland)*, pages 17–26, Nagoya, Japan, 1998. Elsevier.

[28] Y. T. Chu. Constant phase angle impedance of the finite sierpinski electrode. *Solid State Ionics*, 26(4):299–302, 1988.

[29] Y. J. Chuang, F. G. Tseng, and W. K. Lin. Reduction of diffraction effect of uv exposure on su-8 negative thick photoresist by air gap elimination. *Microsystem Technologies*, 8(4):308–313, 2002.

[30] V. Conedera, L. Salvagnac, N. Fabre, F. Zamkotsian, and H. Camon. Surface micromachining technology with two su-8 structural layers and sol-gel, su-8 or

sio¡sub¿2¡/sub¿/sol-gel sacrificial layers. *Journal of Micromechanics and Microengineering*, 17(8):52–7, 2007.

[31] E. H. Conradie and D. F. Moore. Su-8 thick photoresist processing as a functional material for mems applications. volume 12 of *J. Micromech. Microeng. (UK)*, pages 368–74, Cork, Ireland, 2002. IOP Publishing.

[32] B. E. Conway. Electrical double-layer and ion adsorption behavior at solid-solution interfaces. *Encyclopedia of Surface and Colloid Science*, pages 1908 – 1931, 2006.

[33] J. Darabi, M. M. Ohadi, and D. DeVoe. An electrohydrodynamic polarization micropump for electronic cooling. *Journal of Microelectromechanical Systems*, 10(1):98–106, 2001.

[34] J. Darabi, M. Rada, M. Ohadi, and J. Lawler. Design, fabrication, and testing of an electrohydrodynamic ion-drag micropump. *Journal of Microelectromechanical Systems*, 11(6):684–690, 2002.

[35] S. Debesset, CJ. Hayden, C. Dalton, JCT. Eijkel, and A. Manz. An ac electroosmotic micropump for circular chromatographic applications. *LAB ON A CHIP*, 4:396–400, 2004.

[36] P. Delahay and G. G. Susbielles. Double-layer impedance of electrodes with charge-transfer reaction. *The Journal of Physical Chemistry*, 70(10):3150–3157, 1966.

[37] F. W. Delrio, M. P. De Boer, J. A. Knapp, Jr. Reedy, E. D., P. J. Clews, and M. L. Dunn. The role of van der waals forces in adhesion of micromachined surfaces. *Nature Materials*, 4(8):629–34, 2005.

[38] M. Felten, P. Geggier, M. Jager, and C. Duschl. Controlling electrohydrodynamic pumping in microchannels through defined temperature fields. *Physics of Fluids*, 18(5), 2006.

[39] S. Ferree and H. W. Blanch. Electrokinetic stretching of tethered dna. *Biophysical Journal*, 85(4):2539–46, 2003.

[40] G. Fuhr, R. Hagedorn, T. Muller, W. Benecke, and B. Wagner. Pumping of water solutions in microfabricated electrohydrodynamic systems. Proceedings. IEEE Micro Electro Mechanical Systems. An Investigation of Micro Structures, Sensors, Actuators, Machines and Robots(Cat. No.92CH3093-2), pages 25–30, Travemunde, Germany, 1992. IEEE.

[41] G. Fuhr, T. Schnelle, and B. Wagner. Travelling wave-driven microfabricated electrohydrodynamic pumps for liquids. *Journal of Micromechanics and Microengineering*, (4):217–226, 1994.

[42] P. Garcia, A. Ramos, N. Green, and H. Morgan. Experiments on ac electrokinetic pumping of liquids using arrays of microelectrodes. 2005 IEEE International Conference on Dielectric Liquids, ICDL 2005, pages 181–184, Coimbra, Portugal, 2005. Institute of Electrical and Electronics Engineers Computer Society.

[43] P. Garcia-Sanchez and A. Ramos. The effect of electrode height on the performance of travelling-wave electroosmotic micropumps. *Microfluidics and Nanofluidics*, 5(3):307–312, 2008.

[44] P. Garcia-Sanchez, A. Ramos, N. G. Green, and H. Morgan. Experiments on ac electrokinetic pumping of liquids using arrays of microelectrodes. *IEEE Transactions on Dielectrics and Electrical Insulation*, 13(3):670–7, 2006.

[45] P. R. C. Gascoyne, Y. Huang, M. P. H. Hughes, X. B. Wang, R. Pethig, and F. F. Becker. Manipulation of erythroleukemia cells using travelling electric fields. volume 16 of *Annual International Conference of the IEEE Engineering in Medicine and Biology - Proceedings*, pages 772–773, Baltimore, MD, USA, 1994. IEEE, Piscataway, NJ, USA.

[46] S. Ghosal. Electrokinetic flow and dispersion in capillary electrophoresis. *Annual Review of Fluid Mechanics*, 38(1):309–338, 2006.

[47] A. Gonzalez, A. Ramos, N. G. Green, A. Castellanos, and H. Morgan. Fluid flow induced by nonuniform ac electric fields in electrolytes on microelectrodes. ii. a linear double-layer analysis. *Physical Review E (Statistical Physics, Plasmas, Fluids, and Related Interdisciplinary Topics)*, 61(4):4019–28, 2000.

[48] A. Gonzalez, A. Ramos, H. Morgan, N. G. Green, and A. Castellanos. Electrothermal flows generated by alternating and rotating electric fields in microsystems. *Journal of Fluid Mechanics*, 564:415–433, 2006.

[49] N. G. Green and H. Morgan. Sub-micrometre ac electrokinetics. volume vol.6 of *Proceedings of the 20th Annual International Conference of the IEEE Engineering in Medicine and Biology Society. Vol.20 Biomedical Engineering Towards the Year 2000 and Beyond (Cat. No.98CH36286)*, pages 2974–7, Hong Kong, China, 1998. IEEE.

[50] N. G. Green, A. Ramos, A. Gonzalez, H. Morgan, and A. Castellanos. Fluid flow induced by nonuniform ac electric fields in electrolytes on microelectrodes.

i. experimental measurements. *Physical Review E (Statistical Physics, Plasmas, Fluids, and Related Interdisciplinary Topics)*, 61(4):4011–18, 2000.

[51] N. G. Green, A. Ramos, A. Gonzalez, H. Morgan, and A. Castellanos. Fluid flow induced by nonuniform ac electric fields in electrolytes on microelectrodes. iii. observation of streamlines and numerical simulation. *Physical Review E (Statistical, Nonlinear, and Soft Matter Physics)*, 66(2):026305–1, 2002.

[52] N. G. Green, A. Ramost, A. Gonzalez, A. Castellanos, and H. Morgan. Electric field induced fluid flow on microelectrodes: The effect of illumination. *Journal of Physics D: Applied Physics*, 33(2):L13–L17, 2000.

[53] N. G. Green, Sun Tao, D. Holmes, and H. Morgan. Impedance based flow sensor. volume 5836 of *Proceedings of SPIE - The International Society for Optical Engineering*, pages 634–641, Seville, Spain, 2005. International Society for Optical Engineering, Bellingham WA, WA 98227-0010, United States.

[54] M. M. Gregersen, L. H. Olesen, A. Brask, M. F. Hansen, and H. Bruus. Flow reversal at low voltage and low frequency in a microfabricated ac electrokinetic pump. *Physical Review E - Statistical, Nonlinear, and Soft Matter Physics*, 76(5), 2007.

[55] P. D. Grossman and J. C. Colburn. Capillary electrophoresis: Theory and practice. *Academic Press*, page 237, 1992.

[56] L.J. Guerin. The su8 homepage (http://www.geocities.com/guerinlj/), 16-08-2005 2005.

[57] D. Haefliger, M. Nordstrom, P. A. Rasmussen, and A. Boisen. Dry release of all-polymer structures. *Microelectronic Engineering*, 78-79:88–92, 2005.

[58] S. Hardt and F. Schonfeld. *Microfluidic technologies for miniaturized analysis systems*. MEMS reference shelf. Springer, New York, NY, 2007.

[59] http://www.gersteltec.ch/. Gersteltec engineering solutions.

[60] H. Huang and C. Fu. Different fabrication methods of out-of-plane polymer hollow needle arrays and their variations. *Journal of Micromechanics and Microengineering*, 17(2):393–402, 2007.

[61] R. J. Hunters. *Zeta Potential in Colloid Science*. London ; New York : Academic Press, 1981.

[62] Lee Hyung-Joo, Park Jun-Taek, Yoo Ji-Yong, An Ilsin, and Oh Hye-Keun. Resist pattern collapse with top rounding resist profile. Digest of Papers. Microprocesses and Nanotechnology 2002. 2002 International Microprocesses and Nanotechnology Conference (IEEE Cat. No.02EX589), pages 280–1, Tokyo, Japan, 2002. Japan Soc. Appl. Phys.

[63] S. Jiguet, A. Bertsch, H. Hofmann, and P. Renaud. Conductive su8-silver composite photopolymer. 17th IEEE International Conference on Micro Electro Mechanical Systems. Maastricht MEMS 2004 Technical Digest (IEEE Cat. No.04CH37517), pages 125–8, Maastricht, Netherlands, 2004. IEEE.

[64] S. Jiguet, A. Bertsch, H. Hofmann, and P. Renaud. Su8-silver photosensitive nanocomposite. *Advanced Engineering Materials*, 6(9):719–723, 2004.

[65] S. B. Jiguet, A. Bertsch, H. Hofmann, and P. Renaud. Conductive su8 photoresist for microfabrication. *Advanced Functional Materials*, 15(9):1511–16, 2005.

[66] Saulius Juodkazis, Toshiaki Kondo, and Hiroaki Misawa. High-aspect ratio nanofabrication by femtosecond irradiation. volume 2005 of *Pacific Rim Conference on Lasers and Electro-Optics, CLEO - Technical Digest*, pages 1737–1738, Piscataway, United States, 2005. Institute of Electrical and Electronics Engineers Inc.

[67] M. J. Key, V. Cindro, and M. Lozano. On the radiation tolerance of su-8, a new material for gaseous microstructure radiation detector fabrication. *Radiation Physics and Chemistry*, 71(5):1003–1007, 2004.

[68] M. S. Kilic, M. Z. Bazant, and A. Ajdari. Steric effects in the dynamics of electrolytes at large applied voltages. i. double-layer charging. *Physical Review E - Statistical, Nonlinear, and Soft Matter Physics*, 75(2), 2007.

[69] T. Kondo, S. Juodkazis, and H. Misawa. Reduction of capillary force for high-aspect ratio nanofabrication. *Applied Physics A (Materials Science Processing)*, A81(8):1583–6, 2005.

[70] C. Kuo and C. Liu. A bubble-free ac electrokinetic micropump using the asymmetric capacitance-modulated microelectrode array for microfluidic flow control. *Journal of Microelectromechanical Systems*, 18(1):38–51, 2009.

[71] B. L. Kuzin and D. I. Bronin. Electrical double-layer capacitance of the m, o2/o2-interfaces (m = pt, au, pd, in2o3; o2- = zirconia-based electrolyte). *Solid State Ionics*, 136-137:45–50, 2000.

[72] N. C. LaBianca and J. D. Gelorme. High-aspect-ratio resist for thick-film applications. volume 2438 of *Proceedings of SPIE - The International Society for Optical Engineering*, pages 846–852, Santa Clara, CA, USA, 1995. Society of Photo-Optical Instrumentation Engineers, Bellingham, WA, USA.

[73] D. J. Laser and J. G. Santiago. A review of micropumps. *Journal of Micromechanics and Microengineering*, 14(6):35–64, 2004.

[74] Dmitri Lastochkin, Ronghui Zhou, Ping Wang, Yuxing Ben, and Hsueh-Chia Chang. Electrokinetic micropump and micromixer design based on ac faradaic polarization. *Journal of Applied Physics*, 96(3):1730–1733, 2004.

[75] R. A. Lawes. Manufacturing tolerances for uv liga using su-8 resist. *Journal of Micromechanics and Microengineering*, 15(11):2198–203, 2005.

[76] J. Liu, B. Cai, J. Zhu, G. Ding, X. Zhao, C. Yang, and D. Chen. Process research of high aspect ratio microstructure using su-8 resist. *Microsystem Technologies*, 10(4):265–268, 2004.

[77] H. Lorenz, M. Despont, N. Fahrnl, N. LaBianca, P. Renaud, and P. Vettiger. Su-8: a low-cost negative resist for mems. volume 7 of *J. Micromech. Microeng. (UK)*, pages 121–4, Barcelona, Spain, 1997. IOP Publishing.

[78] M. J. Madou. *Fundamentals of Microfabrication: The Science of Miniaturization, Second Edition*. CRC, 2 edition, 2002.

[79] A. Mata, A. J. Fleischman, and S. Roy. Fabrication of multi-layer su-8 microstructures. *Journal of Micromechanics and Microengineering*, 16(2):276–84, 2006.

[80] MicroChem. Su-8 photoresists formulations (http://www.microchem.com/), 2005.

[81] Rong Minzhi, Zhang Mingqiu, Liu Hong, and Zeng Hanmin. Synthesis of silver nanoparticles and their self-organization behavior in epoxy resin. *Polymer*, 40(22):6169–78, 1999.

[82] H. Moon, Cho Sung Kwon, R. L. Garrell, and Kim Chang-Jin. Low voltage electrowetting-on-dielectric. *Journal of Applied Physics*, 92(7):4080–7, 2002.

[83] T. A. Moore and Y. Lai. Ac electroosmotic micropumping with a square spiral microelectrode array. 1st Microsystems and Nanoelectronics Research Conference, MNRC 2008 - Enabling Synergy and Accelerating Excellence in Graduate Student Research, pages 157–160, Ottawa, ON, Canada, 2008. Inst. of Elec. and Elec. Eng. Computer Society.

[84] H Morgan and N Green. *AC Electrokinetics: colloids and nanoparticles*. RSP, 2003.

[85] H. Morgan and N. G. Green. Dielectrophoretic manipulation of rod-shaped viral particles. *Journal of Electrostatics*, 42(3):279–293, 1997.

[86] M. Mpholo, C. G. Smith, and A. B. D. Brown. Low voltage plug flow pumping using anisotropic electrode arrays. *Sensors and Actuators B: Chemical*, 92(3):262–268, 2003.

[87] T. Muller, W. Michael Arnold, T. Schnelle, R. Hagedorn, G. Fuhr, and U. Zimmermann. A traveling-wave micropump for aqueous solutions: Comparison of 1 g and mug results. *Electrophoresis*, 14(1):764–772, 1993.

[88] Nguyen Nam-Trung, Huang Xiaoyang, and Chuan To Kok. Mems-micropumps: a review. *Transactions of the ASME. Journal of Fluids Engineering*, 124(2):384–92, 2002.

[89] T. Okamoto, T. Yamamoto, A. Takamatsu, N. Kaneko, and T. Fujii. Relationship between hydrophobic beads attachment and fluid flow in pdms microchannel. Proceedings of 2006 International Conference on Microtechnologies in Medicine and Biology, pages 119–122, Piscataway, NJ 08855-1331, United States, 2006. Institute of Electrical and Electronics Engineers Computer Society.

[90] L. H. Olesen, H. Bruus, and A. Ajdari. ac electrokinetic micropumps: the effect of geometrical confinement, faradaic current injection, and nonlinear surface capacitance. *Physical Review E (Statistical, Nonlinear, and Soft Matter Physics)*, 73(5):56313–1, 2006.

[91] OSRAM. Mercury short arc lamps hbo for microlithography. Technical report, OSRAM, 1999/2000.

[92] B. Y. Park, L. Taherabadi, C. Wang, J. Zoval, and M. J. Madou. Electrieal properties and shrinkage of carbonized photoresist films and the implications for carbon microelectromechanical systems devices in conductive media. *Journal of the Electrochemical Society*, 152(12):136–143, 2005.

[93] A. G. Peele, B. Y. Shew, K. D. Vora, and H. C. Li. Overcoming su-8 stiction in high aspect ratio structures. *Microsystem Technologies*, 11(2-3):221–4, 2005.

[94] W. F. Pickard. Ion drag pumping. i. theory. *Journal of Applied Physics*, 34(2):246–250, 1963.

[95] W. F. Pickard. Ion drag pumping. ii. experiment. *Journal of Applied Physics*, 34(2):251–258, 1963.

[96] A. Ramos, A. Gonzalez, A. Castellanos, N. G. Green, and H. Morgan. Pumping of liquids with ac voltages applied to asymmetric pairs of microelectrodes. *Physical Review E*, 67(5 2):056302–1, 2003.

[97] A. Ramos, A. Gonzalez, A. Castellanos, N. G. Green, and H. Morgan. Pumping of liquids with ac voltages applied to asymmetric pairs of microelectrodes. *Physical Review E (Statistical, Nonlinear, and Soft Matter Physics)*, 67(5):56302–1, 2003.

[98] A. Ramos, H. Morgan, N. G. Green, and A. Castellanos. Ac electrokinetics: a review of forces in microelectrode structures. *Journal of Physics D (Applied Physics)*, 31(18):2338–53, 1998.

[99] A. Ramos, H. Morgan, N. G. Green, and A. Castellanos. Ac electric-field-induced fluid flow in microelectrodes. *Journal of Colloid and Interface Science*, 217(2):420–422, 1999.

[100] A. Ramos, H. Morgan, N. G. Green, A. Gonzalez, and A. Castellanos. Pumping of liquids with traveling-wave electroosmosis. *Journal of Applied Physics*, 97(8):1–8, 2005.

[101] Yang Ren and Wang Wanjun. A numerical and experimental study on gap compensation and wavelength selection in uv-lithography of ultra-high aspect ratio su-8 microstructures. *Sensors and Actuators B (Chemical)*, 110(2):279–88, 2005.

[102] A. Richter, A. Plettner, K. A. Hofmann, and H. Sandmaier. Electrohydrodynamic pumping and flow measurement. Proceedings. IEEE Micro Electro Mechanical Systems, pages 271–276, Nara, Jpn, 1991. Publ by IEEE.

[103] A. Richter and H. Sandmaier. An electrohydrodynamic micropump. pages 99–104, Napa Valley, CA, USA, 1990. Publ by IEEE, Piscataway, NJ, USA.

[104] W. Satoh, M. Loughran, and H. Suzuki. Microfluidic transport based on direct electrowetting. *Journal of Applied Physics*, 96(1):835–41, 2004.

[105] K. Schjolberg-Henriksen, J. A. Plaza, J. M. Rafi, J. Esteve, F. Campabadal, J. Santander, G. U. Jensen, and A. Hanneborg. Protection of mos capacitors during anodic bonding. *Journal of Micromechanics and Microengineering*, 12(4):361–367, 2002.

[106] R. Schueler, J. Petermann, K. Schulte, and H.P. Wentzel. Agglomeration and electrical percolation behavior of carbon black dispersed in epoxy resin. *Journal of Applied Polymer Science*, 63(13):1741–1746, 1997.

[107] J. M. Shaw, J. D. Gelorme, N. C. Labianca, W. E. Conley, and S. J. Holmes. Negative photoresists for optical lithography. *IBM Journal of Research and Development*, 41(1-2):81–94, 1997.

[108] N. J. Shirtcliffe, Aqil Sanaa, C. Evans, G. McHale, M. I. Newton, C. C. Perry, and P. Roach. The use of high aspect ratio photoresist (su-8) for super-hydrophobic pattern prototyping. *Journal of Micromechanics and Microengineering*, 14(10):1384–9, 2004.

[109] T. M. Squires and M. Z. Bazant. Breaking symmetries in induced-charge electro-osmosis and electrophoresis. *Journal of Fluid Mechanics*, 560:65–101, 2006.

[110] G. Gerald Stoney. The tension of metallic films deposited by electrolysis. *Proceedings of the Royal Society of London. Series A, Containing Papers of a Mathematical and Physical Character (1905-1934)*, 82(553):172–175, 1909.

[111] V. Studer, A. Pepin, Y. Chen, and A. Ajdari. An integrated ac electrokinetic pump in a microfluidic loop for fast and tunable flow control. *The Analyst*, 129(10):944–949, 2004.

[112] O. M. Stuetzer. Ion drag pressure generation. *Journal of Applied Physics*, 30(7):984–994, 1959.

[113] O. M. Stuetzer. Ion drag pumps. *Journal of Applied Physics*, 31(1):136–146, 1960.

[114] K. Subramanian, J. P. Urbanski, J. A. Levitan, T. Thorsen, and M. Z. Bazant. Experimental study of electrolyte dependence of ac electro-osmotic pumps, 2007.

[115] L. Tanguy, S. Salomon, and L. Nicu. Spectral collocation-based numerical simulations of cylindrical ac-electro-osmotic flows for bioconcentration purposes and experimental validations. *Applied Physics Letters*, 94(3), 2009.

[116] W. H. Teh, U. Durig, U. Drechsler, C. G. Smith, and H. J. Guntherodt. Effect of low numerical-aperture femtosecond two-photon absorption on (su-8) resist for ultrahigh-aspect-ratio microstereolithography. *Journal of Applied Physics*, 97(5):054907, 2005.

[117] J. P. Urbanski, J. A. Levitan, D. N. Burch, T. Thorsen, and M. Z. Bazant. The effect of step height on the performance of three-dimensional ac electro-osmotic

microfluidic pumps. *Journal of Colloid and Interface Science*, 309(2):332–341, 2007.

[118] J. Paul Urbanski, T. Thorsen, J. A. Levitan, and M. Z. Bazant. Fast ac electro-osmotic micropumps with nonplanar electrodes. *Applied Physics Letters*, 89(14):143508, 2006.

[119] Y. Utsumi, T. Ikeda, M. Minamitani, and K. Suwa. Integrated structure of pmma microchannels for dna separation by microchip capillary electrophoresis. *Microsystem Technologies*, 14(9-11):1461–1466, 2008.

[120] H. T. G. Van Lintel, F. C. M. Van De Pol, and S. Bouwstra. Piezoelectric micropump based on micromachining of silicon. *Sensors and actuators*, 15(2):153–167, 1988.

[121] K. J. Vinoy K. A. Jose Vijay K. Varadan. Front matter. In *RF MEMS and Their Applications*, pages i–xii. 2003.

[122] M. E. Vlachopoulou, A. Tserepi, N. Vourdas, E. Gogolides, and K. Misiakos. Patterning of thick polymeric substrates for the fabrication of microfluidic devices. *Journal of Physics: Conference Series*, 10(1):293–6, 2005.

[123] K. D. Vora, A. G. Peele, B. Y. Shew, E. C. Harvey, and J. P. Hayes. Fabrication of support structures to prevent su-8 stiction in high aspect ratio structures. *Microsystem Technologies*, 13(5-6):487–93, 2007.

[124] K. D. Vora, B. Y. Shew, E. C. Harvey, J. P. Hayes, and A. G. Peele. Specification of mechanical support structures to prevent su-8 stiction in high aspect ratio structures. *Journal of Micromechanics and Microengineering*, 15(5):978–983, 2005.

[125] C. Wang, G. Jia, L. H. Taherabadi, and M. J. Madou. A novel method for the fabrication of high-aspect ratio c-mems structures. *Journal of Microelectromechanical Systems*, 14(2):348–358, 2005.

[126] C. Wang, L. Taherabadi, G. Jia, M. Madou, Y. Yeh, and B. Dunn. C-mems for the manufacture of 3d microbatteries. *Electrochemical and Solid-State Letters*, 7(11):435–438, 2004.

[127] E. Wasserman and A. R. Felmy. Computation of the electrical double layer properties of semipermeable membranes in multicomponent electrolytes. *Applied and Environmental Microbiology*, 64(6):2295–2300, 1998.

[128] M. Winter. Webelements, the periodic table on the www, (http://www.webelements.com), 2007 1993.

[129] P. Woias. Micropumps - past, progress and future prospects. *Sensors and Actuators B (Chemical)*, 105(1):28–38, 2005.

[130] Jie Wu. Biased ac electro-osmosis for on-chip bioparticle processing. *IEEE Transactions on Nanotechnology*, 5(2):84–88, 2006.

[131] H. Yang, H. Jiang, H. Ao, A Ramos, and P. Garcia-Sanchez. A symmetry electrode array for ac and traveling wave electroosmosis pumping. *2008 2nd International Symposium on Systems and Control in Aerospace and Astronautics, ISSCAA 2008*, 2008.

[132] H. Yang, H. Jiang, D. Shang, A. Ramos, and P. Garcia-Sanchez. Experiments on traveling-wave electroosmosis: Efect of electrolyte conductivity. *IEEE Transactions on Dielectrics and Electrical Insulation*, 16(2):417–423, 2009.

[133] Kun-Lin Yang, Sotira Yiacoumi, and Costas Tsouris. Electrical double-layer formation. *Dekker Encyclopedia of Nanoscience and Nanotechnology*, pages 1001 – 1014, 2004.

[134] Chuang Yun-Ju, Tseng Fan-Gang, Cheng Jen-Hau, and Lin Wei-Keng. A novel fabrication method of embedded micro-channels by using su-8 thick-film photoresists. *Sensors and Actuators A (Physical)*, A103(1-2):64–9, 2003.

[135] R. Zaouk, B. Y. Park, F. Galobardes, G. Turon Teixidor, and Madou M. Design and characterization of 3d carbon mems lithium ion microbatteries, 2006.

[136] J. Zhang, M. B. Chan-Park, and S. R. Conner. Effect of exposure dose on the replication fidelity and profile of very high aspect ratio microchannels in su-8. *Lab on a Chip*, 4(6):646–653, 2004.

[137] P. Zoltowski. On the electrical capacitance of interfaces exhibiting constant phase element behaviour. *Journal of Electroanalytical Chemistry*, 443(1):149–154, 1998.